NEURAL BASIS AND BEHAVIORAL EFFECTS OF DYNAMIC RESTING STATE FUNCTIONAL MAGNETIC RESONANCE IMAGING AS DEFINED BY SLIDING WINDOW CORRELATION AND QUASI-PERIODIC PATTERNS

A Dissertation
Presented to
The Academic Faculty

By

Garth John Thompson

In Partial Fulfillment
Of the Requirements for the Degree
Doctor of Philosophy in Biomedical Engineering

Georgia Institute of Technology
and Emory University

August 2013

Copyright © Garth John Thompson 2013

Neural Basis and Behavioral Effects of Dynamic Resting State Functional Magnetic Resonance Imaging as Defined by Sliding Window Correlation and Quasi-Periodic Patterns

Approved by:

Dr. Shella D. Keilholz, Advisor
Department of Biomedical Engineering
Georgia Institute of Technology and Emory University

Dr. Xiaoping Hu
School of Biomedical Engineering
Georgia Institute of Technology and Emory University

Dr. Dieter Jaeger
Department of Biology
Emory University

Dr. Garrett B. Stanley
Department of Biomedical Engineering
Georgia Institute of Technology and Emory University

Dr. Charles Epstein
Department of Neurology
The Emory Clinic

Date Approved: May 22nd, 2013

ACKOWLEDGEMENTS

Finally I would like to thank my family: Wendy, Mom, Dad, Logan and Andy, my friends: Chad, He, Chi-Chi, Sharanya, Sudesh, Klipper and everyone else who helped keep me sane through 5 years of grad school and as I wrote this 200+ page document. THANK YOU ALL!!!

TABLE OF CONENTS

ix

LIST OF TABLES

LIST OF FIGURES

xv

LIST OF SYMBOLS AND ABBREVIATIONS

Abbreviations used in text

AFNI	Analysis of functional neuroimages (program)
BLP	Band-limited power
BOLD	Blood oxygen level dependent
CBV	Cerebral blood volume
DMN	Default mode network
EEG	Electroencephalography
EPI	Echo-planar imaging
FFT	Fast Fourier transform
FIR	Finite impulse response
fMRI	Functional magnetic resonance imaging
FWER	Family-wise error rate
KATP	Adenosine triphosphate sensitive potassium (channel)
LFP	Local field potential
MRI	Magnetic resonance imaging
PET	Positron emission tomography
PVT	Psychomotor vigilance task
ROI	Region of interest
S1FL	Primary somatosensory cortex of the forelimb region
SGoF	sequential goodness of fit
SI	Primary somatosensory cortex
SPM	Statistical parametric mapping version 8 (program)

SPM8	Statistical parametric mapping version 8 (program)
TE	Echo time
TPN	Task positive network
TR	Repetition time

Symbols used in text

★	The function of calculating the Pearson product-moment correlation coefficient
N(X,Y)	Normal distribution with mean X, standard deviation Y
p	Probability (value), typically of not rejecting the null hypothesis
r	Pearson product-moment correlation coefficient (individual values), sometimes italicized
$r_{\text{lfp-bold}}$	Pearson correlation between LFP and BOLD signals calculated at every voxel and multiple time shifts
$r_{\text{lfp-bold-template}}$	Pearson correlation between $r_{\text{lfp-bold}}$ and fMRI spatiotemporal dynamic templates, calculated at multiple frame shifts
$r_{\text{lfp-template}}$	Pearson correlation between fMRI spatiotemporal dynamic strength versus time and LFP
T	Normal distribution that has been studentized
Type I	False positive
Type II	False negative
z	Value of a data point from a hypothetically normal distribution

xviii

Frequency bands used in text

Infraslow	Neural electrical signal in frequencies below 1Hz, typically 0-0.5Hz
Delta (δ)	Neural electrical signal in 1-4Hz
Theta (θ)	Neural electrical signal in 4-8Hz
Alpha (α)	Neural electrical signal in 8-14Hz
Beta (β)	Neural electrical signal in 14-40Hz
Gamma (γ)	Neural electrical signal in 40-100Hz

Symbols used in equations

D	Cross spectral density function
NPL	Negative peak on the left
NPR	Negative peak on the right
PPL	Positive peak on the left
PPR	Positive peak on the right
V	Covariance function

SUMMARY

While task-based functional magnetic resonance imaging (fMRI) has helped us understand the functional role of many regions in the human brain, many diseases and complex behaviors defy explanation. Alternatively, if no task is performed, the fMRI signal between distant, anatomically connected, brain regions is similar over time. These correlations in "resting state" fMRI have been strongly linked to behavior and disease. Previous work primarily calculated correlation in entire fMRI runs of six minutes or more, making understanding the neural underpinnings of these fluctuations difficult. Recently, coordinated dynamic activity on shorter time scales has been observed in resting state fMRI: correlation calculated in comparatively short sliding windows and quasi-periodic (periodic but not constantly active) spatiotemporal patterns. However, little relevance to behavior or underlying neural activity has been demonstrated. This dissertation addresses this problem, first by using 12.3 second windows to demonstrate a behavior-fMRI relationship previously only observed in entire fMRI runs. Second, simultaneous recording of fMRI and electrical signals from the brains of anesthetized rats is used to demonstrate that both types of dynamic activity have strong correlates in electrophysiology. Very slow neural signals correspond to the quasi-periodic patterns, supporting the idea that low-frequency activity organizes large scale information transfer in the brain. This work both validates the use of dynamic analysis of resting state fMRI, and provides a starting point for the investigation of the systemic basis of many neuropsychiatric diseases.

CHAPTER 1

INTRODUCTION

1.1 Background

One question critical to understanding the human brain is: How do cognitive processes and behavioral performance emerge from interacting brain systems? An important tool for answering this question comes from Biswal et al. (Biswal, Yetkin et al. 1995). They found that the functional magnetic resonance imaging (fMRI) signals from distant regions of the human brain are correlated at low frequencies. Initial investigation revealed that these correlations appeared in low frequency bands (under 0.1Hz in humans), below those that would be expected for physiological artifacts due to respiration or cardiac cycles (Cordes, Haughton et al. 2000). Biswal et al.'s original work used statistical correlation, but brain networks were subsequently discovered using data-driven methods such as independent component analysis (Calhoun, Adali et al. 2001) and hierarchical clustering (Cordes, Haughton et al. 2002). As these networks were generated from a measured similarity over time rather than known anatomical connections, they were referred to as *functional networks* and the methods used to generate them referred to as *functional connectivity*. As subjects were not required to perform a task for these networks to be found, this type of imaging was referred to as *resting state* fMRI.

Despite being generated functionally, these networks showed much similarity to underlying anatomical connectivity. The original paper (Biswal, Yetkin et al. 1995) found

1

a functional network in fMRI that included interhemispheric motor regions of the brain, and subsequent work showed functional networks in anatomically connected regions such as sensorimotor cortex, auditory cortex, visual cortex (Cordes, Haughton et al. 2000) and language regions (Hampson, Peterson et al. 2002).

An important functional network seen commonly in human fMRI was originally discovered not with fMRI, but with PET (positron emission tomography). PET imaging revealed a series of brain regions that were metabolically active when no task was performed (Raichle, MacLeod et al. 2001). Many of the implicated brain regions were known to be associated with the quiet monitoring of one's environment such as the precuneus/posterior cingulate cortex, angular gyri and medial prefrontal cortex. For this reason, these regions together were referred to as the *default mode network*. These regions could also be isolated using their correlated signals in resting state fMRI, and synchronously deactivated during performance of numerous tasks (Gusnard and Raichle 2001). Therefore, the default mode network was also considered a functional network that could be measured with resting state fMRI. When it was systematically investigated as such, something interesting was discovered; the default mode network was anti-correlated with another network of similar extent but different brain regions (Fox, Snyder et al. 2005; Fransson 2005). The anti-correlated network was referred to as the *task positive network* because it was anti-correlated with the default mode network (which was metabolically active at rest), and also because it contained regions activated during a wide variety of tasks such as premotor regions, inferior parietal cortex and dorsolateral prefrontal cortex. In addition to being locatable through brain metabolism (using PET) and through correlation of functional signals over time (using fMRI), the default mode

2

and task positive networks were also demonstrated to reflect previously observed brain systems that reflected underlying axonal tracts (Fox, Corbetta et al. 2006).

However, the use of fMRI to find functional networks complicated their interpretation. While the language of the brain is coded in electric potential changes, fMRI measures changes in blood flow, blood oxygenation and blood volume that are correlated with electrical potential changes that occurred several seconds earlier (Logothetis 2008). The signal measured is thus referred to as the blood oxygenation level-dependent signal (BOLD) (Ogawa, Menon et al. 1993) and the correlate of neural activity observed in fMRI is referred to as a *hemodynamic response* and varies based on brain region (Kay, David et al. 2008), but is generally consistent enough to model the underlying neural activity based on fMRI data (Friston, Harrison et al. 2003).

Despite this complication, early evidence suggested that functional connectivity was not merely a curiosity of the fMRI signal, and was probably related to underlying neural processing. The pioneering work in this field was done in diagnosis of Alzheimer's disease (Greicius, Srivastava et al. 2004; Rombouts, Barkhof et al. 2005) which showed a decrease in functional connectivity in the default mode network in patients as compared to healthy controls of the same age. Soon, evidence of anomalous functional networks was shown in other diseases including autism (Villalobos, Mizuno et al. 2005), schizophrenia (Garrity, Pearlson et al. 2007), depression (Greicius, Flores et al. 2007) and attention deficit hyperactivity disorder (Tian, Jiang et al. 2006; Zang, He et al. 2007). Functional connectivity methods were then used to see if variation in behavior in healthy individuals could be predicted. Tasks where a relationship was successfully found between functional networks and behavior have included working memory (Hampson,

3

Driesen et al. 2006; Tambini, Ketz et al. 2010; Wang, Laviolette et al. 2010), motor learning (Albert, Robertson et al. 2009), language (Waites, Stanislavsky et al. 2005; Hasson, Nusbaum et al. 2009), executive control or maintenance of attention against distractions (Weissman, Roberts et al. 2006; Seeley, Menon et al. 2007; Eichele, Debener et al. 2008; Kelly, Uddin et al. 2008; Prado, Carp et al. 2011; Prado and Weissman 2011; Prado and Weissman 2011), and auditory or somatosensory stimulus detection (Boly, Phillips et al. 2008; Sadaghiani, Hesselmann et al. 2009). A common result seen is an increase in correlation between brain regions related to the task (such as premotor cortex increasing in correlation with dorsolateral prefrontal cortex in a task that requires monitoring and planning), and a decrease in correlation between those brain regions and other brain regions, in particular those that may interfere with the task if activated (such as the aforementioned premotor-frontal network becoming anti-correlated with the angular gyri, which may interfere by increasing introspection).

Some studies have recorded fMRI during the task and compared performance to the observed concurrent functional connectivity, or fluctuations in signal immediate to the task (Hampson, Driesen et al. 2006; Boly, Phillips et al. 2008; Kelly, Uddin et al. 2008; Hasson, Nusbaum et al. 2009; Sadaghiani, Hesselmann et al. 2009; Prado, Carp et al. 2011; Prado and Weissman 2011; Prado and Weissman 2011). Many other studies, however, have recorded fMRI when the task is not actively being performed and compare functional connectivity to task performance recorded at another time (Hampson, Driesen et al. 2006; Seeley, Menon et al. 2007; Kelly, Uddin et al. 2008; Albert, Robertson et al. 2009; Tambini, Ketz et al. 2010; Wang, Laviolette et al. 2010). In these studies, the individual is typically instructed to remain awake but not move and not think about

4

anything in particular. This is hypothesized to place the individual's brain within the resting state where functional networks can be easily observed (Raichle, MacLeod et al. 2001). Positive results from both types of study suggest that spontaneous fluctuations exist at rest and continue during task performance, affecting the non-spontaneous brain activations that occur due to the task.

The methods used to compare functional connectivity to performance vary. First, functional networks can be generated for each individual and functional imaging run and compared in terms of spatial extent (or independent component strength) (Waites, Stanislavsky et al. 2005; Hampson, Driesen et al. 2006; Albert, Robertson et al. 2009; Hasson, Nusbaum et al. 2009). Second, hypothetically static networks can be pre-defined or generated, and the connectivity within one of these networks examined (Seeley, Menon et al. 2007; Carter, Astafiev et al. 2010) or between two regions within a network (Hampson, Driesen et al. 2006; Prado, Carp et al. 2011; Prado and Weissman 2011). Third, connectivity between two or more hypothetically static networks can also be investigated (Kelly, Uddin et al. 2008; Tambini, Ketz et al. 2010; Wang, Laviolette et al. 2010) or between a region in each network (Prado and Weissman 2011). Fourth, mean signal within these networks can also be examined over time (Weissman, Roberts et al. 2006; Boly, Phillips et al. 2008; Eichele, Debener et al. 2008; Sadaghiani, Hesselmann et al. 2009).

Of these four methods, only the last considers the temporal evolution of the signal within the networks before and after performance of the task. However, in a review by Sadaghiani et al. (Sadaghiani, Hesselmann et al. 2010) it was noted that both the type of task and the time point around the instance of the stimulus (peristimulus time) affect how

5

the signal in the network will be related to performance. This matches what is seen in models of spontaneous brain activity which suggest that the correlated/anti-correlated networks observed are due to coordinated changes occurring at certain locations at certain times, rather than incidental activation of one location suppressing its corresponding anti-correlated regions; this is reviewed in Deco et al. (Deco, Jirsa et al. 2011).

However, for many years functional networks were assumed to be stationary over the course of an fMRI run (typically six to eight minutes). Early evidence for this assumption came from finding high spatial correlation when comparing two such runs from a given subject (van de Ven, Formisano et al. 2004) and from the relationships between functional connectivity and chronic neuropsychiatric disorders (Greicius, Srivastava et al. 2004; Rombouts, Barkhof et al. 2005; Villalobos, Mizuno et al. 2005; Tian, Jiang et al. 2006). Because of this, studies that examine relationships between networks mostly use the time scale of one or more entire fMRI runs, typically six to ten minutes, to calculate correlation values (or independent components, etc.) (Waites, Stanislavsky et al. 2005; Hampson, Driesen et al. 2006; Seeley, Menon et al. 2007; Kelly, Uddin et al. 2008; Albert, Robertson et al. 2009; Hasson, Nusbaum et al. 2009; Tambini, Ketz et al. 2010; Wang, Laviolette et al. 2010).

Recent work has made it increasingly clear that, while traditional measures of functional connectivity provide an estimate of the 'average' relationship between areas, they mask a wealth of information about dynamic interactions within and between networks. Mathematical models of neural-based functional connectivity indicated that if the time period used to calculate correlations were small enough (30 seconds), variations in functional networks' extents could be observed (Honey, Kotter et al. 2007).

6

Experimental results from resting state MRI studies soon verified this prediction. In rats, Majeed et al. showed that the BOLD signals exhibit intrinsic spatiotemporal organization, with characteristic patterns persisting for seconds rather than minutes (Majeed, Magnuson et al. 2009). These characteristic patterns do not appear to match known evoked responses from the regions where they are observed. Similar characteristic patterns were subsequently observed using other fMRI contrasts in rats (Magnuson, Majeed et al. 2010) and using BOLD in humans (Grigg and Grady 2010; Majeed, Magnuson et al. 2011; Liu and Duyn 2013). In the diagnosis of schizophrenia, different results were shown for entire fMRI runs versus 96-second long sliding windows (Sakoglu, Pearlson et al. 2010). In healthy individuals, Chang and Glover examined the wavelet coherence and sliding window correlation (120 and 240 second windows) between areas of the default mode network (Raichle, MacLeod et al. 2001; Fox, Snyder et al. 2005), and found that at certain scales, temporal variability was greater than would be expected by chance (Chang and Glover 2010). Using sliding window independent component analysis, Kiviniemi et al. showed that the spatial extent of this network varied within individuals (Kiviniemi, Vire et al. 2011). This, and other recent studies (Allen, Damaraju et al. 2012; Handwerker, Roopchansingh et al. ; Hutchison, Womelsdorf et al. 2012) demonstrate that the correlation between areas could vary between strongly positive and strongly negative, features that were not captured by traditional 'steady-state' analysis methods. This is not limited to humans, as there have been reports of similar time-varying connectivity in nonhuman primates (Hutchison, Womelsdorf et al. 2012) and rats (Keilholz, Magnuson et al. 2012).

7

These findings generated much interest among the neuroimaging community but have been received with a healthy amount of caution due to the difficulty of determining the significance of these variations in connectivity. The spontaneous BOLD fluctuations are low in amplitude and easily contaminated by physiological noise. In addition, the preprocessing that is performed to limit noise contributions adds substantial autocorrelation to the signal. Indeed, two of the studies that reported variations in connectivity found similar dynamics when randomly-matched data were used (Handwerker, Roopchansingh et al. ; Keilholz, Magnuson et al. 2012). Periods of high synchronization across known anatomical connections are a potential sign of the correlation variations having a neural basis; however, in Figures 9 and 11 of Hutchison et al. (Hutchison, Womelsdorf et al. 2012) it is shown that occasional synchronization of the white-matter signal is seen as well, particularly in the shortest (30 second) windo

Early evidence that meaningful information can be extracted from dynamic functional connectivity came from Sakoğlu et al., who found differences between schizophrenia patients and healthy controls, despite using identical imaging and pre-processing methods on each group (Sakoglu, Pearlson et al. 2010). In support of a neural origin for the variability in connectivity, Chang et al. recently presented data from a simultaneous electroencephalography (EEG) and fMRI study that suggests that alpha power is inversely linked to the correlation between the default mode and dorsal attention networks (Chang, Liu et al. 2013). Tagliazucchi et al. reported a similar link between EEG power and functional connectivity using sliding windows (Tagliazucchi, von Wegner et al. 2012). However, while EEG power is typically more directly related to neural activity than fMRI, it is also highly integrative and poorly localized. Patient

models, as used by Sakoğlu et al., also do not allow direct investigation of the substrate of the functional connectivity changes. Therefore, many gaps are left in our present understanding. An approach is needed that can validate the neural basis of these changes in connectivity.

If the dynamic changes in resting state fMRI are not merely effects of signal processing, and do represent an interesting neural or metabolic process that should be investigated further, there are two ways to proceed. First, the dynamic changes could be compared to behavior in a model where a relationship to behavior has already been shown with static (using an entire fMRI run) functional connectivity. Second, a neural electrical basis for the dynamic changes in resting state fMRI could be investigated using the same type of multimodal study as has been used to investigate the neural electrical basis of standard fMRI (Logothetis, Pauls et al. 2001; Logothetis 2008).

1.2 Behavioral effects of dynamic resting state fMRI

Due to fMRI being safe and non-invasive, the majority of previous work has been done in human subjects. Therefore, it was advisable to begin this work with a human subject study of the effects of changes in dynamic functional networks prior to a task that has already been compared to steady-state functional connectivity. This was done as described in Chapter 2 and this work has been published in Thompson et al. (Thompson, Magnuson et al. 2012).

Because dynamic changes in functional networks are strongly related to a behavior, in a specific time epoch prior to the task on an intra-individual basis (Figure

9

2.6), and because this relationship mirrors what is seen in steady-state results, it suggests that such dynamic changes in functional connectivity could reflect underlying neural activity in the brain. Therefore Chapter 3 and Chapter 4 proceed to investigate whether this neural basis exists, and what neural activity may relate to what form of dynamics.

1.3 Neural basis of dynamic resting state fMRI

While a behavioral connection is informative that dynamic changes in resting state fMRI are interesting (as they are not just an abnormality of signal processing) it is not sufficient to determine if they have a neural basis. This is because fMRI is measuring a hemodynamic signal that correlates well with neural activity, but may be affected by numerous sources unrelated to the brain's neural electrical processing.

One potential hemodynamic signal that may be confounding results is "vasomotion", an approximately 0.1Hz periodic change in vascular size. Vasomotion is observable in locations presumably lacking neural processing, such as the fingernail tip (Mayhew, Askew et al. 1996), and can be induced *in vitro* within extracted arteries (Porret, Stergiopulos et al. 1998). Aliasing of physiological noise such as heart-rate and breath-rate can potentially induce fluctuations across the entire image, particularly at higher frequencies (Cordes, Haughton et al. 2000; Majeed, Magnuson et al. 2009). Another possible confounding hemodynamic signal is changes in blood flow in the absence of neural electrical events when a subject is anticipating having to perform a task (Sirotin and Das 2009). Preprocessing for functional connectivity analysis typically involves low-pass filtering, which can disperse correlation values and increase temporal

10

autocorrelation. As the thermal noise in fMRI is inherently blurred, spatial autocorrelation will exist as well. Therefore, dynamic changes observed in BOLD could theoretically either (a) have no behavioral significance, and/or (b) have behavioral significance under certain circumstances but be unrelated to underlying neural events.

Despite the widespread use of resting state fMRI, the relationship between the underlying neural activity and the resting state BOLD signal is complex and not well understood. Researchers investigating the neural substrate of resting-state fMRI have reported a correlational relationship between the spontaneous BOLD fluctuations and slow fluctuations of the power of local field potentials (LFP) (Shmuel and Leopold 2008; Pan, Thompson et al. 2011; Magri, Schridde et al. 2012). Shmuel and Leopold demonstrated a consistent, forward shifted in time, BOLD correlate of electrophysiological activity in multiple frequency bands (Shmuel and Leopold 2008). This paper was criticized by Logothetis et al. (Logothetis, Murayama et al. 2009) as there was a slight flicker in the visual field and data were recorded from the visual cortex, potentially creating an artifact in the gamma band of hypothesized neural activity and aliasing into the fMRI signal as well, thus possibly confounding results as gamma band activity and fMRI were highly correlated. Magri et al. (Magri, Schridde et al. 2012) did similar work without the confounding visual stimuli. Their results were superficially similar (compare Figure 2 of Magri et al. 2012 and Figures 2 and 3 of Shmuel and Leopold 2008) but demonstrated greater correlation and mutual information between BOLD and changes in gamma power (40-100Hz) than between BOLD and other frequency bands, and that alpha (8-12Hz) and beta (18-30Hz) power related to how gamma power affected the shape of the BOLD correlate's time waveform. Correlations

11

between BOLD and local field potentials (LFP) have also been demonstrated in an anesthetized rodent model (Pan, Thompson et al. 2011) and are localized spatially to the electrode location, and in time to an approximately four second lag under isoflurane (Pan, Thompson et al. 2011, Figure 5).These studies found links between BOLD and comparatively high-frequency LFPs, including gamma frequencies (40-100Hz) (Shmuel and Leopold 2008), beta to gamma (24-90Hz) (Magri, Schridde et al. 2012) or delta to gamma (1-100Hz) (Pan, Thompson et al. 2011). Each study found that peak correlation occurred when BOLD lagged the envelope of electrophysiology power by several seconds: a hemodynamic response similar to what has been observed in studies where a stimulus was presented (Logothetis, Pauls et al. 2001). Evidence of a more complex relationship, a wave of activity in BOLD that propagated past an electrode in visual cortex, was found in the monkey (Shmuel and Leopold 2008), however the findings were controversial (Logothetis, Murayama et al. 2009) and not replicated in rats (Pan, Thompson et al. 2011). These studies have also indicated that the LFP frequencies that are most correlated with the local BOLD signal are not the most predictive of interhemispheric correlation (Lu, Zuo et al. 2007; Pan, Thompson et al. 2011); this suggests that BOLD contains distinct contributions from local spontaneous activity and widespread functional networks.

Neither Shmuel and Leopold, Logothetis et al. (2009), Magri et al. nor Pan et al. (2011) used frequencies in the electrophysiology similar to what was used in the BOLD (less than 1Hz), instead using band-limited power of LFP (Leopold, Murayama et al. 2003) or broadband signal from electrophysiology (1Hz or greater). This is yet another potential confounding factor because, while electroencephalography is the standard

12

neural electrical recording method in healthy human subjects, it has been little studied at frequency bands matching the frequencies below 1Hz, which includes almost all frequencies investigated in standard functional connectivity analysis. This is due to problems with noise and interpretation (Tallgren 2006).

LFP-BOLD correlates may have a complex spatiotemporal structure, because most fMRI studies of spontaneous activity suggest it is more than a random series of local activations. This is, in part, due to the fact that the low-frequency, resting state BOLD signal exhibits strong correlation between distant anatomical locations in the functional networks (Cordes, Haughton et al. 2000; Calhoun, Adali et al. 2001). Highly reproducible spatiotemporal dynamics exist within these networks, and have been demonstrated in both anesthetized rats and awake humans (Majeed, Magnuson et al. 2009; Grigg and Grady 2010; Majeed, Magnuson et al. 2011). If the spatial locations that define a network are held constant and power spectra are examined for different epochs of time, it can be seen that the dominant frequencies within those spatial locations change (Chang and Glover 2010) and computer models indicate network extents may change over time as well (Honey, Kotter et al. 2007; Deco, Jirsa et al. 2011). If spontaneous fluctuations are linked to the underlying neurophysiology, correlates of these spatiotemporal dynamics would be expected in the neurophysiology as well.

If a neural basis of dynamic changes in the resting state fMRI is found, this implies that the changes in functional connectivity seen in disease and across performance groups in healthy individuals may result from underlying differences in the dynamics that make up these networks. Chapter 3 and Chapter 4 demonstrate that, in fact, neural electrical activity and dynamic resting state fMRI are strongly correlated. They

also measure the relationship between these dynamics and the correlated neural electrical activity. This work demonstrates that, by measuring resting state fMRI in a dynamic manner, we can better understand the neural bases of diseases and behavioral differences. As steady-state analysis of functional networks averages together large epochs of time, dynamic analysis may pick up changes that it ignores. Also, this work suggests that electrical recording from a single site may include influence of a larger dynamic process. This work thus provides the first steps towards linking spontaneous local activity to large-scale spontaneous processes in the brain. Future work that clarifies these links may help us understand how local changes in synaptic potentials can integrate to large scale changes across the entire brain that coordinate thought and behavior. Doing so provides a starting point for the investigation of the systemic basis of many neuropsychiatric diseases and behavioral differences between healthy individuals.

14

CHAPTER 2

BEHAVIORAL EFFECT OF DYNAMIC RESTING STATE FMRI DEFINED BY SLIDING WINDOW CORRELATION

The work presented in this chapter was published in full in the *Human Brain Mapping* journal (Thompson, Magnuson et al. 2012). It is included here as per Wiley reproduction instructions.

2.1 Introduction

This chapter sets out to compare dynamic resting state functional connectivity to behavior. The *default mode* and *task positive* networks were chosen as target networks in this study as they are large networks and were two of the first functional networks to be investigated in detail (Raichle, MacLeod et al. 2001; Fox, Snyder et al. 2005) and thus are better studied than many other networks. In addition, these networks were involved in the highly reproducible spatiotemporal dynamics in the low-frequency BOLD signal that were demonstrated by Majeed et al. (Majeed, Magnuson et al. 2011). A similar pattern on a similar time scale was observed by Grigg and Grady (Grigg and Grady 2010), who claimed it as one of two fundamental states of the default mode network.

This chapter will apply both traditional functional connectivity (using entire functional imaging runs to calculate correlation) and short-window correlation methods to performance prediction in healthy individuals both across the group (inter-

15

individually) and approximating per-individual results (intra-individually). The time windows used in the windowed correlation analysis were short enough to only reflect momentary, second-scale differences such as those seen by Majeed et al. (Majeed, Magnuson et al. 2011) and Grigg and Grady (Grigg and Grady 2010).

The psychomotor vigilance task (PVT) (Dinges and Powell 1985) was chosen for this study because it is a measure of sustained attention and both the default mode network and regions related to attentional control (i.e., the task positive network) (Lim and Dinges 2008) are known to be involved. Using fMRI and the general linear model to study the PVT, Drummond et al. (Drummond, Bischoff-Grethe et al. 2005) demonstrated that optimal performance was associated with a greater response in regions associated with sustained attention (e.g. inferior parietal and premotor cortex) whereas sub-optimal performance was associated with activity in the default mode network (e.g. posterior cingulate and medial frontal cortex). Both the default mode network and the task positive network, which overlaps with attentional control networks (Fox, Snyder et al. 2005; Fransson 2005), were involved in the second-scale activity observed by Chang and Glover and Majeed et al. (Chang and Glover 2010; Majeed, Magnuson et al. 2011). Additionally, the default mode network deactivates in response to task performance on time scales as short as only a few seconds (Singh and Fawcett 2008). Such results suggest dynamic properties of both the default mode and task positive networks, and that dynamic interaction between these networks may be responsible for performance variation in the PVT.

In this chapter, functional connectivity metrics on different time scales (an entire fMRI run, a 12.3s window or a single data point) are compared to multiple statistical

16

interpretations of reaction time (inter-individual linear regression and two-group analysis using inter-individual and intra-individual separations). Knowledge of which functional connectivity metrics predict fast PVT performance will demonstrate if short time scale analysis can be used to produce similar results to traditional entire-run functional connectivity. Furthermore, comparing intra-individual performance to functional connectivity will suggest whether performance prediction can be analyzed on a per individual basis or can only be analyzed using a group. This study motivates further work to both consider shorter time scales for functional connectivity analysis and the possibility of using intra-individual variations in functional connectivity to predict performance.

2.2 Materials and Methods

A brief summary of the methods used can be found in Figure 2.1 and Tables 2.1, 2.2 and 2.3.

2.2.1 Data collection

17 healthy human individuals were recruited (9 male and 8 female) with an age range of 18-26 years. Informed consent was obtained from all individuals. All studies were performed in compliance with the Georgia Institute of Technology Institutional Review Board. All data were acquired at the joint Georgia Institute of Technology/Georgia State University Center for Advanced Brain Imaging.
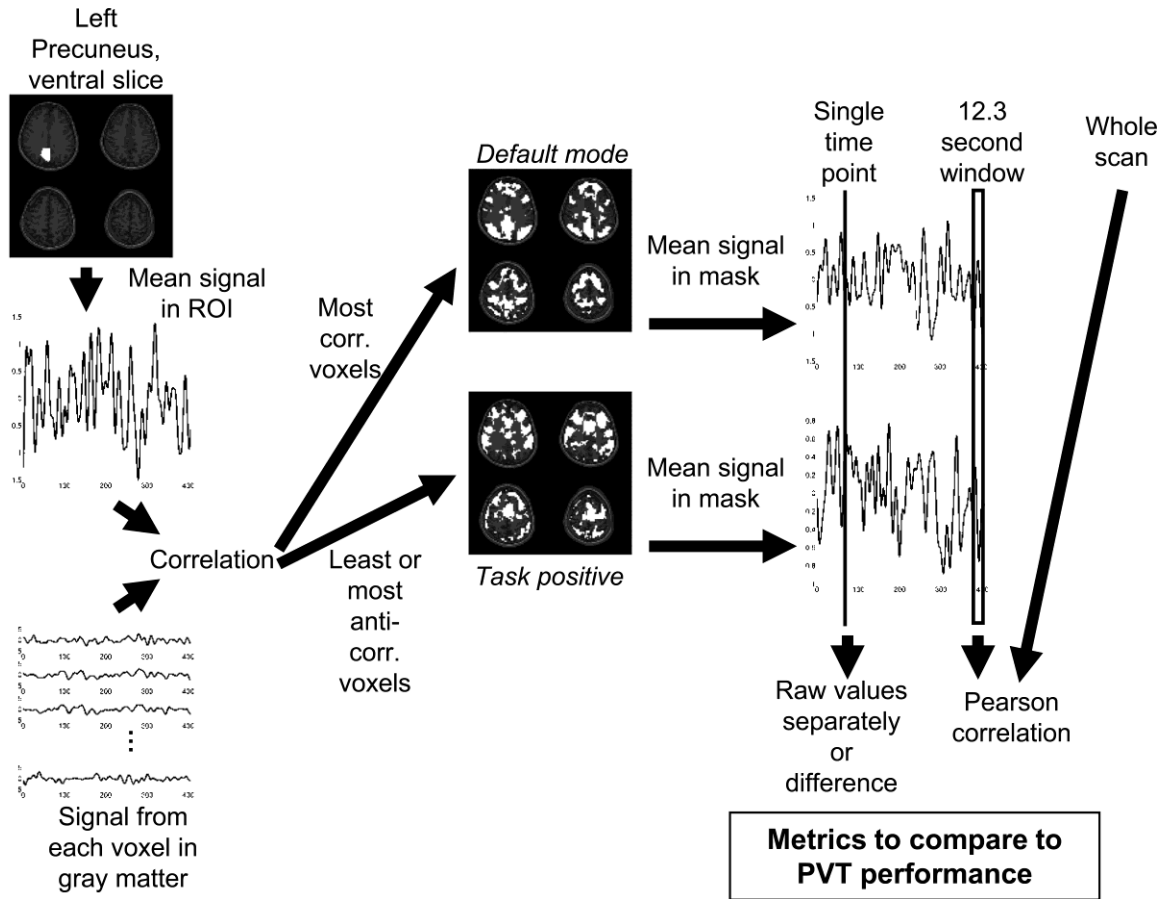
Figure 2.1: Calculation of functional connectivity metrics to compare to PVT performance. To calculate metrics from functional connectivity to compare to PVT performance, masks are generated from Pearson product-moment correlation coefficient (*r*) and then the mean signal is compared. The left precuneus in the most ventral image slice is found as an ROI using SPM8 and marsbar (shown in white). The mean signal in this ROI is taken and *r* calculated between it and every voxel in gray matter. The 1,639 (10% of whole image) voxels in gray matter most correlated with the ROI are taken as the default mode network (shown in white). The 1,639 voxels least correlated or most anti-correlated with the ROI in gray matter are taken as the task positive network (shown in white). The mean signal in each network mask is taken to produce a default mode network signal and a task positive network signal. The network signals are compared in several manners. At a single time point at some shift relative to an instance of PVT performance the mean signal in both networks and the difference in signal between networks can be compared to performance. In a 12.3s window at some peristimulus time relative to an instance of PVT performance, *r* between the two networks' mean signals can be calculated and compared to performance. Finally *r* between the entireties of the two networks' signals from each functional imaging run can be compared to performance.

18

All 17 individuals underwent high temporal resolution fMRI while performing a PVT. In this task participants fixated on a centrally presented black dot subtending 0.28^0 of visual angle on a gray background. When the dot changed to navy blue, participants pressed a button with their right index finger as quickly as possible. If participants failed to respond in 9 seconds, the dot returned to black. Each block lasted 8 minutes and the dot changed color between 3 and 5 times. Change onset was random for each participant (the delay time between onsets as an integer number of milliseconds randomly chosen from a range of 10,000 ms to 480,000 ms without replacement). Four fMRI runs of PVT performance were collected from each individual. Two fMRI *resting state* runs were collected from each individual. In resting state runs, individuals were told to lie quietly. The order of runs was counterbalanced between two options (Option 1: resting state, two PVT, resting state and two PVT. Option 2: two PVT, resting state, two PVT and resting state). In resting state runs individuals fixated on the black dot, but it never changed to navy blue. Participants were always informed that no change would occur before the start of each resting state run.

Images were acquired using Siemens Trio 3T whole body MRI scanner. Functional images acquired were echo-planar imaging (EPI) four horizontal slices including the precuneus and dorsal brain with voxels of size 3.4mm in the frequency and phase encoding directions and 5mm in the slice direction, repetition time (TR) 300 ms, echo time (TE) 30 ms and 1600 images. Slices were manually positioned to include the precuneus, medial prefrontal cortex, inferior parietal cortex and angular gyri using Figure 3 from Fox, et al. (p9679, Fox, Corbetta et al. 2005) as reference. Structural images were acquired using a T1 weighted MP RAGE 3D sequence with 1mm isotropic voxels.

19

2.2.2 Data preprocessing

The following preprocessing steps were done in Statistical Parametric Mapping 8 (SPM8) using the marsbar region of interest (ROI) plug-in: T1 images were segmented into gray matter, white matter and cerebrospinal fluid maps. The left precuneus ROI from the AAL Structural ROI library (Brett 2002) was reverse normalized (Chang and Glover 2010) from the MNI brain template to the individual T1 images. Individual T1 images were spatially cropped and registered to same-individual EPI images and this transformation was applied to all segments and left precuneus ROI as well. Reverse normalization allowed analysis to be performed in individual space rather than normalized space. This was necessary because individual EPI images did not cover the whole brain and had decreased signal to noise ratio due to the short TR used in this study.

EPI data were first slice-time corrected and then motion corrected through registration to a mean of all EPI images using Analysis of Functional NeuroImages (AFNI). From AFNI the maximum total movement in each direction (X, Y and Z) was recorded. 100 TR (30s) were removed from the beginning of EPI and motion data to eliminate stabilization effects. EPI data were blurred with a spatial Gaussian with sigma of 2x2x1 voxels and size of 3x3x1 voxels. A finite impulse response filter was used with a length of 150 TR (45s) and a pass band of 0.01 to 0.08Hz. As behavioral onset times were recorded in milliseconds from the start of the functional imaging run in raw data, they were corrected for the removed TRs and the phase shift resulting from the filter. Each voxel within EPI data was quadratically de-trended (Majeed, Magnuson et al. 2011) and divided by one standard deviation, resulting in unit variance. Mean signals were

20

calculated for whole-brain and white matter and these signals, in addition to filtered and cropped motion parameter signals, were regressed from EPI data. Final EPI data were again set to zero mean and unit variance for each voxel. This produced a normalized BOLD signal.

As it is debatable what to expect for a hemodynamic response to spontaneous fluctuations (Shmuel and Leopold 2008; Logothetis, Murayama et al. 2009), the normalized BOLD signal was not de-convolved with any hemodynamic response function. To compensate for this the central time point was placed at a delay of four seconds rather than zero seconds (Miezin, Maccotta et al. 2000, see section 2.2.11 below).

2.2.3 Functional network generation

For each normalized EPI time-course (405s after cropping and filtering) masks for default mode network and task positive network were created. The left precuneus ROI in the most ventral image slice was chosen as a *seed region* as it is a large, easily identified component of the default mode network (Fox, Snyder et al. 2005; Fransson 2005). The left side was chosen arbitrarily. The Pearson product-moment correlation coefficient (*r*) was calculated between the mean normalized time course for the seed region and each voxel's normalized time course for the entire fMRI run.

The 1,639 voxels in gray matter with the highest positive correlation with the precuneus were taken as the *default mode network*. The 1,639 voxels in gray matter with the weakest positive or strongest negative correlation were taken as the *task positive*

network. A constant number of voxels was chosen to maintain constant signal to noise ratio for mean signals from voxels within each network. The number 1,639 was 10% of the total number of voxels in the image (ceiling of 0.1 x 64 x 64 x 4). Percentiles of 5, 10, 15, 20 and 30 were tried and 10% was a sufficient number of voxels to produce default mode maps that appeared consistent to those presented by Fransson (Fransson 2005) when plotted against T1 weighted anatomical images. Functional imaging runs where the gray matter did not have at least 1,639 voxels were excluded, but otherwise no exclusivity was enforced for any voxel across different networks or fMRI runs. For each individual and functional imaging run a mean time course was taken from each of these networks to produce a *default mode network signal* and a *task positive network signal*.

This method of generating default mode and task positive networks (through correlation with a precuneus seed) was consistent with the early work in investigating the task positive network done by Fox et al. (Fox, Snyder et al. 2005) and by Fransson (Fransson 2005). Both Fox et al. and Fransson based network extents on correlation maps. As the primary purpose of this study was to use known networks, rather than to test networks for significance, network extents here were based on percentage of included voxels in the cluster (10% or 1,639 voxels) to create masks containing the same anatomical regions as seen in those early studies.

2.2.4 Exclusion

Functional imaging runs were excluded if the total range of movement in any direction was greater than the size of a voxel in the phase or frequency encoding direction

(3.4mm). However, functional imaging runs excluded due to motion or mask parameters were not excluded for calculation of behavioral parameters. Furthermore, instances where the individual failed to respond within 9 seconds were recorded as failures and excluded from both BOLD and behavioral data analysis.

2.2.5 Classification into fast and slow responses

While reaction times theoretically are continuously variable, for comparison to previous studies examining spontaneous fluctuations temporally locked to task performance it is desirable to divide reaction times into two groups of *good performance* (here, *fast performance*) and *bad performance* (here, *slow performance*) on the PVT (Weissman, Roberts et al. 2006; Boly, Phillips et al. 2008; Eichele, Debener et al. 2008; Sadaghiani, Hesselmann et al. 2009). Dividing instances into *fast response* and *slow response* groups also allows the characteristic spontaneous activity for *fast response* instances and for *slow response* instances to be examined separately.

Two performance metrics are desired: one which relates to variation within an individual's own performance, and a different metric which considers the entire group. To this end, instances of *change onset*, when the circle changed color from black to navy blue and the individual responded, were classified into *fast response* and *slow response* groups based on two metrics.

The first *inter-individual* metric was calculated by identifying the overall median value for all 17 individuals' response times combined. Instances were grouped into a fast response group and a slow response group whether the response time fell below or above

23

this overall median, respectively. Data falling into the central five percent of response times was excluded from this analysis to ensure separation between the two groups. This metric is more comparable to previous studies (Drummond, Bischoff-Grethe et al. 2005; Weissman, Roberts et al. 2006; Eichele, Debener et al. 2008; Kelly, Uddin et al. 2008) and allows for greater statistical power by allowing a linear fit across all runs from all subjects.

The second *intra-individual* metric was identical, except the median value to which any given instance was compared was calculated only using instances from the specific individual to which that instance belonged. Therefore individuals' instances were only compared to their own reaction times and each individual had approximately 50% of reaction times classified as fast and 50% as slow.

Table 2.1 shows an example of each metric.

2.2.6 Prediction using comparative metrics

Two comparative metrics (short-window correlation and local difference in magnitude) were chosen for their ability to extract a time-localized relationship between activity in the default mode network and the task positive network. Such metrics would thus target the time scale of the spatiotemporal dynamics of the default mode and task positive networks which have been observed to have phase differences between networks on a scale of seconds (Grigg and Grady 2010; Majeed, Magnuson et al. 2011). These metrics are described in sections 2.2.7 and 2.2.8.

24

Table 2.1: Example of calculation of intra-individual and inter-individual human performance metrics from PVT reaction times. Each individual has several instances of the PVT which, for testing purposes, are divided into *fast* and *slow* groups in two manners. **(a)** An overall median is calculated for all performance times from all individuals. In this example it is 1041.5ms. Each individual's reaction times are classified as fast or slow based upon being less than or greater than this median, respectively. This metric can be compared to all predictive metrics calculated from functional connectivity in this study. The groups of fast and slow reaction times can be considered *inter-individual* differences. **(b)** Each individual has a median calculated separately. Each individual's own reaction times are classified as fast or slow based upon being less than or greater than these individual median values, respectively. In this case, each individual has approximately 50% fast and 50% slow reaction times. This metric can be used to classify performance using a functional connectivity metric calculated at some peristimulus time around performance but (in the present chapter) cannot be used to classify performance using resting state functional connectivity. The groups of fast and slow reaction times can be considered *intra-individual* differences.

(a) Overall median

	Individual 1 (ms)	Individual 2 (ms)	Individual 3 (ms)
Instances classified as "fast"	942, 1029	716, 693, 648	920
Instances classified as "slow"	1054, 1329	1331	1204, 1156, 1314

(b) Individuals' own medians

	Individual 1 (ms)	Individual 2 (ms)	Individual 3 (ms)
Instances classified as "fast"	942, 1029	693, 648	920, 1156
Instances classified as "slow"	1054, 1329	716, 1331	1204, 1314

25

Both metrics were calculated at time locations from 16s before to 24s after each instance of the task. The time difference between the stimulus and the time location where the metric was calculated is referred to as the peristimulus time (Boly, Phillips et al. 2008; Sadaghiani, Hesselmann et al. 2009; Sadaghiani, Hesselmann et al. 2010). Peristimulus times was centered at 4s, which is the expected peak hemodynamic response in the motor cortex to a simple visual stimulation motor response task (Miezin, Maccotta et al. 2000). This interval also ensures with 95% confidence that no other change onset occurred at a peristimulus time that would be analyzed for the current onset, and is a large enough time span to compare to results seen in analysis of similar tasks, such as the *flanker task* which also measures attention, though in terms of cognitive control rather than maintenance (Eichele, Debener et al. 2008; see discussion). If the peristimulus time was such that it fell outside of available normalized BOLD data, then that peristimulus time was excluded from analysis for that instance.

Each metric at each peristimulus time was compared to reaction time in two manners. First, a linear regression was performed between the value of the metric and reaction time, producing an R^2 value, slope and slope standard error. Based on the slope and its standard error a *p* value was calculated (assuming a T distribution) and this was used as a probability of null hypothesis. The resulting 42 p-values (21 time points, correlation and magnitude) were tested to control family-wise error rate (see below). This method has higher statistical power as every point is used, but can only look at inter-individual differences due to the limited number of points per individual in this study.

Second, fast response and slow response groups were compared using a two sample T test at every peristimulus time. The resulting 84 p-values (21 time points,

26

overall and own medians, correlation and magnitude) were tested to control family-wise error rate (see below). This method has lower statistical power but allows comparison of intra-individual and inter-individual differences. Two-group statistical testing may produce different results than linear testing, e.g. one group may follow a linear trend but show no difference in mean when compared to the other group.

2.2.7 Short-window correlation

The intent of this chapter was to examine dynamic changes in correlation to determine if they were similar to entire-run correlation. Therefore, a window length needed to be chosen that was sufficiently short so that it represented dynamic changes, rather than reflecting the same correlations as entire-run functional connectivity with less averaging. Frequencies above 0.08 Hz were greatly attenuated by filtering. Therefore, r calculated from a window shorter than 12.5 seconds (1 / 0.08Hz = 12.5s) should eliminate much of the frequency profile that is being correlated using whole runs. Instead, it will only reflect similarity in time-local magnitude. Here 41 TRs (41 * 0.300s = 12.3s) were chosen for the correlation window as 12.3s < 12.5s.

2.2.8 Local difference in magnitude

As the signal from each voxel was normalized to zero mean and unit variance prior to getting the default mode and task positive networks' mean signals, and as the number of voxels averaged from each network was identical, the mean signal in each network can be considered to reflect its current state of activity, relative to the baseline.

27

Therefore, the difference between the two networks' signals can be considered to reflect the relative difference in current activity between the two networks. If the difference is relatively large, the networks are in relatively different states (e.g. default mode is activated and task positive is deactivated, or vice-versa), while if the difference is relatively small, the networks are in relatively similar states (e.g. the default mode and task positive are both activated, deactivated, or silent). For the purposes of this chapter, the mean signal from the task positive network was subtracted from the mean signal from the default mode network to provide a measure of the current relationship between the two networks. This was calculated point-by-point on normalized data.

2.2.9 Intra-individual prediction within fast and slow groups

Individuals were separated into a fast individuals group and a slow individuals group depending upon whether an individual's own median response time was above or below the overall median response time. Response instances from all individuals in each group (fast individuals and slow individuals) were then divided into fast and slow response instances based upon each individual's own median response time as described in section 2.2.5 (see Table 2.1(b) for an example) to approximate intra-individual performance.

As statistical power was greatly reduced by separating individuals into fast and slow groups, a reduced number of peristimulus times were used. Only peristimulus times found to be significant using either of the intra-individual two-group metrics (see section 2.3.2 and Figure 2.6) were used.

28

At each remaining peristimulus time, the short-window correlation and local difference in magnitude metrics (see above) were calculated. The fast response instances for each metric (short-window correlation and local difference in magnitude) and each set of individuals (fast individuals and slow individuals) were compared to the slow response instances for the same metric and set of individuals using a two sample T test at every peristimulus time. Family-wise error rate control was used on the fast individuals group and the slow individuals group separately with 6 hypotheses in each family (3 time points, short-window correlation and local difference in magnitude).

2.2.10 Resting state correlation

For comparison to the many functional connectivity studies on the time scale of entire fMRI runs (Waites, Stanislavsky et al. 2005; Kelly, Uddin et al. 2008; Albert, Robertson et al. 2009; Hasson, Nusbaum et al. 2009; Tambini, Ketz et al. 2010; Wang, Laviolette et al. 2010), r was calculated between the mean normalized BOLD signal within the default mode network and the task positive network for the entirety of each individual's resting state functional imaging runs. Each resulting correlation value was used as a data point compared to whether an individual's own median response time was above or below the overall median response time. This was tested with a two sample T-test. This was done to assess the relationship between network interaction and performance on an inter-individual, entire-functional-imaging-run basis. No family-wise error rate control was performed.

2.2.11 Prediction using signal change

At 2s intervals from 16s prior to 24s succeeding each instance of the task, the mean normalized BOLD signal within the default mode network and the mean signal in the task positive network were compared to reaction time in two manners. First, a linear regression was performed between the normalized BOLD signal and reaction time, producing an R^2 value and using the resulting *p* value for slope (considering a T distribution) as a probability of null hypothesis. The resulting 42 p-values (21 time points, default mode and task positive) were tested to control family-wise error rate (see below).

Second, normalized BOLD signal was compared between fast and slow response groups using a two sample T test. If the peristimulus time was such that it fell outside of available normalized BOLD data, then that peristimulus time was excluded from analysis for that instance. The resulting 84 p-values (21 time points, default mode and task positive, overall and own medians) were tested to control family-wise error rate (see below).

2.2.12 Test for differences in masks

To determine if network masks contain reproducible differences based on performance, the probability of a voxel being in the fast performance group (reaction time below overall median) was compared to the probability of it being in the slow performance group (reaction time above overall median). As dorsoventral orientation was observed to be consistent (Figure 2.2), all masks were registered using rigid-body

30

registration (Sochor, http://www.mathworks.com/matlabcentral/fileexchange/19086). The transformation was calculated by registering the corresponding structural image (the structural image registered to the functional imaging run) to the same slice of the structural image from the first valid subject and functional imaging run for that type (PVT or resting state) for all four slices. This transformation was then applied to the masks created from the corresponding functional imaging run. For each type of mask (default mode and task positive) and each functional imaging run type (PVT and resting state) the probability (zero to one) of each voxel being in a registered mask was calculated.

A map of differences between the probability maps was created by subtracting the slow group's probability in each voxel from the fast group's probability in the same voxel. In the resulting map very high or very low values would correspond to significantly different voxels between fast and slow groups. Significance was tested using artificial null distributions (see section 2.2.17).

2.2.13 Generation of Masks in 12.3s Windows

The viability of creating network masks within a short analysis window (rather than for entire functional imaging runs as in section 2.2.3) was tested. The analysis methods detailed in the sections 2.2.6 and 2.2.11 were performed again, with the difference that the masks used to define the Default Mode and Task Positive networks were calculated using only a 12.3s window centered at the peristimulus time being tested

31

in each case. In addition, the masks themselves were tested for significant differences between fast and slow performers as described in sections 2.2.12 and 2.2.17.

From previous model-based results (Honey, Kotter et al. 2007; Deco, Jirsa et al. 2011) these results are expected to reflect momentary changes in network dynamics and in general should not be consistent with the more stable networks generated from entire functional imaging runs. However, any methodologies where the results match indicate that these methodologies are highly stable, and thus highly useful for predicting response time on the basis of short time windows.

2.2.14 Family-wise error rate control

The purpose of this study was data-driven: to identify functional network properties predictive of individual performance rather than to model all such possible factors. Therefore, the results include multiple hypotheses, each represented by a probability (*p* value). Hypotheses are separated into families based on similarity in purpose as shown in Table 2.2.

As multiple *p* values resulting from multiple hypotheses are calculated, it was necessary to control against type I statistical errors (false positives). In this study the family-wise error rate (FWER) was chosen instead of false discovery rate as it detects families of viable hypotheses instead of testing hypotheses on an individual basis.

The sequential goodness of fit (SGoF) method was used to control FWER at 5% chance that all rejected null hypotheses are false positives (Carvajal-Rodriguez, de Una-Alvarez et al. 2009). SGoF performs an exact binomial test onto the expected distribution

32

of p values under the complete null hypothesis (no results significant). Therefore unlike standard Bonferroni FWER correction, SGoF will not increase in type II error (false negative) rate as the number of p values tested increases.

As SGoF assumes comparisons are independent, and comparisons in this study are likely to be non-independent, the possibility exists that this non-independence will create a cluster of small p values which will be incorrectly reported as significant. Therefore standard Bonferroni correction, which decreases the chance of reporting significance if comparisons are correlated, was also performed. Bonferroni correction has a high type II error rate, so not all hypotheses found to be significant by SGoF are expected to be found significant by Bonferroni. However if any hypotheses are significant by Bonferroni it suggests SGoF's results are not due to clustering randomly small p values.

As SGoF uses the distribution of p values to calculate significance it does not automatically consider a p value of zero to be significant, unlike Bonferroni. Therefore when p values are calculated using bootstrapping (see section 2.2.17) only SGoF will be used.

Table 2.2: Statistical families. This table presents the twelve statistical families used in this study. Each family was tested separately to control family-wise error rate (FWER). Each statistical family also had a control calculated using randomized onset times, except for families 1 and 8 where the data with randomized onset times was instead used to calculate significance cutoffs (see section 2.2.17). As only one hypothesis was tested for resting state data, it is not considered a "family." See Table 2.3 for more details. The columns include:

Mask creation: Method of creating default mode and task positive network masks. Either the entire fMRI run or a 12.3s window centered on the peristimulus time was used.

Metric type: "Masks" is comparison between the probability of a voxel occurring in a fast performance group's masks and a slow performance group's masks. Mag. dif. is difference in magnitude between the default mode and task positive networks' mean signals at the peristimulus time. 12.3s r is correlation between the default mode and task positive networks' signals in a window of 12.3 seconds centered at the peristimulus time. DMN (default mode network) and TPN (task positive network) is the mean signal in that network at the peristimulus time.

Test type: "Two group" is where instances of task performance were divided into two groups for comparison, in both an inter-individual and an intra-individual manner. "Linear" is where metrics were compared with reaction time using linear regression. "Fast" or "slow" indicates that only individuals either faster than or slower than the overall median reaction time were used.

SGoF significance: With the exception of the "Mask" metric, significance was tested using SGoF correction for FWER at 0.05, 0.1 and 0.005. (* The mask metric was tested using only 0.05). The lowest probability cutoff where significance was found is shown, or "None" if no results passed SGoF correction at 0.05 FWER.

Family number: Reference numbers for each statistical family.

Mask creation	Metric type	Test type	SGoF significance	Family Number
Entire run	Masks	Two group	None	1
Entire run	Mag.dif. & 12.3s r	Linear	≤ 0.05	2
Entire run	Mag.dif. & 12.3s r	Two group	≤ 0.005	3
Entire run	Mag.dif. & 12.3s r	Two group, Fast	≤ 0.005	4
Entire run	Mag.dif. & 12.3s r	Two group, Slow	≤ 0.05	5
Entire run	DMN & TPN	Linear	≤ 0.005	6
Entire run	DMN & TPN	Two group	None	7
12.3s window	Masks	Two group	≤ 0.05*	8
12.3s window	Mag.dif. & 12.3s r	Linear	≤ 0.005	9
12.3s window	Mag.dif. & 12.3s r	Two group	≤ 0.005	10
12.3s window	DMN & TPN	Linear	≤ 0.1	11
12.3s window	DMN & TPN	Two group	None	12

Table 2.3: Individual metrics tested. Each table displays individual metrics tested sorted by how the metric was calculated (columns) and how statistical testing was performed on it (rows).

Differences in method of calculation include: (1) Whether masks were generated using entire fMRI runs or only a 12.3s window centered on the peristimulus time, (2) Whether a linear fit was performed between reaction time and the metric, or if two groups were used. The two groups could be determined using either each individual's own median or an overall median. (3) Whether all individuals were used, or only individuals whose median reaction time fell above (slow) or below (fast) the overall median reaction time.

The metrics that were calculated include: (1) comparison of probability of a voxel falling within a mask for a fast performance group versus a slow performance group, (2) correlation between mean network signals in a 12.3s window centered around the peristimulus time, (3) difference in magnitude between mean network signals at the peristimulus time, (4) mean default mode network signal at the peristimulus time, and (5) mean task positive network signal at the peristimulus time.

a) Individual metrics by most significant result and statistical family. A symbol showing the most significant result from this metric, followed by the family of hypotheses to which it belongs (see Table 2.2). Symbols are as follows:
X This test was not performed
O No results passed correction for multiple comparisons
* Passes SGoF at 0.05
** Passes SGoF at 0.01
*** Passes SGoF at 0.005
† Passes standard Bonferroni correction at 0.05

Mask creation	Testing method	Indivi-duals used	Masks (0.05 only)	Short-window r	Magni-tude difference	Default mode signal	Task positive signal
Entire fMRI runs	Linear fit	All	X	* (2)	* (2)	O (6)	***† (6)
Entire fMRI runs	Two groups, overall median	All	O (1)	***† (3)	** (3)	O (7)	O (7)
Entire fMRI runs	Two groups, individual medians	All	O (1)	* (2)	** (2)	O (7)	O (7)
Entire fMRI runs	Two groups, individual medians	Fast	X	***† (4)	* (4)	X	X
Entire fMRI runs	Two groups, individual medians	Slow	X	O (5)	* (5)	X	X
12.3s window	Linear fit	All	X	***† (9)	** (9)	** (11)	O (11)
12.3s window	Two groups, overall median	All	* (8)	***† (10)	O (10)	O (12)	O (12)
12.3s window	Two groups, individual medians	All	* (8)	O (10)	O (10)	O (12)	O (12)

(Table 2.3 continued on next page.)

35

(Table 2.3 continued from previous page.)

(b) Individual metrics by figure number. The figure number to which this metric corresponds. "O" indicates no figure.

Mask creation	Testing method	Indivi-duals used	Masks (0.05 only)	Short-window r	Magni-tude difference	Default mode signal	Task positive signal
Entire fMRI runs	Linear fit	All	X	2.5d	2.5c	2.9b	2.9b
Entire fMRI runs	Two groups, overall median	All	O	2.5b	2.5a	2.9a	2.9a
Entire fMRI runs	Two groups, individual medians	All	O	2.6b	2.6a	2.9c	2.9c
Entire fMRI runs	Two groups, individual medians	Fast	X	2.7d	2.7c	X	X
Entire fMRI runs	Two groups, individual medians	Slow	X	2.7b	2.7a	X	X
12.3s window	Linear fit	All	X	2.10bF	2.10bE	2.10bD	2.10bD
12.3s window	Two groups, overall median	All	2.10a	2.10bC	2.10bB	2.10bA	2.10bA
12.3s window	Two groups, individual medians	All	2.10a	O	O	O	O

_____

2.2.15 Control

The type of functional imaging run (resting state vs. PVT), change onsets and response times were randomly permuted between all functional imaging runs and all subjects. These randomly permuted behavioral data were compared to original-order BOLD data using the signal change and comparative metrics. Other than randomization of behavioral data, analysis was identical to the descriptions above, including separate control of family-wise error rate for each family of hypotheses.

Table 2.2 illustrates the twelve families of hypotheses that were included in this study. Excluding families one and eight, ten families had a control significance test

36

performed. From ten families, it is likely (40.1% chance, from binomial distribution) that at least one will show a false positive, but less than 5% likely (1.15%, from binomial distribution) that three will show a false positive. Therefore if more than three control tests show a false positive, it suggests that there was a methodological error in significance testing.

2.2.16 Cross-validation

This study is investigative and not intended to optimize a predictive model. Nevertheless, it is informative to run cross validation on at least some of the above predictive metrics to test if results are viable as a predictive metric in the future. For simplicity, and to have the best chance of showing predictive validity, only the metric found with the lowest *p* value resulting from a T test was tested.

The set of values for the selected metric, calculated at each instance of task performance, was divided into two groups. For the first group, a linear boundary was calculated in *MATLAB* to separate the fast response instances and the slow response instances. This boundary was tested on the second group. This was repeated 1,000 times and mean percentage correct classification (number of instances classified in correct group divided by total number of instances), slow specificity (number of true slow instances divided by number of instances classified as slow) and fast specificity (number of true fast instances divided by number of instances classified as fast) (Harrell, Califf et al. 1982) mean values taken over all repeats.

2.2.17 Artificial null distribution for mask significance level

Using control data with randomized onset times (see above) the difference in probability of a voxel being in a mask between fast performers and slow performers was calculated for each voxel. For masks generated in 12.3s windows, it was also calculated at each peristimulus time. This distribution of differences can be considered to be a null distribution with regards to fast versus slow performance. Resting state data and data in 12.3s windows had their null distributions calculated separately.

Any value which falls between the minimum and maximum values of the null distribution can be converted to a p value by converting it to a percentile of the null distribution. Any value falling outside of the null distribution can be considered to have a p value of zero. Here, p values were calculated in a two tailed manner based on percentile of center: one is center (50th percentile) of null distribution; zero is either tail of null distribution. As Bonferroni FWER correction cannot be determined on p values of zero, only SGoF FWER correction will be used in this case.

2.3 Results

Twenty-two functional imaging runs were removed due to excess motion, resulting in exclusion of two individuals. One functional imaging run was removed due to the required network size being larger than the entirety of gray matter, preventing the creation of network masks. The final number of functional imaging runs was 45 (from 68) over 15 individuals (from 17). Based on the peristimulus time tested, a total of

between 131 and 136 instances occurred per usable peristimulus time within these 45 remaining functional imaging runs.

Maps of the default mode and task positive networks were successfully obtained in all functional imaging runs for all remaining individuals. Figure 2.2 shows probability maps illustrating how often any given voxel was placed within a mask. In this figure all masks were registered using per-slice, rigid-body registration to demonstrate their similarity across subjects (Sochor, http://www.mathworks.com/matlabcentral/fileexchange/19086), though further analysis was performed in individual space. The majority of masks had co-localized regions corresponding to anatomical regions known to be contained within the default mode network (precuneus, angular gyri and medial prefrontal cortex) and the task-positive network (dorsolateral prefrontal cortex, inferior parietal cortex and premotor cortex). Masks created from PVT and from resting state functional imaging runs are similar, suggesting that task performance minimally perturbs the definition of the networks. Figure 2.3 shows masks created from a single functional imaging run from one individual and the mean BOLD time-course within these masks. As expected, these mean time courses are generally anti-correlated (changing in a similar manner but with opposite sign) yet the degree to which they are anti-correlated varies over the functional imaging run (Kelly, Uddin et al. 2008).

Overall median reaction time was 971ms; excluding the central 5% of reaction times resulted in instances faster than 939ms classified as fast and instances slower than 1014ms classified as slow. Individual median reaction times varied, with the mean individual median reaction time at 1,060ms with standard deviation 613ms. Using an

39

overall median, within the group of fast response instances mean reaction time was 697ms with standard deviation 125ms; within the group of slow response instances mean reaction time was 2,001ms with standard deviation 1,332ms. Using a median for each individual, within the group of fast response instances mean reaction time was 888ms with standard deviation 365ms; within the group of slow response instances mean reaction time was 1,778ms with standard deviation 1,413ms.

Figure 2.4a shows a histogram of reaction times. In Figure 2.4b these are separated into whether there was positive or negative correlation between the signals from the two networks in a 12.3s window centered at the change onset (not corrected for hemodynamic response delay). The overall median reaction time of 971ms is shown as a light dashed line. 971ms is approximately centered in the large leftmost cluster of reaction times. To the left of 971ms most bins are dominated by negative correlation, to the right most bins are dominated by positive correlation. These results indicate that median was an appropriate criterion for division of instances.
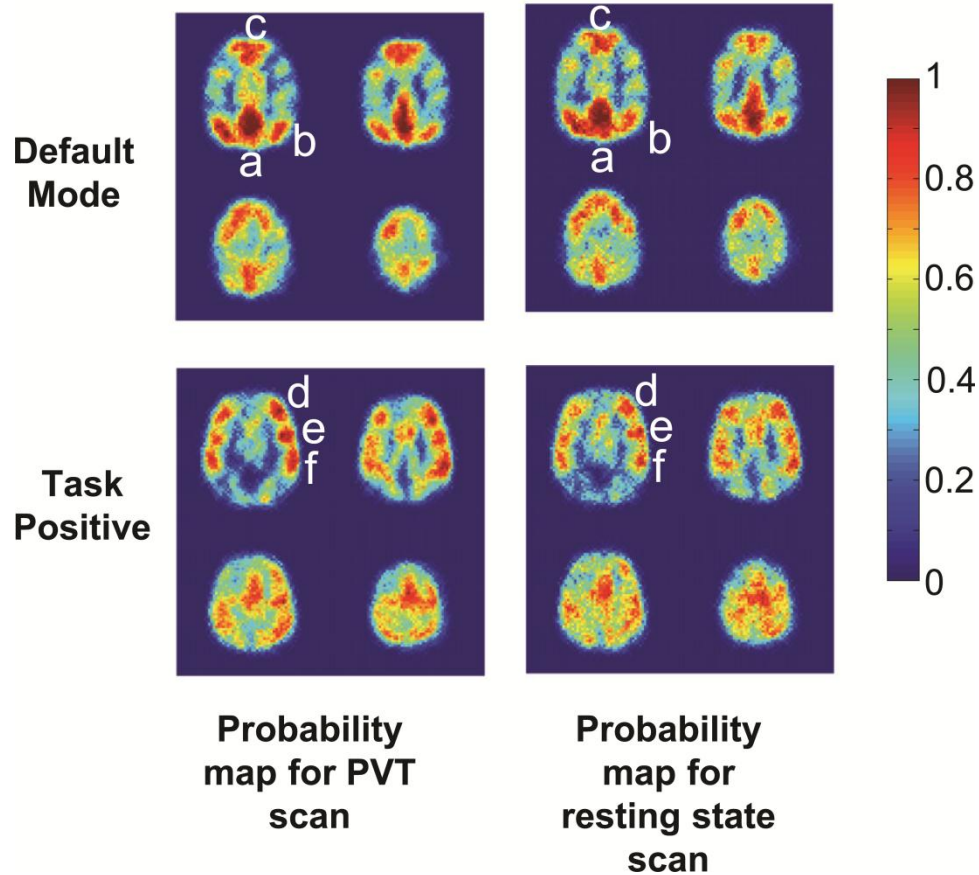
Figure 2.2: Probability maps for generated masks. In this study masks were generated on a per-functional-imaging-run basis due to the high temporal resolution EPI used (method shown in Figure 2.1). Images shown are four transverse image slices from ventral (upper left) to dorsal (lower right) of human individuals with the nose pointing upwards, non-radiological convention. Masks are registered (for visualization purposes only) using rigid-body registration (Sochor, http://www.mathworks.com/matlabcentral/fileexchange/19086) of co-registered anatomical images on a per-slice basis. Probabilities are shown that any given voxel exists in any given mask of the default mode network or the task positive network, in either the masks generated for PVT or resting-state functional imaging runs. Zero (dark blue) indicates that the voxel never appears in that location, one (dark red) indicates that the voxel always appears in that location, 0.5 (light green) indicates that the voxel appears in half of all masks. The top row shows probabilities for masks generated for the default mode network, the bottom row the task positive network. The first column shows probabilities for masks generated from PVT functional imaging runs, the second column resting-state functional imaging runs. Compare masks to Figure 5 in Fransson (Fransson 2005). Anatomical brain locations can be seen for the default mode network corresponding to **(a)** precuneus **(b)** angular gyri **(c)** medial prefrontal cortex, and for the task-positive network corresponding to **(d)** dorsolateral prefrontal cortex **(e)** premotor cortex **(f)** inferior parietal cortex.

41
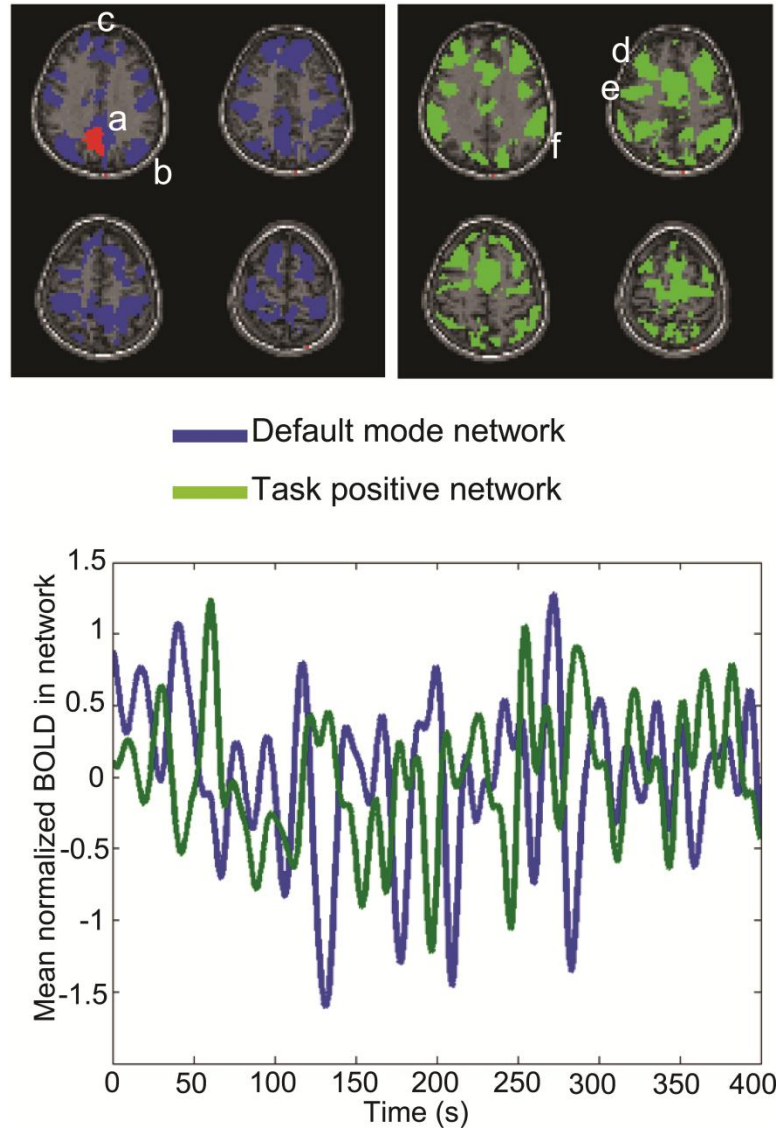
Figure 2.3: Example masks and mean time courses. Example masks are shown for the first individual, first PVT functional imaging run. Images shown are four transverse image slices from ventral (upper left) to dorsal (lower right) of one individual with the nose pointing upwards, non-radiological convention. The masks are shown against co-registered anatomical T1 weighted MPrage images. The mask on the left, shown in blue, is for the default-mode network and anatomical brain locations can be seen corresponding to **(a)** precuneus **(b)** angular gyri **(c)** medial prefrontal cortex. The ventral left precuneus seed region used to generate these masks is shown in red. The mask on the right, shown in green, is for the task-positive network and anatomical brain locations can be seen corresponding to **(d)** dorsolateral prefrontal cortex **(e)** premotor cortex **(f)** inferior parietal cortex. The mean time course from each of these masks is plotted with the mean signal from the default mode network in blue and the mean signal from the task positive network in green. Note that while in general the two signals are anti-correlated, the degree of anti-correlation appears to vary over time (Kelly, Uddin et al. 2008).

www.manaraa.com
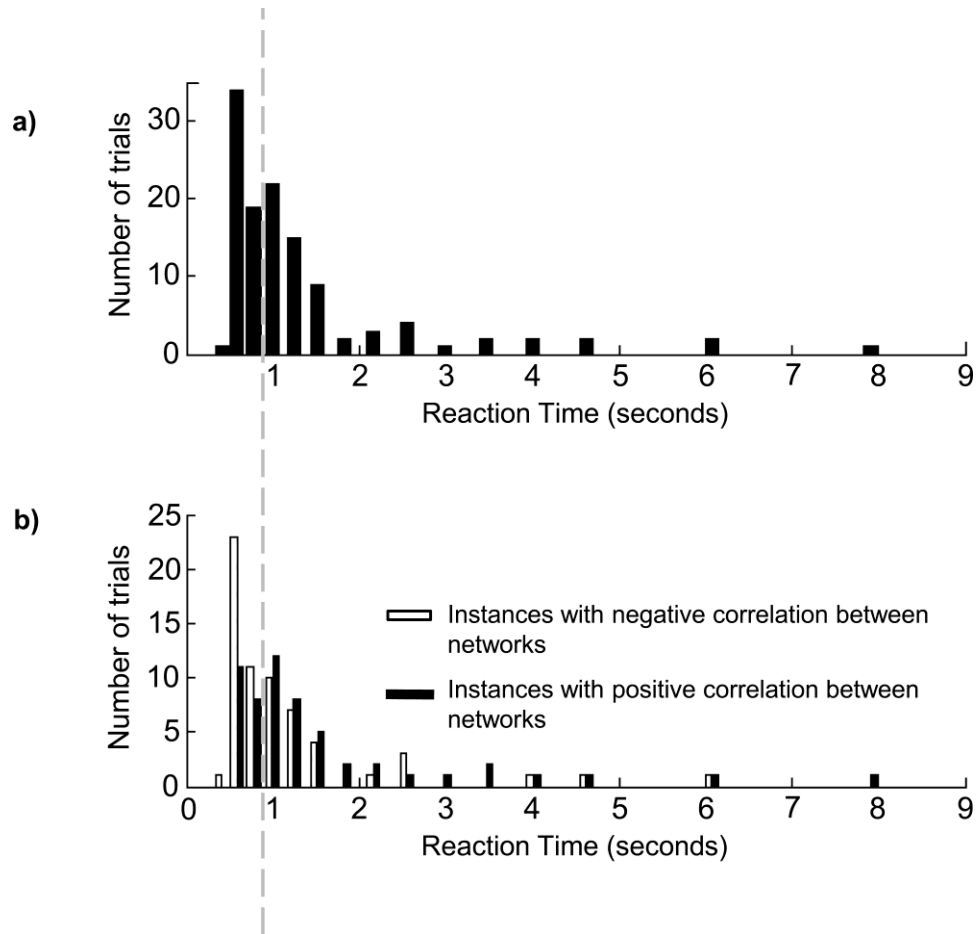
Figure 2.4: Histograms of reaction times on PVT. Number of instances of the PVT where individuals responded within a bin of possible reaction times is plotted as a histogram versus the entire possible range of reaction times from 0s to 9s. The twenty bin centroids are exponentially distributed from 0s to 9s. **(a)** Reaction times are shown together in each bin **(b)** Each bin is separated into 2 new bins based upon Pearson product-moment correlation coefficient (*r*) between the default mode network and the task positive network in a 12.3s window around the change onset (equivalent to 0s peristimulus time on Figure 2.5b; approximately 4s before the expected hemodynamic response to neural activity due to task performance, see Miezin, Maccotta et al. 2000) before PVT performance where reaction time was measured. If correlation is negative, the instance is placed in the white bin on the left; if positive the instance is placed in the black bin on the right.

The dashed line indicates the overall median reaction time (971ms). Note that it is centered within the large distribution on the left side of the histogram. Also note that to the left of this median instances with negative correlation between networks dominate, while to the right of this median instances with positive correlation between networks dominate.

43

2.3.1 Inter-individual prediction using comparative metrics (Figure 2.5)

Figure 2.5 illustrates how comparative metrics relate to inter-individual performance at peristimulus times from 16s before change onset to 24s after. The first comparative metric is *local difference in magnitude*, the signal in the task positive network subtracted from the signal in the default mode network at the peristimulus time around the instance; it is shown in Figures 2.5a and 2.5c. The second comparative metric is *short window correlation*, which is *r* in a 12.3s window centered at the peristimulus time around the instance; it is shown in Figures 2.5b and 2.5d. In figures 2.5a and 2.5b individual instances are separated into slow and fast response groups by the overall median response time, and the metrics from each group are plotted. Error bars are one standard error. In figures 2.5c and 2.5d linear regression was performed between the metrics and reaction time (using all response instances), and R^2 values are plotted.

Unlike prediction using signal change (shown in Figure 2.9), prediction using comparative metrics (Figure 2.5) shows many significant differences prior to change onset (0s) or the expected hemodynamic response to neural activity (4s).

For fast vs. slow group analysis, tests passing SGoF correction at 0.05 FWER included: using magnitude difference at peristimulus times of 4s and 6s (fast response greater negative difference indicating task positive signal was greater, $p = 1.60 \times 10^{-2}$, 5.36×10^{-3}), and using short-window correlation at peristimulus times of -16s to -6s and 0s to 16s (fast response greater negative correlation, $3.28 \times 10^{-4} \leq p \leq 1.13 \times 10^{-2}$). Two of these tests passed Bonferroni correction: separating instances by overall median response time and using short-window correlation at peristimulus times of -12s and -10s (fast response greater negative correlation, $p = 4.59 \times 10^{-4}$, 3.28×10^{-4}).

44

For linear analysis, tests passing SGoF correction at 0.05 FWER included: magnitude difference at peristimulus times of -6s and -4s (p = 2.11×10^{-2}, 9.69×10^{-3}, $R^2 = 4.43 \times 10^{-2}$, 5.52×10^{-2}, negative slope suggesting slower performance is related to lower default mode minus task positive) and at peristimulus times of 4s to 8s ($2.95 \times 10^{-3} \leq p \leq 2.42 \times 10^{-2}$, $4.38 \times 10^{-2} \leq R^2 \leq 7.56 \times 10^{-2}$, positive slope suggesting slower performance is related to greater default mode minus task positive) and using short-window correlation at peristimulus times of -12s, -8s to -2s, 2s and 4s ($1.23 \times 10^{-2} \leq p \leq 2.77 \times 10^{-2}$, $4.13 \times 10^{-2} \leq R^2 \leq 5.19 \times 10^{-2}$, positive slope suggesting slower performance is related to greater correlation).

2.3.2 Intra-individual prediction using comparative metrics (Figure 2.6)

Figure 2.6 illustrates how comparative metrics relate to intra-individual performance at peristimulus times from 16s prior to 24s succeeding change onset. The first comparative metric is *local difference in magnitude* which is the signal in the task positive network subtracted from the signal in the default mode network at the peristimulus time around the instance; it is shown in Figure 2.6a. The second comparative metric is *short window correlation* which is *r* in a 12.3s window centered at the peristimulus time around the instance; it is shown in Figure 2.6b. Individual instances are separated into slow and fast response groups by each individual's own median response time, and the metrics from each group are plotted. Error bars are one standard error.

45
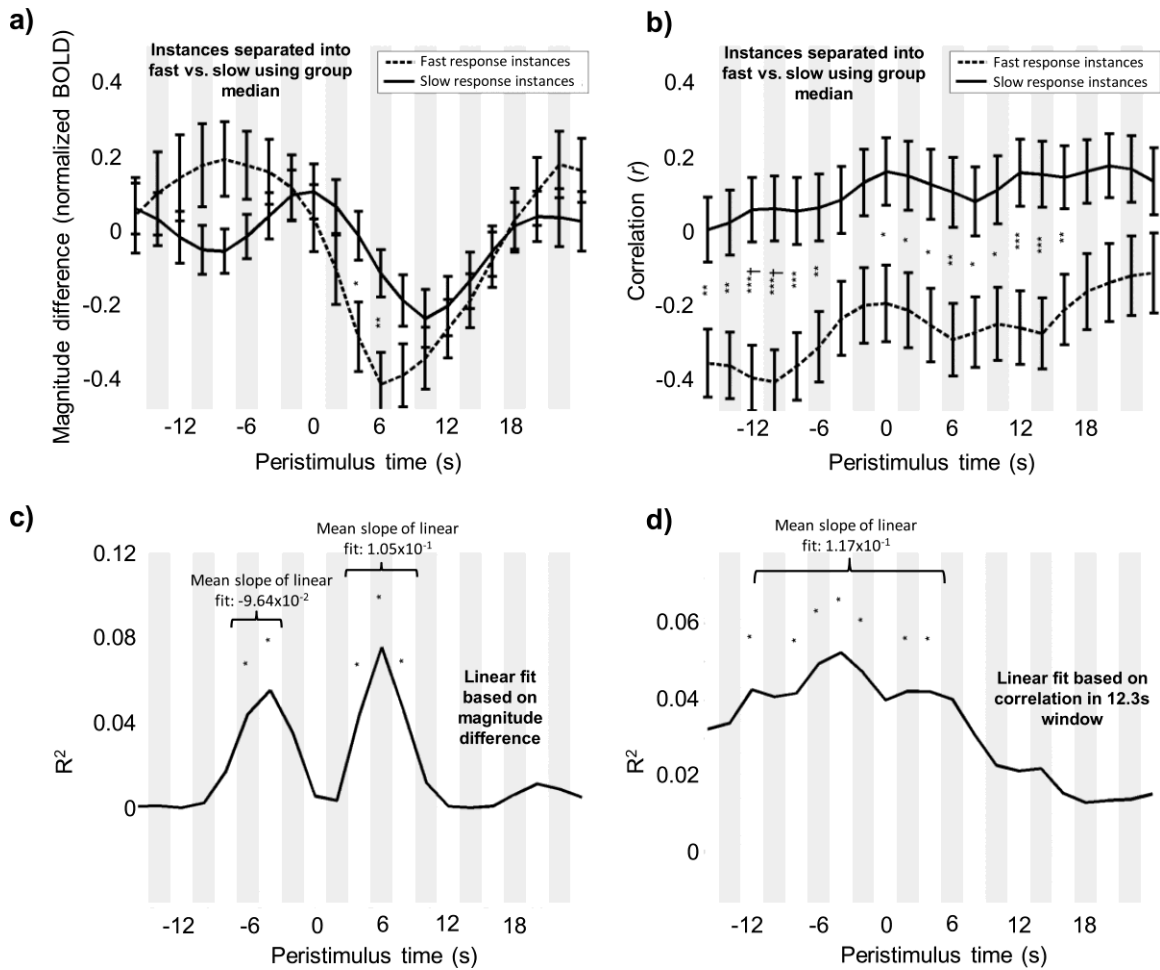
Figure 2.5: Inter-individual results from comparative metrics.

a) Mean signal in default mode network with mean signal in task positive network subtracted from its value. Instances faster than the overall median reaction time are shown as dashed lines; instances slower than the overall median reaction time are shown as solid lines. X axis is the amount of time between the calculated value and the change onset cue to perform the task (negative is prior to task, positive is succeeding task). Error bars are one standard error.

b) Pearson product-moment correlation coefficient (*r*) for 12.3s square window between mean default mode network signal and mean task positive network signal. Instances faster than the overall median reaction time are shown as dashed lines; instances slower than the overall median reaction time are shown as solid lines. X axis is the amount of time between the calculated value and the change onset cue to perform the task (negative is prior to task, positive is succeeding task). Error bars are one standard error.

(Caption continued on next page)

(Figure 2.5 Caption continued)

c) R^2 values for linear regression (using all response instances) between reaction time and mean signal in default mode network with mean signal in task positive network subtracted from its value. X axis is the amount of time between the calculated value and the change onset cue to perform the task (negative is prior to task, positive is succeeding task).

d) R^2 values for linear regression (using all response instances) between reaction time and Pearson product-moment correlation coefficient (*r*) for 12.3s square window between mean default mode network signal and mean task positive network signal. X axis is the amount of time between the calculated value and the change onset cue to perform the task (negative is prior to task, positive is succeeding task).

Comparisons found to be significant are shown include magnitude difference at peristimulus times of -6s, -4s and 4s to 8s, correlation at peristimulus times of -16s to 16s. They are demarcated as follows:
* Passes SGoF at 0.05
** Passes SGoF at 0.01
*** Passes SGoF at 0.005
† Passes standard Bonferroni correction at 0.05

_____

Unlike inter-individual comparisons (Figure 2.5), intra-individual comparisons (Figure 2.6) isolate significant results to only peristimulus times prior to task performance. This is the logically expected result, as signals from different individuals could conceptually vary over the entire scan in a manner reflecting the overall performance of that individual. Conversely, fluctuations within the same individual that are relevant to the task must be temporally localized to the task in some manner, otherwise they would be inherent to the individual as a whole and thus couldn't be related to only specific time points around the task.

47
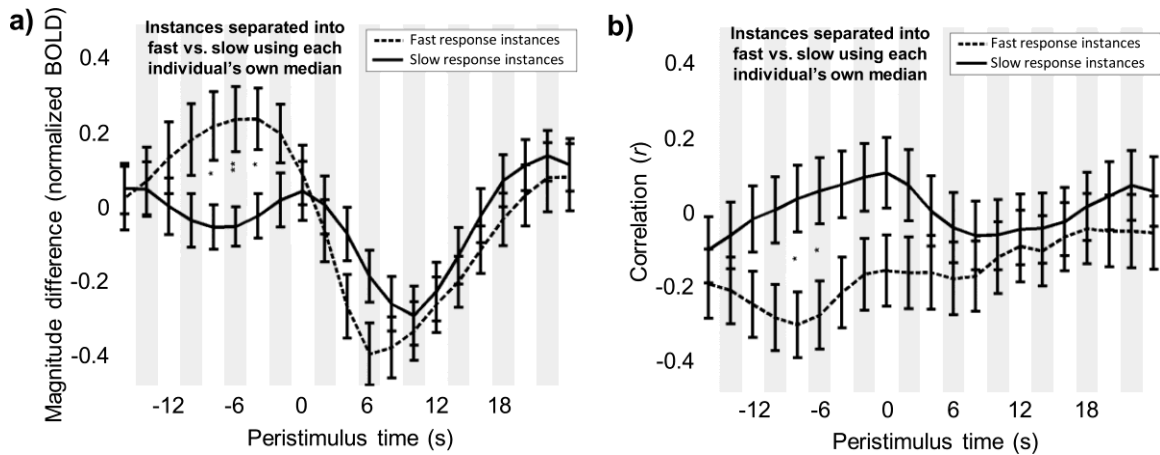
Figure 2.6: Intra-individual results from comparative metrics.

a) Mean signal in default mode network with mean signal in task positive network subtracted from its value. Instances faster than each individual's median reaction time are shown as dashed lines; instances slower than each individual's median reaction time are shown as solid lines. X axis is the amount of time between the calculated value and the change onset cue to perform the task (negative is prior to task, positive is succeeding task). Error bars are one standard error.

b) Pearson product-moment correlation coefficient (*r*) for 12.3s square window between mean default mode network signal and mean task positive network signal. Instances faster than each individual's median reaction time are shown as dashed lines; instances slower than each individual's median reaction time are shown as solid lines. X axis is the amount of time between the calculated value and the change onset cue to perform the task (negative is prior to task, positive is succeeding task). Error bars are one standard error.

Comparisons found to be significant include magnitude difference at -8s to -4s and correlation at -8s to -6s. They are demarcated as follows:
* Passes SGoF at 0.05
** Passes SGoF at 0.01
*** Passes SGoF at 0.005
† Passes standard Bonferroni correction at 0.05

Tests passing SGoF correction at 0.05 FWER included: using magnitude difference at peristimulus times of -8s to -4s (fast response greater positive difference indicating default mode signal was greater, $4.15 \times 10^{-3} \leq p \leq 1.21 \times 10^{-2}$), and using short-window correlation at peristimulus times of -8s and -6s (fast response greater negative correlation, $p = 8.78 \times 10^{-3}$, 1.03×10^{-2}).

2.3.3 Intra-individual prediction within fast and slow groups (Figure 2.7)

Figure 2.7 illustrates how comparative metrics relate to intra-individual performance at peristimulus times from -8s to -4s, when fast and slow individuals are separated. These peristimulus times were chosen as these were the only points significant for prior intra-individual analysis (see -8s to -4s on Figure 2.6). The first comparative metric is *local difference in magnitude* which is the signal in the task positive network subtracted from the signal in the default mode network at the peristimulus time around the instance; it is shown in Figures 2.7a and 2.7c. The second comparative metric is *short window correlation* which is r in a 12.3s window centered at the peristimulus time around the instance; it is shown in Figures 2.7b and 2.7d. Individuals are first separated into slow and fast groups first by the overall median response time, then individual instances within each group are sub-divided into fast and slow response groups using each individual's own median response time. The metrics from each sub-group are plotted. Figures 2.7a and 2.7c are for the slow individuals group while Figures 2.7b and 2.7d are for the fast individuals group. Error bars are one standard error.

49
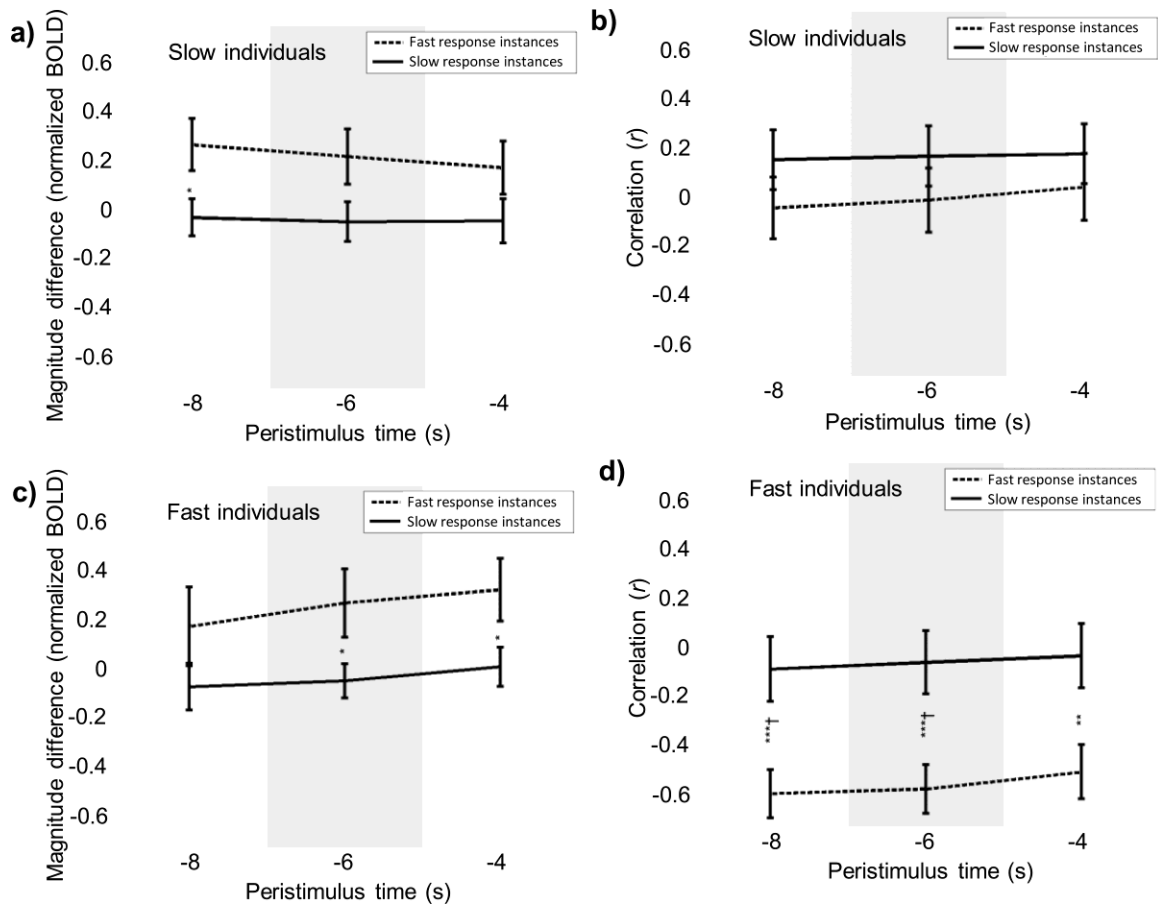
Figure 2.7: Intra-individual results at previously significant peristimulus times for fast and slow groups. Peristimulus times of -8s to -4s are analyzed, as these were the only peristimulus times significant for intra-individual analysis.

a) Mean signal in default mode network with mean signal in task positive network subtracted from its value. Instances faster than each individual's median reaction time are shown as dashed lines; instances slower than each individual's median reaction time are shown as solid lines. X axis is the amount of time between the calculated value and the change onset cue to perform the task (negative is prior to task, positive is succeeding task). Error bars are one standard error. Only instances from individuals whose own median response time was above the overall median response time are used (slow individuals group).

(Caption continued on next page)

50

(Figure 2.7 caption continued)

b) Pearson product-moment correlation coefficient (*r*) for 12.3s square window between mean default mode network signal and mean task positive network signal. Instances faster than each individual's median reaction time are shown as dashed lines; instances slower than each individual's median reaction time are shown as solid lines. X axis is the amount of time between the calculated value and the change onset cue to perform the task (negative is prior to task, positive is succeeding task). Error bars are one standard error. Only instances from individuals whose own median response time was above the overall median response time are used (slow individuals group).

c) As (a); except only instances from individuals whose own median response time was below the overall median response time are used (fast individuals group).

d) As (b); except only instances from individuals whose own median response time was below the overall median response time are used (fast individuals group).

Comparisons found to be significant include magnitude difference at -8s for slow individuals, and magnitude difference at -6s and -4s and correlation at -8s to -4s for fast individuals. They are demarcated as follows:
* Passes SGoF at 0.05
** Passes SGoF at 0.01
*** Passes SGoF at 0.005
† Passes standard Bonferroni correction at 0.05
_____

Tests passing SGoF correction at 0.05 FWER included: within the slow individuals group using magnitude difference at a peristimulus time of -8s (fast response greater positive difference indicating default mode signal was greater, $p = 2.32 \times 10^{-2}$), within the fast individuals group using magnitude difference at peristimulus times of -6s and -4s (fast response greater positive difference indicating default mode signal was greater, $3.57 \times 10^{-2} \leq p \leq 3.70 \times 10^{-2}$) and within the fast individuals group using short-window correlation at peristimulus times of -8s to -4s (fast response greater negative correlation, $3.44 \times 10^{-3} \leq p \leq 9.65 \times 10^{-3}$).

51

Two tests passed Bonferroni correction within the fast individuals group. These were short-window correlation at peristimulus times of -8s and -6s (fast response greater negative correlation, $3.44 \times 10^{-3} \leq p \leq 4.39 \times 10^{-3}$).

In every case whether the mean value for fast instances was greater or less than the mean value for slow instances matched what was seen when the groups were combined (Figure 2.6).

2.3.4 Resting state correlation (Figure 2.8)

Using the traditional analysis method of correlation between networks on the time scale of entire resting state functional imaging runs (Kelly, Uddin et al. 2008; Albert, Robertson et al. 2009; Tambini, Ketz et al. 2010; Wang, Laviolette et al. 2010) a significant relationship was shown between faster reaction times and anti-correlation between the default mode and task positive networks. This was similar to what was seen using short-window correlation (see section 2.3.1) and what has been observed in other attention-requiring tasks (Kelly, Uddin et al. 2008). This is shown in Figure 2.8.

Individuals were divided into two groups based on whether their mean reaction time was above or below the overall median reaction time of 971ms. The "fast" group of individuals (with below 971ms reaction times) had mean negative correlation between their default mode network and task positive networks' signals, correlated over entire fMRI resting state runs (mean $r = -0.134$, standard deviation 0.408). The "slow" group of individuals (with above 971ms reaction times) had mean positive correlation (mean $r =$

0.333, standard deviation 0.312). This difference was significant when the two groups were compared with a student's t-test ($p = 6.05\text{x}10^{-3}$).

No significant relationship was found between masks generated for fast performers versus slow performers, when the whole functional imaging run was used to generate the mask (see section 2.3.6).

_____
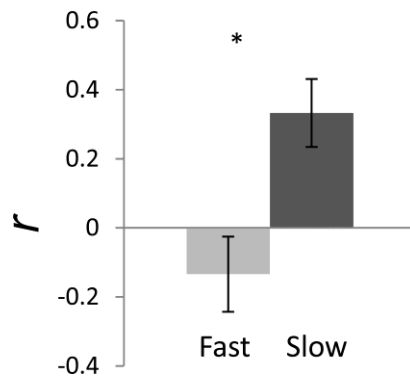
Figure 2.8: Resting state results. The Pearson product-moment correlation coefficient was calculated between the mean signal from the default mode network and the mean signal from the task positive network in each resting state functional imaging run. The mean *r* is shown for (left) individuals whose own median response time was less than the overall median response time and (right) individuals whose own median response time was greater than the overall median response time. Error bars are one standard error. This difference was significant ($p = 6.05\text{x}10^{-3}$).

2.3.5 Prediction using signal change (Figure 2.9)

Figure 2.9 shows how the mean signal within each network relates to intra-individual performance at peristimulus times relative to change onset from 16s prior to 24s succeeding. Error bars are one standard error. Individual instances are separated into slow and fast response groups. Figure 2.9a has instances separated by the overall median response time and plots mean signal for each group. Figure 2.9b uses linear regression between mean signal and reaction time and plots R^2 values. Figure 2.9c has instances separated on a per-individual level by each individual's median response time and plots mean signal for each group.

For two-group analyses, no significant differences were observed between slow and fast response groups when corrected using SGoF or Bonferroni methods at 0.05 FWER. Four p values were less than 0.05 (default mode compared to overall median response time 8s prior, default mode compared to individuals' own median response times at 8s to 6s prior, task positive compared to individuals' own median response times at 4s prior, $3.40 \times 10^{-2} \leq p \leq 4.89 \times 10^{-2}$), however this is what is expected in a random distribution (84 hypotheses / [1 / 0.05] = 4.2 hypotheses expected with p values less than 0.05).

For linear analysis, tests passing SGoF correction at 0.05 FWER included: using task positive signal at peristimulus times of 6s, 8s, 18s and 20s ($1.10 \times 10^{-3} \leq p \leq 5.80 \times 10^{-3}$, $6.49 \times 10^{-2} \leq R^2 \leq 8.89 \times 10^{-2}$, negative slope indicating that slower performance is related to lower task positive signal). No tests passed SGoF correction at 0.05 FWER for default mode signal. One test passed Bonferroni correction at 0.05 FWER: using task positive signal at peristimulus time of 18s ($p = 1.10 \times 10^{-3}$, $R^2 = 8.89 \times 10^{-2}$).

54
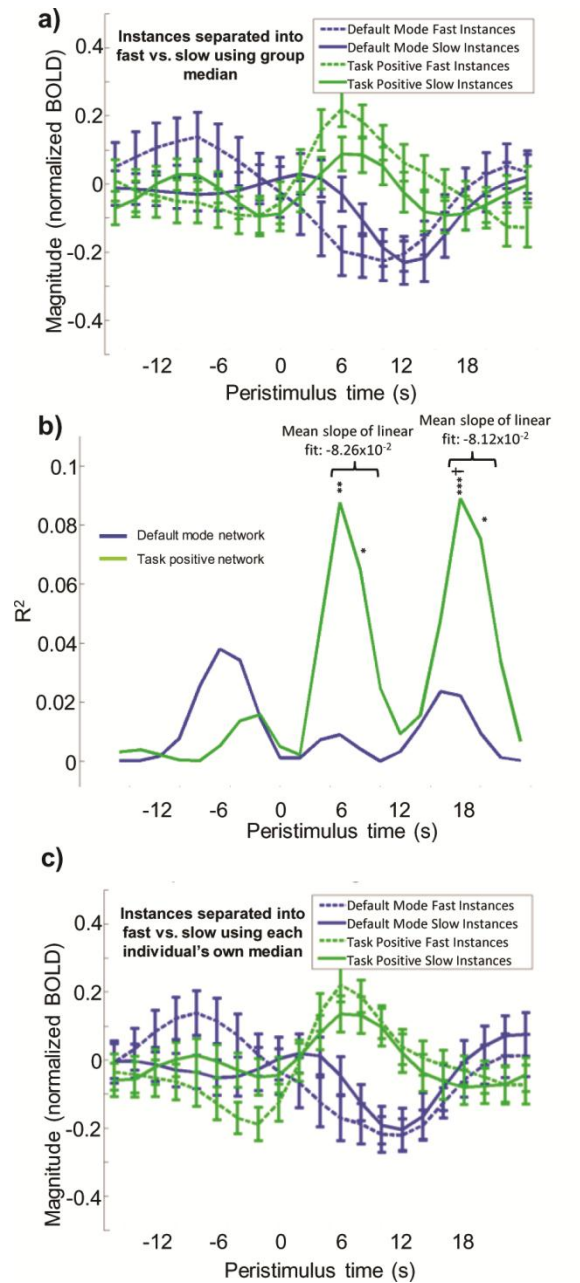
Figure 2.9: Mean signal in network by peristimulus time around task instance.

a) Mean signal in the default mode networks (blue) and task positive networks (green) across each instance of the PVT. Instances faster than the overall median reaction time are shown as dashed lines; instances slower than the overall median reaction time are shown as solid lines. X axis is the amount of time between the mean value in the network and the change onset cue to perform the task (negative is prior to task, positive is succeeding task). Error bars are one standard error.

(Caption continued on next page)

55

(Figure 2.9 caption continued)

b) R^2 values for linear regression between reaction time and mean signal in the default mode networks (blue) and task positive networks (green) across each instance of the PVT. X axis is the amount of time between the mean value in the network and the change onset cue to perform the task (negative is prior to task, positive is succeeding task).

c) As (a); however instances are separated into fast and slow groups using individuals' own median reaction times.

Comparisons found to be significant are shown as follows:
* Passes SGoF at 0.05
** Passes SGoF at 0.01
*** Passes SGoF at 0.005
† Passes standard Bonferroni correction at 0.05

_____

2.3.6 Test for differences in masks

Using the standard masks generated from entire functional imaging runs, no voxels were found with a significant difference in probability maps for fast and slow performance groups.

2.3.7 Generation of Masks in 12.3s Windows (Figure 2.10)

Probability maps are shown for masks generated within 12.3s windows in Figure 2.10a for two peristimulus times (6s prior on left two columns and 6s succeeding on right two columns) and fast and slow groups separated using an overall median value. All probability maps (including both methods of separating fast and slow groups and all peristimulus times) are included as multimedia movie files which use the same scale as Figure 2.10. These masks are less detailed than their counterparts generated using entire

56

functional imaging runs (Figure 2.2) but nevertheless show localized anatomical regions within the default mode network (precuneus, angular gyri and medial prefrontal cortex) and the task-positive network (dorsolateral prefrontal cortex, inferior parietal cortex and premotor cortex). Qualitatively, fast performers' masks (top row) may be more detailed than slow performers' masks (bottom row).

The third row of Figure 2.10a shows significant differences between the fast and slow groups' (separated using an overall median value, inter-individual) probability maps for two peristimulus times (6s prior on left two columns and 6s succeeding on right two columns). All significant differences (including both methods of separating fast and slow groups and all peristimulus times) are included as multimedia movie files which use the same scale as Figure 2.10. Significantly greater values in fast performers are shown as red, significantly greater values in slow performers are shown in blue. Significant values are plotted against mean co-registered anatomical images.

Out of 688,128 potential voxels (128 x 128 x 2 networks x 21 peristimulus times), 9,269 voxels were marked as significantly different between fast and slow groups when these groups were separated using an overall median, 1,671 voxels were marked as significantly different between fast and slow groups when these groups were separated using each individual's own median. While results are noisy, in general fast performance groups showed higher probabilities in areas that would be expected in the network (precuneus in default mode network, or premotor area in task positive network) while slow performance groups showed higher probabilities in areas that would not be expected in the network (precuneus in task positive network, premotor and occipital cortex in default mode network).

57

For prediction, three results were consistent between the masks generated for the entire functional imaging run and the masks generated in 12.3s windows; using two groups separated by an overall median response time with short-window correlation, using linear analysis with short-window correlation and using linear analysis with local difference in magnitude.

For two-group analysis, tests passing SGoF correction at 0.05 FWER included: using short-window correlation and an overall median response time at peristimulus times of -6s to 4s and 10s to 22s (fast response greater negative correlation, $5.10 \times 10^{-5} \leq p \leq 1.66 \times 10^{-3}$). At 0.01 FWER the peristimulus times of -16s and 6s are also within the significant cluster (fast response greater negative correlation, $p = 3.64 \times 10^{-3}$, 2.68×10^{-3}). Tests passing Bonferroni correction at 0.05 FWER included: using short-window correlation and an overall median response time at peristimulus times of 0s to 4s and 12s to 20s (fast response greater negative correlation, $5.10 \times 10^{-5} \leq p \leq 4.59 \times 10^{-4}$).

For linear analysis, tests passing SGoF correction at 0.05 FWER included: using short-window correlation at peristimulus times of -4s, -2s and 4s to 24s ($2.14 \times 10^{-4} \leq p \leq 1.67 \times 10^{-2}$, positive slope suggesting slower performance is related to greater correlation), using local difference in magnitude at peristimulus time of 6s (p = 5.16×10^{-3}, positive slope suggesting slower performance is related to higher default mode minus task positive), using default mode signal at peristimulus times of 16s and 18s (p = 6.41×10^{-3}, 2.36×10^{-3}, negative slope suggesting slower performance is related to lower default mode network signal). Tests passing Bonferroni correction at 0.05 FWER included: using short-window correlation at peristimulus times of 12s to 20s ($2.14 \times 10^{-4} \leq p \leq 5.18 \times 10^{-4}$, positive slope suggesting slower performance is related to greater correlation).

58
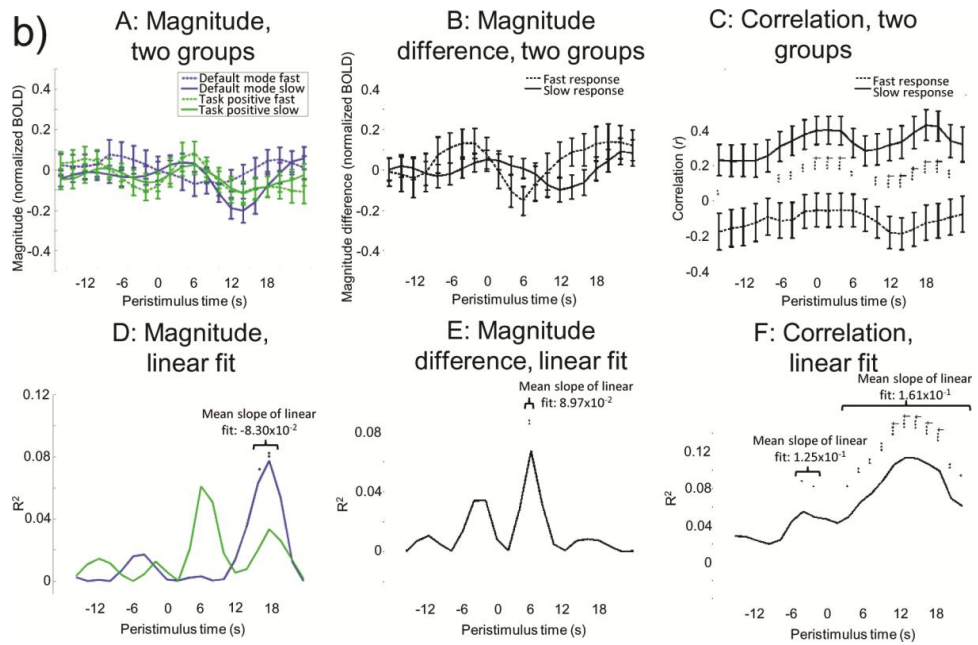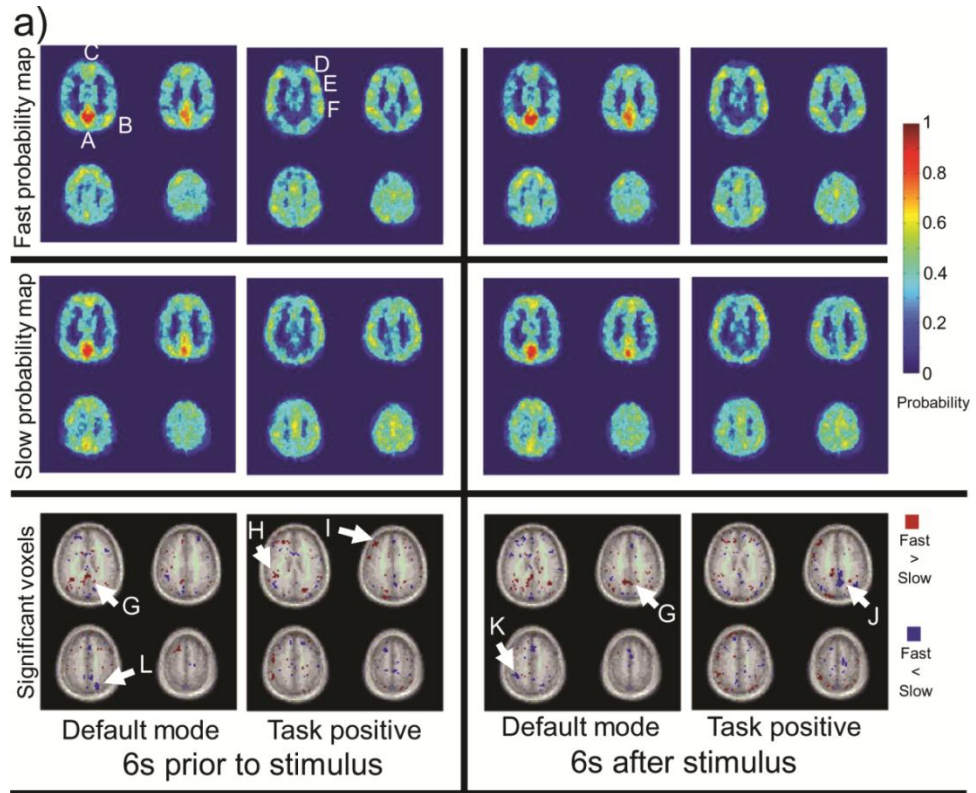
Figure 2.10: Network masks generated in 12.3s windows.

(Caption continued on next page)

(Figure 2.10 caption continued)

(a) Example probability maps and differences between probability maps for network masks generated in 12.3s windows. Probability maps are colored according to the shown scale, with dark blue being a zero or 0% probability indicating that voxel was in no instances' maps, light green being a 0.5 or 50% probability, and dark red being a one or 100% probability, indicating that voxel was in every instances' maps. Peristimulus times of -6s and 6s are shown as representative. All such masks generated can be seen in the multimedia movie files. The first row is probability maps for instances where the individual responded faster than the overall median response time, the second row is where the individual responded slower. The third row is significant differences between the above two rows at $p \leq 0.05$ for SGoF correction using a two-tailed distribution, with red being where the fast group's map's values are significantly greater than the slow group's, and blue being where the slow group's map's values are significantly greater than the fast group's. Moving left to right, the columns are default mode network 6s prior to stimulus, task positive network 6s prior to stimulus, default mode network 6s after stimulus, task positive network 6s after stimulus.

Even though masks are noisier than those generated from entire functional imaging runs (Figures 2.2, 2.3) the same anatomical regions of interest can be seen in each network, in particular for the fast performance group. For the default mode network these include **(A)** precuneus **(B)** angular gyri **(C)** medial prefrontal cortex, and for the task-positive network corresponding to **(D)** dorsolateral prefrontal cortex **(E)** premotor cortex **(F)** inferior parietal cortex.

In general, fast performance groups showed higher probabilities in areas that would be expected in the network. In the default mode network this included the **(G)** precuneus and in the task positive network this included the **(H)** premotor cortex and **(I)** dorsolateral prefrontal cortex. Conversely, slow performance groups tended to show higher probabilities in areas that would not be expected in the network. In the task positive network this included **(J)** the precuneus and in the default mode network this included the **(K)** premotor cortex and **(L)** occipital lobe.

(b) Significant results from replicating Figures 2.5 and 2.6 except using a network mask generated in a 12.3s window around the peristimulus time, rather than a network mask generated using the entire functional imaging run.

(A) Mean signal in the default mode networks (blue) and task positive networks (green) across each instance of the PVT. Instances faster than the overall median reaction time are shown as dashed lines; instances slower than the overall median reaction time are shown as solid lines. X axis is the amount of time between the mean value in the network and the change onset cue to perform the task (negative is prior to task, positive is succeeding task). Error bars are one standard error.

60

(Figure 2.10 caption continued)

(B) Mean signal in default mode network with mean signal in task positive network subtracted from its value. Instances faster than the overall median reaction time are shown as dashed lines; instances slower than the overall median reaction time are shown as solid lines. X axis is the amount of time between the calculated value and the change onset cue to perform the task (negative is prior to task, positive is succeeding task). Error bars are one standard error.

(C) Pearson product-moment correlation coefficient (*r*) for 12.3s square window between mean default mode network signal and mean task positive network signal. Instances faster than the overall median reaction time are shown as dashed lines; instances slower than the overall median reaction time are shown as solid lines. X axis is the amount of time between the calculated value and the change onset cue to perform the task (negative is prior to task, positive is succeeding task). Error bars are one standard error.

(D) R^2 values for linear regression between reaction time and mean signal in the default mode networks (blue) and task positive networks (green) across each instance of the PVT. X axis is the amount of time between the calculated value and the change onset cue to perform the task (negative is prior to task, positive is succeeding task).

(E) R^2 values for linear regression between reaction time and mean signal in default mode network with mean signal in task positive network subtracted from its value. X axis is the amount of time between the calculated value and the change onset cue to perform the task (negative is prior to task, positive is succeeding task).

(F) R^2 values for linear regression between reaction time and Pearson product-moment correlation coefficient (*r*) for 12.3s square window between mean default mode network signal and mean task positive network signal. X axis is the amount of time between the calculated value and the change onset cue to perform the task (negative is prior to task, positive is succeeding task).

Comparisons found to be significant are shown as follows:
* Passes SGoF at 0.05
** Passes SGoF at 0.01
*** Passes SGoF at 0.005
† Passes standard Bonferroni correction at 0.05
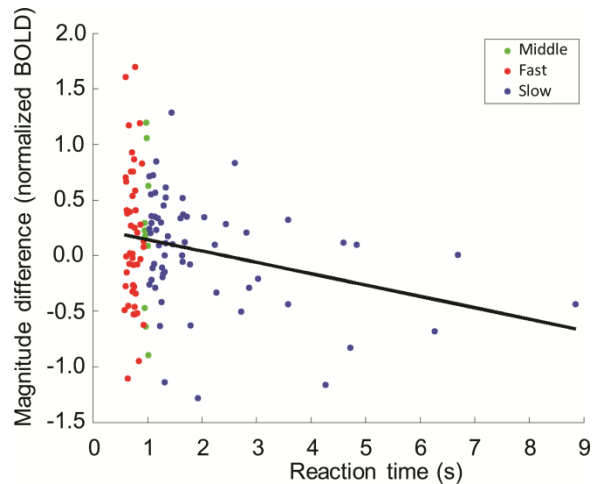
Figure 2.11: Example scatter plot for -4s peristimulus time and magnitude difference. A scatter plot is displayed of reaction time (x axis) and difference in magnitude of normalized BOLD between the default mode and task positive networks (y axis) at -4s peristimulus time. Each response instance is shown as one point. Instances that were classified as "fast" in two-group analysis using an overall median reaction time are shown as red, instances classified as "slow" are shown as blue, and instances not used in two group analysis (instances within the central five percent of reaction times for all individuals) are shown as green. The solid black line is a least-squares linear fit.

Note that while a significant linear trend is reported (see section 2.3.1), it occurs largely due to slow response instances. Fast response instances, however, have high variance and do not clearly show a visible trend.

_____

2.3.8 Linear fit is possible without two-group classification

Significant results at negative peristimulus times for linear analysis but not two group analysis were in part due to that slow response instances followed a linear trend while fast response instances had high variance (Figure 2.11).

2.3.9 Control

No control tests included a *p* value that passed multiple comparisons correction by SGoF or Bonferroni at 0.05 FWER or below. Eight out of ten experimental tests showed significant results at the 5% level. The likelihood of this result being a false positive is vanishingly small (1.61×10^{-9}%, from binomial distribution).

2.3.10 Cross validation

Separating instances by overall median response time and using short window correlation at peristimulus times of -10s had the lowest *p* value resulting from a T test, and thus was chosen as the metric to test for out of sample predictive power using cross validation.

64.5% of instances were correctly predicted from out of sample data from 1,000 runs. Fast instances were diagnosed at 60.2% specificity and slow instances were diagnosed at 70.2% specificity.

2.4 Movies of networks generated within 12.3s windows

There are 14 movies linked here, 10 of probability maps versus peristimulus time, and 4 of significant differences between these probability maps. The movies run through all peristimulus times from -16s to 24s. All movie files are in MPEG (.mpg) format.

2.4.1 Probability maps

The movies linked below are probability maps. They contain the probability of each voxel being in the network mask under the given conditions. The scale is the same as Figure 2.10a.

Figure 2.12: 12.3s window probability maps, default mode, all instances (ProbabilityMaps_All_DMN.mpg, 371K) - This movie contains probability maps for the default mode network from all instances.

Figure 2.13: 12.3s window probability maps, task positive, all instances (ProbabilityMaps_All_TPN.mpg, 380K) - This movie contains probability maps for the task positive network from all instances.

Figure 2.14: 12.3s window probability maps, default mode, fast intra-individual (ProbabilityMaps_IndividualMedians_Fast_DMN.mpg, 401K) - This movie contains probability maps for the default mode network from fast instances. Intra-individual results. Instances are separated into fast versus slow groups using each individual's own median reaction time (see Table 2.1).

Figure 2.15: 12.3s window probability maps, task positive, fast intra-individual (ProbabilityMaps_IndividualMedians_Fast_TPN.mpg, 415K) - This movie contains probability maps for the task positive network from fast instances. Intra-individual results. Instances are separated into fast versus slow groups using each individual's own median reaction time (see Table 2.1).

Figure 2.16: 12.3s window probability maps, default mode, slow intra-individual (ProbabilityMaps_IndividualMedians_Slow_DMN.mpg, 394K) - This movie contains

64

probability maps for the default mode network from slow instances. Intra-individual results. Instances are separated into fast versus slow groups using each individual's own median reaction time (see Table 2.1).

Figure 2.17: 12.3s window probability maps, task positive, slow intra-individual (ProbabilityMaps_IndividualMedians_Slow_TPN.mpg, 400K) - This movie contains probability maps for the task positive network from slow instances. Intra-individual results. Instances are separated into fast versus slow groups using each individual's own median reaction time (see Table 2.1).

Figure 2.18: 12.3s window probability maps, default mode, fast inter-individual (ProbabilityMaps_OverallMedian_Fast_DMN.mpg, 414K) - This movie contains probability maps for the default mode network from fast instances. Inter-individual results. Instances are separated into fast versus slow groups using the overall median reaction time (see Table 2.1).

Figure 2.19: 12.3s window probability maps, task positive, fast inter-individual (ProbabilityMaps_OverallMedian_Fast_TPN.mpg, 426K) - This movie contains probability maps for the task positive network from fast instances. Inter-individual results. Instances are separated into fast versus slow groups using the overall median reaction time (see Table 2.1).

Figure 2.20: 12.3s window probability maps, default mode, slow inter-individual (ProbabilityMaps_OverallMedian_Slow_DMN.mpg, 408K) - This movie contains probability maps for the default mode network from slow instances. Inter-individual

65

results. Instances are separated into fast versus slow groups using the overall median reaction time (see Table 2.1).

Figure 2.21: 12.3s window probability maps, task positive, slow inter-individual (ProbabilityMaps_OverallMedian_Slow_TPN.mpg, 414K) - This movie contains probability maps for the task positive network from slow instances. Inter-individual results. Instances are separated into fast versus slow groups using the overall median reaction time (see Table 2.1).

2.4.2 Significant voxels

The movies linked below contain the significant differences between the probability maps for fast instances versus slow instances. As in Figure 2.10a, red is significantly greater probability for fast instances, blue is significantly greater probability for slow instances. Significance is at $p < 0.05$ using SGoF.

Figure 2.22: 12.3s probability maps, default mode, intra-individual differences (SignificantVoxels_IndividualMedians_DMN.mpg, 334K) - This movie contains significant differences for voxels within the default mode network. Intra-individual results. Instances are separated into fast versus slow groups using each individual's own median reaction time (see Table 2.1).

Figure 2.23: 12.3s probability maps, task positive, intra-individual differences (SignificantVoxels_IndividualMedians_TPN.mpg, 336K) - This movie contains significant differences for voxels within the task positive network. Intra-individual

66

results. Instances are separated into fast versus slow groups using each individual's own median reaction time (see Table 2.1).

Figure 2.24: 12.3s probability maps, default mode, inter-individual differences (SignificantVoxels_OverallMedian_DMN.mpg, 419K) - This movie contains significant differences for voxels within the default mode network. Instances are separated into fast versus slow groups using the overall median reaction time (see Table 2.1).

Figure 2.25: 12.3s probability maps, task positive, inter-individual differences (SignificantVoxels_OverallMedian_TPN.mpg, 428K) - This movie contains significant differences for voxels within the task positive network. Inter-individual results. Instances are separated into fast versus slow groups using the overall median reaction time (see Table 2.1).

2.5 Discussion

2.5.1 Summary of Results

All comparisons consistently demonstrated that a greater difference between the signal in the default mode network and the task positive network predicts faster performance on the PVT. The results from comparing the local difference in magnitude between the two networks suggested that this difference may be directional and bimodal, with greater signal in the default mode network sufficiently prior to the task associated with faster performance and greater signal in the task positive network during or after the task associated with faster performance (Figures 2.5 and 2.6).

67

The relationship between task positive/default mode anti-correlation and fast reaction times is statistically strong and preserved across all time scales. The statistically strongest result (when all peristimulus times were considered) was when an overall median reaction time and correlation in 12.3s windows was used (Figure 2.5b). Masks are also generated within 12.3s windows (rather than entire functional imaging runs). As networks generated in short windows are likely to reflect temporary changes in network dynamics (Honey, Kotter et al. 2007; Deco, Jirsa et al. 2011) these results do not completely match the results from networks generated from entire runs. However, the statistically strongest result is similar even when using these temporary networks (Figure 2.10bC). Therefore the result when only a 12.3s window is considered for both network generation and correlation calculation largely matches the result when the whole functional imaging run is considered for these calculations (Figure 2.8).

Using signal in a single network did not significantly predict PVT performance prior to the task, suggesting relative difference between networks may be more important than absolute signal within a single network (Figure 2.9). The only significant relationships between signal and task performance were seen after the likely neural response to the task itself (Figure 2.9b) and have already been documented in similar tasks (Chee, Tan et al. 2008; Prado, Carp et al. 2011).

Significant results were found at peristimulus times prior to task performance that suggest that speed of response on individual instances of the PVT can be predicted on an instance-by-instance basis for a specific individual, rather than only between different individuals. Significant prior differences in network state were seen using local difference in magnitude and correlation in a 12.3s window for instances separated by each

68

individual's own median reaction time (Figure 2.6). However, a significant predictive difference was not seen when using local difference in magnitude and an overall median reaction time to separate instances (Figure 2.5a) and could only be seen using linear regression, which had higher statistical power (Figure 2.5c). While using an overall median or linear regression and correlation in a 12.3s window shows similar results to using individuals' own medians at peristimulus times of 6s to 8s prior to the task, it also shows similar results at many other peristimulus times not present when medians are calculated separately (Figure 2.5b, d).

While the majority of results agreed that a greater difference between the signal dynamics of the networks is required for optimal response times, two different time scales were observed. Results from resting state correlation (Figure 2.8), correlation within a 12.3s window using an overall median response time (Figure 2.5b) and local difference in magnitude using linear regression (Figure 2.5c) all showed a persistent difference; this difference was significant for 15 out of 21 peristimulus times tested using windowed analysis (with an identical trend for the six non-significant results, Figure 2.5b). However if individual instances were separated into fast and slow groups based on individual median reaction times (so that each individual has approximately half of reaction times classified as fast and half as slow) the comparative metrics only showed a significant difference prior to the change onset within a comparatively small peristimulus time span (Figure 2.6); significant results were isolated to four to eight seconds prior to the change onset.

Further support for the existence of a second, shorter, time scale was that intra-individual prediction was possible even when the analysis only considered individuals

69

who were generally fast or slow (Figure 2.7). When individuals were separated into fast and slow groups, difference in magnitude was still significantly greater for comparatively faster response instances both for generally slow and generally fast responders (Figure 2.7a, c). When only individuals classified as generally fast were used, correlation in a 12.3s window was still significantly more negative for comparatively faster response instances (Figure 2.7d). When only individuals classified as generally slow were used, the mean result for comparatively faster response instances was lower correlation, but the difference was not significant (Figure 2.7b).

2.5.2 The default mode network and anti-correlation

Why does the brain have a default mode, and why would it fluctuate in an anti-correlated manner with regions associated with attention? One possible answer for the first part of this question, which was proposed by the initial work of Raichle et al. (Raichle, MacLeod et al. 2001), is that regions within the default mode network provide useful functions when a subject is at rest. They suggested that the precuneus may gather information and the medial frontal cortex may evaluate its salience. Both the present chapter's results, and previous work (Kelly, Uddin et al. 2008; Prado and Weissman 2011), move us closer to answering the second part of the question (i.e., the purpose for the anti-correlated fluctuations). These studies have demonstrated that performance is optimized when the task-positive and default mode networks are anti-correlated and, conversely, co-activation of the task positive network and the default mode network is detrimental to performance. The mechanism by which anti-correlation results in improved performance requires further study; however some possible answers have

70

already been suggested. One possibility is that anti-correlation itself may not causally affect performance but instead serves as "an index of the degree of regulation of activity in those networks" (p528, Kelly, Uddin et al. 2008); in this case anti-correlation is a biomarker of the underlying processes that regulate behavior. Another possibility is that activity within one functional network may interfere with initiation or sustenance of activity within a different functional network, such as the default mode network interfering during task performance (Eichele, Debener et al. 2008). Anti-correlation creates a situation where cross-activation and hence cross-interference is unlikely.

How then can the brain ensure at least occasional activation of the default mode network, but also discourage co-activation between it and task positive regions? The spatiotemporal dynamics observed in studies by Grigg and Grady and Majeed et al. (Grigg and Grady 2010; Majeed, Magnuson et al. 2011) provide one potential hypothesis. Through repeated, dynamic alternation between default mode and task positive regions, the human brain can both activate the default mode network at some interval and also ensure these activations do not coincide with activations in the task positive network. The present chapter's results thus support the importance of competition between the default mode and task positive functional networks to optimal performance (Kelly, Uddin et al. 2008), but append the important result that this competition varies on a much smaller time scale than had been suspected based on inter-individual studies, and that *intra-individual* behavioral prediction is possible. This time scale is consistent with the spatiotemporal dynamics which take approximately 10 to 20 seconds to switch between networks (Figure 2B in Grigg and Grady, 2010; Figure 5 in Majeed, Magnuson et al. 2011).

71

The present chapter used regression to remove the whole-brain signal prior to analysis. It has been demonstrated that this can potentially create artifactual de-activation resulting in artifactual anti-correlation (Gavrilescu, Shaw et al. 2002). However, recent work by Fox and Zhang et al. demonstrated that the global signal in fMRI is not preferentially located, suggesting regression is unlikely to create artifactual networks; Fox and Zhang et al. also demonstrated that observed anti-correlated networks are highly consistent, suggesting such networks cannot be attributed to global signal removal alone (Fox, Zhang et al. 2009). If anti-correlation was completely artifactual, the network driving behavior should be related to behavior itself; the relationship between the artifactual anti-correlated network and behavior should mimic the network driving behavior with opposite sign and greater noise. However the present chapter does not support this; rather, prior to the task the amount of anti-correlation between networks was significantly related to behavior, whereas the inherent activity within a single network was not (compare Figures 2.5 and 2.9). This supports Fox et al.'s hypothesis of a "biological basis to anticorrelated networks" (p. 3280, Fox, Zhang et al. 2009).

2.5.3 Correlation within entire functional imaging runs vs. 12.3 second windows

Few studies have examined resting state correlation in short time windows; typically the entire fMRI run is used. Sakoğlu et al. used 30s windows in data from patients with schizophrenia as compared to normal controls to find greater diagnostic information than from whole functional imaging runs (Sakoglu, Pearlson et al. 2010). Chang and Glover observed that the low frequency fluctuations which make up functional networks vary in terms of power and dominant frequency band over time

72

(Chang and Glover 2010). A simulation of resting state activity in the Macaque brain by Honey et al. (Honey, Kotter et al. 2007) demonstrated that functional networks gradually change over time if correlation in 30s windows is used as opposed to entire simulated functional imaging runs. A recent review by Deco et al. (Deco, Jirsa et al. 2011) also noted that, in such simulations, correlation coefficients vary based upon the window size used to perform analysis.

The results presented here suggest that the relationship seen in previous work between behavioral differences and entire-functional-imaging-run correlation (Kelly, Uddin et al. 2008) may be a summation of global differences between individuals and numerous low-frequency yet second-scale processes, the latter of which can be examined on their original time scales of only a few seconds. Using the same overall median response times and same mask-generation methods as were used for resting state analysis, the anti-correlation in fast instances was seen at peristimulus times both following and prior to the hypothesized hemodynamic response to neural activity (Figure 2.5b); here about 4s (Miezin, Maccotta et al. 2000). The 12.3s window was short enough such that it could not have contained a full cycle of the fastest fluctuation after filtering. Therefore the anti-correlation which was related to fast responses could only have been based upon momentary differences between networks which can be characterized on a scale of seconds.

On an individual basis, the second-scale relationship between these two networks is also significantly related to behavior, however at fewer peristimulus times. When each individual's own median was used to classify instances as fast or slow, the same effect

73

was seen: greater anti-correlation predicts faster performance. However in this case a significant effect was only seen at 6s to 8s prior to task performance (Figure 2.6b).

2.5.4 Difference in mean signals

A mean signal in the default mode network greater than the mean signal in an anti-correlated network was significantly related to faster response times prior to task performance and slower response times following task performance (Figure 2.5a and 2.6a). However the prior result was significant only if individuals' median reaction times were used and the latter significant only if an overall median reaction time was used. This may be due to intra-individual differences on an instance by instance basis being more predictive of the general waiting state needed to respond quickly: the intra-individual differences in mean occur at 2 out of 3 of the same peristimulus times as intra-individual differences in correlation between networks. Also, as the automatically generated anti-correlated networks include premotor regions (Figures 2.2 and 2.3); a motor response that is similar in all individuals may occlude results unless a global median response time is used. Interestingly, the ideal (fast response) state for the difference in mean signals overall is alternation between networks at approximately 0.05Hz, on the order of what has been observed in studies of spatiotemporal dynamics (Grigg and Grady 2010; Majeed, Magnuson et al. 2011).

74

2.5.5 Comparison to previous research that used distracting stimuli

The present chapter used the PVT. Other investigations into the effects of brain networks on attention have used other tasks, many of which include distracting stimuli. For example, in the flanker task, an individual must respond to a centrally presented target while ignoring surrounding distracting symbols such as arrows or letters (Eriksen and Eriksen 1974).

As the flanker task and the PVT both require an individual to attend to visual stimuli and react with motor movement, results from these tasks should be similar. However, as the flanker task is a two-choice task that involves inhibiting the effects of distracting stimuli, it may require more attentional control to selectively attend to the target location than the PVT. Thus the flanker task may be more reliant on functions associated with task positive brain regions such as inhibition and maintenance of attention (Fox, Snyder et al. 2005; Fransson 2005) while the PVT may be more reliant on function associated with default mode brain regions such as gathering of salient information (Raichle, MacLeod et al. 2001). However there is no reason to believe that competition between networks (Kelly, Uddin et al. 2008) would be desirable in either task, so anti-correlation between networks might be expected in both tasks.

Consistent with this prediction, it was demonstrated by Kelly et al. (Kelly, Uddin et al. 2008) that an individual's ability to maintain an anti-correlated relationship between the default mode network and the task positive network predicted consistent reaction times on a flanker task, suggesting that maintenance of anti-correlation should improve performance. The finding presented in this chapter, that anti-correlation during the resting state predicts lower median response times, demonstrates that this idea extends to the

75

PVT as well. In addition, using the *short-window correlation* metric, a significant difference was found between fast and slow instances on an intra-individual level for individuals classified as fast for resting state analysis, but not for individuals classified as slow (Figure 2.7). This would suggest that individuals who perform optimally are better at modulating competition between networks as Kelly et al. suggested. However, Kelly et al. did not use correlation within windows, but rather maximal change inside 8s windows to look for transient events; they were unable to relate these to performance. Using an even more time-localized method, *local difference in magnitude*, both overall fast and overall slow performers on the PVT did show significant differences between their fast and slow instances (Figure 2.7).

However, in the present chapter, the specific signal changes around each instance of task performance differ from what has been observed for the flanker task. Groundbreaking work by Weissman et al. (Weissman, Roberts et al. 2006) demonstrated that fast performance on a visual letter-based task was associated with a prior reduction in the default mode network signal and increase in the task positive network signal. Eichele et al. followed the work of Weissman but used a standard arrow-based flanker task and focused on prediction of correct trials (Eichele, Debener et al. 2008). They demonstrated that these predictive changes in signal maintain their directionality up to 30 seconds prior to the performance of the task after correcting the BOLD signal for the hemodynamic response delay.

In the present chapter, when an overall median value was used to separate response times, the default mode network signal was significantly lower than the anti-correlated network's signal at 6s succeeding the task (neural electrical differences

76

expected 2s after task occurrence), following the peak of the hemodynamic response from motor regions (Miezin, Maccotta et al. 2000). When individual median values were used to separate response times, the default mode network signal was significantly greater than the task positive network signal from 4s to 8s prior to the task; therefore peak neural electrical differences would be expected 8s to 12s prior (Miezin, Maccotta et al. 2000). The first of these results was seen in the flanker task (Weissman, Roberts et al. 2006; Eichele, Debener et al. 2008) and supports fMRI activation seen for the PVT by Drummond et al. (Drummond, Bischoff-Grethe et al. 2005). The present chapter's second result, where the default mode signal is greater prior to the task, is in the opposite direction of Eichele et al. and Weissman et al. The opposite result may be due to the flanker task requiring greater cognitive control, and thus more sustained activation of the task positive network. Another possibility is suggested by data that drowsiness both reduces performance on the PVT (Jewett, Dijk et al. 1999; Graw, Krauchi et al. 2004) and was recently observed by Gular et al. (Gujar, Yoo et al. 2009) to reduce the amount of signal change in the default mode. If individuals exhibit a range of drowsiness the loss of default mode may become a factor at some point sufficiently prior to task performance. Thus, it is also possible that individual drowsiness is a much greater risk in the PVT than the flanker task. As drowsiness was not systematically tested in the present chapter the exact relationship is unknown.

Comparing the present chapter to another recent study of an attention task (Prado and Weissman 2011) also suggests that comparisons between attention tasks are possible. Prado et al. used a task where subjects were required to attend to either auditory (spoken letters) or visual (displayed letters) stimuli and ignore letters in the other modality, which

77

were either congruent or incongruent with the correct modality. They observed that greater connectivity between the precuneus (default mode) and dorsolateral prefrontal cortex (task positive) was linked to increased reaction time on the current trial but decreased reaction time on the succeeding trial. As Prado et al. calculated connectivity using psychophysiological interaction (Friston, Buechel et al. 1997) and a hemodynamic response function with a peak at approximately 6 to 8 seconds (Josephs, Turner et al. 1997) their results are most comparable to the current chapter's local difference in magnitude using linear regression at positive peristimulus times of 6s and 8s (see Figure 2.5c, peristimulus times of 6s and 8s). Even though the PVT is a less complicated task, the direction of the results (greater difference and greater anticorrelation are linked to faster performance) is identical.

2.5.6 A critical period for intra-individual task performance?

As the intra-individual relationship between reaction time and network activity was limited to four to eight seconds prior to task performance (indicating neural activity eight to twelve seconds prior) this suggests that intra-individual variation may influence studies where the time separation between trials falls within this window. This may have been seen in the present chapter. Using local difference in magnitude, two-group analysis did not show a significant relationship in inter-individual analysis within the four to eight seconds prior time span (Figure 2.5a). However, with the increase in statistical power using linear regression, this difference in intra-individual performance was now seen inter-individually (Figure 2.6c).

78

Why does this critical period for intra-individual performance exist? Its leftmost bound (-8s) may be determined by the fact that the neural mechanisms for task preparation may differ from those for task performance, as Prado et al. observed that effects detrimental for the current trial could enhance a future trial (Prado and Weissman 2011). Alternately it may be due to a lack of statistical power at long peristimulus times in the present chapter. Its rightmost bound (-4s) may be determined by task interference from resting state networks (Weissman, Roberts et al. 2006; Eichele, Debener et al. 2008). It is also possible that the time scale upon which spontaneous fluctuations affect behavior is slow enough so that from eight seconds prior to the neural response itself (about four seconds succeeding) it isn't possible to resolve its effects.

2.5.7 Stimulus detection vs. speed of response

Previous studies have shown a significant relationship between stimulus detection and signal within the default mode network and also within the dorsal attention system which contains many of the same brain regions as the task positive network such as the intraparietal sulcus and frontal eye field (compare Kelly, Uddin et al. 2005 to Sadaghiani, Hesselmann et al. 2009).

However in the present chapter, no significant difference was found prior to task performance between fast instances and slow instances using individual networks (Figure 2.9). It should be considered that, in the present chapter, there were not enough "miss" instances (instances of the PVT where individuals did not respond) to use in analysis (only 18 instances in the entire study were missed, these occurred in only 4 subjects).

Therefore, every result analyzed can be considered a "hit" in terms of stimulus detection. The evolution over time of the mean signal in the default mode and task positive networks (Figure 2.9a, c) appears bimodal, potentially similar to "hit" results seen by Sadaghiani et al. (Sadaghiani, Hesselmann et al. 2009) using auditory detection. However in future studies the protocol would need to be changed to result in more "miss" instances for a comparative analysis to be done.

2.5.8 Timescale of correlation versus response times on task

The median response time on the task was slightly less than one second (971ms), however, correlations were only calculated every 2s to reduce the potential for Type I errors (by reducing the number of hypotheses tested) and to ensure there was enough data for each point tested (even though fMRI was comparatively fast in this study, there was still only one image per 300ms). Therefore, it was assumed that the effect of response time (<1s resolution) on the measured changes in fMRI (>2s resolution) would be minimal.

The two-group analysis of the mean signal in each network didn't show any statistically significant difference between fast and slow performance groups, supporting this assumption. The peristimulus time plots of mean signal in each network are shown in Figure 2.9. For the mean signal in the task positive network, both fast and slow groups do appear to have peak signal after performance of the task at the same time. However, for the default mode network, the slow performance group appears to be lagged about four seconds after the fast performance group in terms of where the post-stimulus signal peaks

80

(Figure 2.9). This could be a statistical anomaly (which is likely, as there were no statistically significant differences in this figure), or it could be an indication of slow performers having a slower-acting default mode network. If true, it might support some long-standing suppositions about attention deficit disorders and network efficiency (Weissman, Roberts et al. 2006). This would be an interesting topic for future work, especially if more tasks can be included during fMRI recording.

2.5.9 Conclusion

The results presented here extend previous results regarding network anti-correlation to rapid performance on the PVT. In addition to results that are comparable to previous studies, the present chapter suggests that the time scale at which anti-correlation between the default mode and task positive networks predicts improved performance is very small, at least as short as a 12.3s window both inter- and intra-individually, and potentially this opposing relationship can be seen to predict performance on an intra-individual basis at a single time point if one network's normalized signal is subtracted from the other (Figure 2.6a). These results would allow researchers to use short windows to evaluate the current condition of functional networks without requiring long resting state functional imaging runs. More interestingly, these results suggest that correlation in short, sliding windows is a viable metric and appears to be reflecting the same behavioral variation as correlation calculated from entire resting state runs. This would imply that the neural basis of functional connectivity could be better understood by investigating dynamic, sliding-window correlation.

81

The present chapter also suggests that predictive metrics resulting from spontaneous oscillations may reflect a combination of both intra-individual and inter-individual variation in network properties. However most previous studies have only considered either inter-individual differences in spontaneous fluctuations or large scale inter-individual network differences in resting state networks. The simple method used in the present chapter to group instances by both intra-individual and inter-individual differences, as well as using similar metrics for both resting state data and instantaneous data, can be applied in future studies to better understand how both the individual's transient state and the individual themselves affect results.

The contribution of the global signal was simply regressed in this study (Murphy, Birn et al. 2009; Scholvinck, Maier et al. 2010), but for real-time performance prediction it remains an open problem. Results generated using network masks generated in 12.3s windows are a promising future direction, even if they are not expected to match results generated using more stable networks (Figure 2.2 and 2.10, see also Deco, Jirsa et al. 2011). However, the results presented here are, in general, promising for the future development of second-scale, real-time performance prediction using functional networks.

82

CHAPTER 3

NEURAL BASIS OF DYNAMIC RESTING STATE FMRI DEFINED BY INTERHEMISPHERIC SLIDING WINDOW CORRELATION

3.1 Introduction

As described in Chapter 1, dynamic changes in functional connectivity have been shown by calculating correlation coefficients in sliding windows between different brain regions. Chapter 2 illustrated that such changes are behaviorally relevant. However it is still unclear if these changes have a basis in the brain's underlying neural electrical activity.

In the present chapter, the electrical (neural or glial) basis of these dynamics are examined by re-analyzing simultaneously recorded electrophysiology and fMRI from the left and right primary somatosensory cortex (SI) of the anesthetized rat, data first reported by Pan et al. (Pan, Thompson et al. 2011). The author of this dissertation was a major contributor to Pan et al. (second author), and is the first author and primary contributor on the manuscript under review that results from the work presented in this chapter.

Previous work in the rodent identified left and right SI as one of the few pairs of areas where BOLD dynamics were significantly different from those of randomly-matched time courses (Keilholz, Magnuson et al. 2012). The contralateral homologous regions of the brain are the first regions where resting state functional connectivity was observed (Biswal, Yetkin et al. 1995) and studies since have continued to find them

among the strongest functionally connected regions (Cordes, Haughton et al. 2000; Calhoun, Adali et al. 2001). This is hypothesized to be due to strong interhemispheric connections in the underlying brain anatomy, notably the corpus callosum (Nielsen, Montplaisir et al. 1993).

Examining changes in BOLD correlation between specific interhemispheric sites allow us to examine a spatially localized "network," simplifying the comparison to electrophysiology because the signal from our electrodes will be localized due to our electrical recording methods. This will allow us to understand changes over time in BOLD to BOLD correlation in terms of how it relates to changes over time in electrophysiology to electrophysiology correlation. The BOLD to BOLD correlation that is seen in fMRI-only studies can thus be better understood.

By comparing sliding window functional connectivity for the BOLD signal and for band-limited power (BLP), a well-established neural correlate of spontaneous fMRI (Shmuel and Leopold 2008; Pan, Thompson et al. 2011; Magri, Schridde et al. 2012), this chapter shows that changes in the correlation of BLP between the left and right electrodes are linked to changes in BOLD correlation, particularly in the higher frequency ranges (25-100Hz) and the theta band (4-8Hz). The correlation between the two increases with the window length used, but longer window lengths increase inter-trial error more than accounted for by normalization, thus may be obscuring the very short dynamics themselves. These findings strongly support a neural origin for at least some portion of the time-varying fMRI connectivity observed in the brain.

3.2 Materials and Methods

3.2.1 Animal preparation

All experiments were performed in compliance with NIH guidelines and were approved by the Emory University Institutional Animal Care and Use Committee. The data analyzed were originally acquired for a previous study examining LFP and BOLD correlation for entire fMRI runs using standard analysis techniques, and a more detailed description of experimental procedures can be found in the resulting paper in Brain Connectivity (Pan, Thompson et al. 2011). Briefly, seven Sprague-Dawley rats (male, 200-300g) were implanted with high impedance (1-5 MΩ) glass microelectrodes in left and right primary somatosensory cortex. A demonstration of the preparation protocol is available in the Journal of Visualized Experiments (Pan, Thompson et al. 2010). Animals were maintained under anesthesia as they were transferred to the MRI cradle and fixed in the stereotaxic head holder.

3.2.2 Data acquisition

All imaging was performed on a 9.4 T horizontal bore small animal MRI system (Bruker, Germany). A three plane scout image was first acquired to position the fMRI images. To improve the homogeneity of the magnetic field, the volume of interest (6 mm^3) was shimmed using FASTMAP (Gruetter 1993). Manual shimming adjustment was applied when necessary to improve the field homogeneity of the selected slice. For fMRI recording, a coronal imaging slice was selected, which included interhemispheric forepaw primary somatosensory areas, in which the glass recording electrodes were

85

implanted. The EPI imaging parameters were FOV, 1.92 x 1.92 cm^2; matrix size, 64 x 64; in-plane resolution, 0.3 x 0.3 mm^2; slice thickness, 2 mm; TR/TE, 500/15 ms. Each fMRI scanning session included 1000 single-slice images acquired over 8.3 minutes. Twenty unsaved images were acquired prior to each scan to reduce transient signal intensity fluctuations. Resting state runs were collected under concentrations of isoflurane which ranged from 1% - 2%. Isoflurane levels used for specific scans are shown on Table 3.1. The isoflurane, in a mixture of O_2 and room air, was continuously delivered to the nosecone allowing for free breathing throughout the experiment. The rat's oxygen saturation, measured with a pulse oximeter, was kept above 98% throughout the data acquisition process. One to four simultaneous LFP and fMRI recordings were conducted for each animal. The specific number of scans for each rat is shown on Table 3.1. Thirteen runs were used total from seven rats. Runs were excluded if they showed head motion more than one voxel total (quantified using Statistical Parametric Mapping, SPM8), if abrupt spike-like head motion was observed, or if the entire run (1,000 images) could not be used, due to noise in electrophysiology data preventing removal of scanner artifacts (see below).

3.2.3 Electrophysiology preprocessing

In MATLAB (Mathworks, Natick, MA), artifacts in the raw LFP signal due to the fMRI scanning were removed using a method based on previously established EEG methods (Allen, Josephs et al. 2000) and described in detail elsewhere (Pan, Thompson et al. 2010; Pan, Thompson et al. 2011). To summarize, the saturated portion of the signal that occurs during EPI readout due to rapidly changing gradients (less than 22ms per

86

500ms) was removed and replaced with a linear function between the two connecting points on each side of the saturation. The non-saturated decaying oscillation that occurs as the amplifier recovers from saturation (approximately 150ms to decay, though the entire 500ms period was used for artifact removal) was removed by averaging across every fMRI run and subtracting the resulting artifact waveform from each to produce a de-noised LFP signal. See Figure 2 in Pan et al. (Pan, Thompson et al. 2011) for an example.

_____

Table 3.1: Isoflurane levels, number of runs used and date recorded from each rat.
* The first run from this rat is plotted in Figure 3.1 A and B.
** Anomalous breathing was noticed approximately halfway through the run and isoflurane was increased to 2% to follow the protocol.

Rat index	Date	Number of runs	Isoflurane levels (%)
1*	11/6/2009	2	1.5
2	11/7/2009	1	1.3
3	11/12/2009	1	1.5
		1	1.4
4	11/13/2009	1	1.8
5	11/14/2009	3	1.5
6	11/20/2009	1	1.5
		1	1.2-2.0**
7	11/21/2009	2	1.5
Total		**13**	**1.2-2.0**

3.2.4 Band-limited power calculation

From each LFP signal, six band-limited power (BLP) time courses were created; delta (1–4 Hz), theta (4–8 Hz), alpha (8–14 Hz), low-beta (14–25 Hz), high-beta (25–40 Hz), and gamma (40–100 Hz). The BLP time courses were created by taking the fast Fourier transform (FFT) of segments of the de-noised LFP signal. Each segment started at the current fMRI image and extended until prior to the start of the next fMRI image (0.5s segment, equivalent to one fMRI sample, for alpha and higher frequencies) or extended just prior to the start of the third succeeding fMRI image (2s segment, equivalent to four fMRI samples, for delta and theta). From the FFT of each segment, power values were taken within the frequency band of interest, and these power values had the mean taken in order to create a BLP signal at 2Hz. The resulting BLP signal represents power versus time in each frequency band.

BLP time series were then filtered using a finite impulse response (FIR) filter with a length of 100 seconds to between 0.01 and 0.1Hz, as this frequency range contains statistically significant coherence between BOLD and LFPs in rats anesthetized with isoflurane (Pan, Thompson et al. 2013). This also matches the range used in previous studies of functional connectivity in isoflurane-anesthetized rats (Liu, Zhu et al. 2010; Pan, Thompson et al. 2011).

3.2.5 fMRI preprocessing

Data analysis was conducted in MATLAB and SPM 8 (http://www.fil.ion.ucl.ac.uk/spm). To summarize, first a brain mask was created, and rows and columns outside the brain were removed from the image. Head motion was

88

corrected using SPM and any runs showing abrupt spikes of head motion or more than one voxel motion were excluded from further analysis. Images were spatially smoothed (Gaussian filter, 0.5 full-width-half-maximum). Linear de-trend was performed on each voxel, setting all voxels to zero mean.

3.2.6 Global signal regression

Some of the analysis described in this paper was performed with and without global signal regression, in case the correction affected the relationship between BOLD and the electrical activity. Analysis with global signal regression is the default choice due to its common use in similar studies (Majeed, Magnuson et al. 2009; Liu, Zhu et al. 2010; Pan, Thompson et al. 2011) and as it removes effects of slight anesthesia differences (Liu, Zhu et al. 2012). This was done by taking the mean BOLD signal at each time point from all voxels across the brain and regressing this signal from every voxel's individual BOLD signal. Whether global signal was removed or not, all voxels were then set to unit variance.

3.2.7 Region of interest selection and filtering

As electrodes were implanted only in left and right SI, only these regions were used for further analysis. For each rat, regions of interest (7 to 22 voxels, based on slight differences of the positioning of the slice and the quality of the shim) were manually drawn in left and right primary somatosensory cortex (SI) of the lower forelimb region using an atlas for reference (Paxinos and Watson 2005). The BOLD signal in each region

89

of interest was averaged across all voxels to produce left and right "SI BOLD signals."
These signals were filtered using an FIR filter that matched the filter used on BLP time
courses.

3.2.8 Normalization of correlation values

As Pearson correlation (r used to represent individual correlation values, ★ used
to represent the function of correlation) values are distributed only within [-1, 1], and as
correlation of series with fewer points are biased towards higher variance in resulting r
values, normalization was performed prior to averaging and prior to statistical tests. This
consisted of taking the Fisher transformation (hyperbolic arctangent) of the r values, then
dividing the result by one divided by the square root of the number of samples correlated,
minus three (the standard deviation of the sampling distribution). This normalization
would have created, for hypothetically independent and normally distributed signals, a
normal distribution of correlation values (z scores) with a mean of zero and a standard
deviation of one.

3.2.9 Sliding-window correlation

Sliding-window correlation was calculated using custom-written software in
MATLAB. It was defined as Pearson correlation, calculated for time windows that were
shorter than the entirety of the signals being correlated, incremented by one TR at a time
from the beginning of the signals to the end. Adjacent windows overlapped by their
length minus one sample. The maximum number of windows was equal to the total

90

number of images, minus the window length, plus one. The sliding-window correlation time course was then taken as the values resulting from these windows, in order.

For the present chapter, sliding window correlation was calculated between left and right SI for all BOLD and BLP signals. This was because the focus in this chapter is on understanding dynamic BOLD to BOLD correlations that have been observed previously (Chang and Glover 2010; Hutchison, Womelsdorf et al. 2012). The interhemispheric SI network provided a simplified model for examining this, and is a model where dynamic changes in BOLD versus BOLD correlation have been previously observed (Keilholz, Magnuson et al. 2012). For comparison to previous studies, Pearson correlation was also calculated over the entire run between the signals from left and right SI for BOLD and for every BLP band. The entire-run r values were converted to normalized z values, averaged, and then the inverse transformation was taken to find an estimated average r value for comparison to Pan et al. (Pan, Thompson et al. 2011).

Here, sliding window correlation between equivalent interhemispheric signals, versus time of the window start points, will be referred to as a "sliding window series," e.g. a BOLD sliding window series represents sliding window correlation between interhemispheric SI from BOLD.

3.2.10 BLP sliding window series ★ BOLD sliding window series

The sliding window series from interhemispheric BOLD was compared to each sliding window series from interhemispheric BLP by computing Pearson correlation between the two corresponding sliding window series for every run.

91

As it was expected that the BOLD sliding window series to lag the BLP sliding window series due to the hemodynamic delay, BOLD sliding window series were delayed four seconds relative to BLP sliding window series to match when peak correlation was observed in steady-state findings (Pan, Thompson et al. 2011). Preliminary work was done to see if a peak correlation based on time shift could be found for BLP sliding window series being correlated with BOLD sliding window series; however, due to the small sample size the standard error was too large to make inferences (allowing shifts up to ± 100s, standard error in optimal time shift rounded to $6s \pm 7.5s$ for theta, high beta and gamma, and $-5s \pm 9.5s$ for delta, alpha and low beta, mean $\pm$ standard error).

For most of the analysis performed (any analysis that did not measure the effects of varying window length), a window length of 50s was used. Correlation values were thus taken in every 50s segment of the signals, ordered by the start time of each window, to produce the sliding window series. 50s was selected to match previous work with fMRI-only data (Keilholz, Magnuson et al. 2012). (For further justification, see section 4.5.3.) All r values were normalized to z values and the mean z value was then taken across all rats, runs and time points for both BOLD and every BLP.

3.2.11 Dependence on window length

To investigate effects of window length on results, the calculation of sliding window series was repeated for window lengths from 10 to 100 seconds (the filter's pass-band) in 0.5 second increments. First, all r values were converted to normalized z values

92

and the mean z value was then taken across all rats, runs and time points for BOLD and every BLP signal as a function of window length. Second, for every fMRI run, window length and BLP band, Pearson correlation was calculated between every run's sliding window series from BOLD and that run's sliding window series from BLP, shifted 4s prior. Resulting *r* values were converted to normalized z values. Both of these tests were repeated without normalization on naïve *r* values.

3.2.12 Correlation with global signal

As regression of the global signal from every voxel in BOLD was found to increase correlation between BOLD sliding window series and BLP sliding window series (see section 3.3.4), it is possible that the global signal acts as a confounding factor to sliding window analysis. This is surprising as it contradicts previous studies that have indicated the global signal reflects underlying neural activity (Scholvinck, Maier et al. 2010). Therefore, a further investigation of the effects of the global signal was performed. The global signals (calculated from the mean fMRI signal from all brain voxels) were saved from every run during section 3.2.6. Prior to the analysis done in section 3.2.12, a linear de-trend was performed on these global signals, they were then set to unit variance and filtered to the same pass-band as the other signals analyzed in this study (0.01 to 0.1Hz, FIR filter with a length of 100s).

Standard Pearson correlation coefficients were calculated for each global signal versus either the corresponding BLP signal (six bands) or the corresponding SI BOLD signal. Correlation between the global signal and SI BOLD was calculated both with and

93

without global regression performed on the SI BOLD data. In every case where it was compared to a BOLD-derived signal (SI BOLD or the global signal), the BLP signal was lagged by four seconds. These coefficients (*r* values) were converted to normalized z values as was described in section 3.2.8. Data from both hemispheres were combined for statistical analysis.

In addition to direct relationships between measured neurophysiological signals and the global signal, it is also possible that increases/decreases in the global signal increase/decrease correlation across the entire brain. This is because the strong global signal could obscure local variations in correlation. In particular, it is possible that changes over time in the BLP sliding window series may be driven by the magnitude of the global signal if the global signal is driving network dynamics (Scholvinck, Maier et al. 2010). To investigate this, the sliding window series (interhemispheric correlation calculated in 50s sliding windows for the corresponding signal) for SI BOLD (with global regression) and for each BLP band was also correlated with the global signal using standard Pearson correlation. All correlations between sliding window series (from BOLD or BLP) and the global signal (from BOLD) were done at multiple alignments; these alignments corresponded to every possible alignment between a point in the global signal and where that point was located within the corresponding window   (-25s to 25s, relative to center of window). In addition, in every case where it was compared to a BLP-derived sliding window series, the global signal was moved backward in time by four seconds. These coefficients (*r* values) were converted to normalized z values as was described in section 3.2.8.

94

3.2.13 Sliding window correlation from infraslow LFP

The methods described in sections 3.2.3-3.2.10 were repeated, except that data were used from Chapter 4 (section 4.2.1) instead so that frequencies down to the DC component (0Hz) could be used from the data. As the low-frequency amplifiers potentially have trouble recording higher frequency activity during simultaneous fMRI-LFP experiments (personal communication with Wen-Ju Pan, 2013), only the infraslow component was examined from these data for this dissertation. From these data, both anesthesia were examined with and without global signal regression performed on the BOLD data. To produce the infraslow signal, artifact-removed LFP data were resampled to 2Hz, linearly de-trended and directly filtered with an FIR filter (hamming window, length 100s) to 0.01-0.1 Hz for isoflurane and 0.01-0.25Hz for dexmedetomidine, normalized to zero mean, unit variance and finally inverted to match the analysis of the DC component in Pan, et al. (Pan, Thompson et al. 2013). Sliding window correlation for BOLD and infraslow LFP were calculated using 50s sliding windows and the two sliding window series for each run were correlated with each other as is otherwise described in sections 3.2.3 to 3.2.10.

3.2.14 Determination of significance

To minimize the chance that correlation observed between the two sliding window series was due to inherent characteristics of the processed signal, artificial null distributions were created for comparison. The correlation between BOLD and BLP sliding window series' time courses for the artificial null distribution was calculated in the same manner as for the real data, but each BLP signal was paired with a BOLD signal

from a different fMRI run (from both the same rat, where available, and different rats). For correlation with the whole-brain (global) signal, the same process was done except the BLP, BOLD or sliding window series signals were paired with whole-brain signals from different fMRI runs. In each case, every trial was compared to every trial with an index number higher than its own index, to create a large null distribution from the upper triangular half of the comparisons matrix ($[13^2\text{-}13]/2 = 78$ total values). For each BLP band, a two sample, two-tailed, equal variance student's t test was calculated between the distribution of actual z scores and the null distribution of z scores (using a 50s window with a 4s delay for BOLD sliding window series versus BLP sliding window series). To correct against false positive errors due to multiple comparisons, sequential goodness of fit (SGoF) (Carvajal-Rodriguez, de Una-Alvarez et al. 2009), a binomial-based method of controlling family-wise error rate (FWER), was calculated to determine a threshold for significance with a 5% FWER. Each figure or table is considered one family for statistical purposes.

3.3 Results

3.3.1 Sliding-window correlation

Both BOLD and BLP correlation time courses calculated with a sliding window approach ("sliding window series") exhibited interesting variability in all rats. An example from one rat (first run, index = 1 from Table 3.1) is shown in Figure 3.1A. This rat is typical as its gamma and beta bands have mostly positive values. The changes in correlation over time are not limited to the BOLD signal but also can be observed in the

BLP signals, which implies that a neural origin is possible for the variation in connectivity measured with BOLD.

"Steady-state" correlation was calculated for each time course using data from the full run for BOLD and for each BLP band. The results are given in Table 3.2 as both actual mean z values and estimated *r* value averages that are in close agreement with previous analysis of this data presented in Figure 7 of Pan et al. (Pan, Thompson et al. 2011). Correlation between BLP from left and right SI is highest for beta and gamma bands and lowest for delta and theta bands.

Table 3.2: Mean interhemispheric correlation (normalized z values) between left and right SI signals for BOLD and each BLP signal from entire fMRI runs. Estimated Pearson correlation (*r*) values are also shown; these were created by applying the inverse transformation to the z values shown in the column to the left. Compare *r* values to Figure 7 of Pan, et al. (Pan, Thompson et al. 2011). Mean ± one standard error is shown for each signal. These are not from a window, but instead use the entire length of data to calculate correlation.

	Mean Interhemispheric Steady State Correlation	
	Normalized z	**Estimated r**
BOLD	8.5 ± 4.3	0.293 ± 0.151
Delta	9.0 ± 4.9	0.309 ± 0.174
Theta	7.4 ± 5.2	0.258 ± 0.182
Alpha	12.1 ± 7.1	0.406 ± 0.247
Low Beta	16.4 ± 4.4	0.525 ± 0.153
High Beta	16.5 ± 5.1	0.527 ± 0.179
Gamma	16.4 ± 5.2	0.525 ± 0.184

97

(A)

(B)
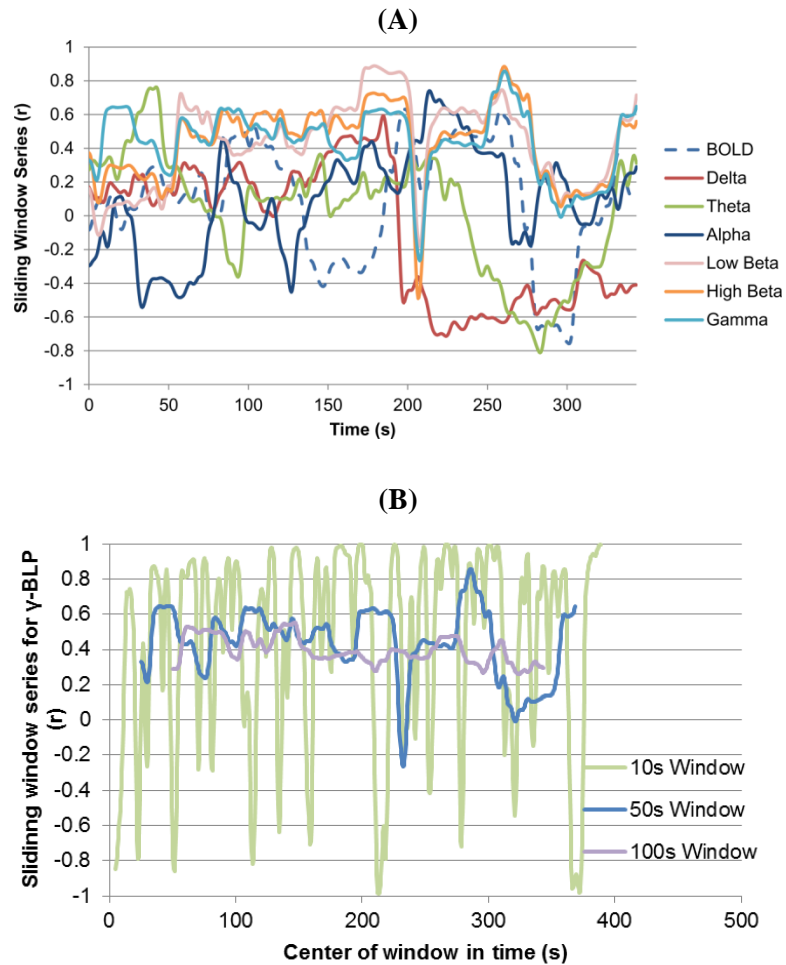
Figure 3.1: Example of interhemispheric correlation, measured in a sliding window as a function of window start time ("sliding window series") from one rat, one fMRI run. **(A)** Values are calculated using a window length of 50s, between left and right SI, for BOLD (dashed line) and each BLP band (solid lines, colors shown in legend), and are plotted versus the time of each window's start point. Correlation varies substantially over time for all signals, ranging from strongly positive to strongly negative for BOLD, delta, theta, and alpha. Beta and gamma band correlation is rarely negative in this example, yet still varies between zero and high positive values. See section 3.4.4 for an in-depth discussion of how some of the seemingly rapid changes and peaks arise. See Figure 3.10 for an example plot of the gamma BLP signal versus the sliding window series from gamma BLP.

(B) Comparison between three different window lengths for sliding window series generated from gamma BLP. Correlation in 10s windows is green, in 50s windows (same as part A) is blue and in 100s windows is pink. In this plot, the time axis represents the center of each window rather than the start point. Raw correlation values vary more in shorter windows, but overall trends are similar. For a similar plot, except for BOLD sliding window series instead of BLP, see Keilholz et al. (Keilholz, Magnuson et al. 2012), Figure 1.

3.3.2 BLP sliding window series ★ BOLD sliding window series

To examine the relationship between variations in BOLD correlation and in BLP correlation, the sliding window series from each BLP band was correlated with the BOLD sliding window series from the same fMRI run with BOLD lagging BLP by four seconds, to match Pan et al. (Pan, Thompson et al. 2011). 50s windows were used for this analysis. Note that four seconds may not be an exact match, as delta and theta used 2s power spectrum windows instead of 0.5s power spectrum windows for power calculations, causing each window in the BOLD sliding window series to potentially align with up to four windows in the delta and theta BLP sliding window series. As a control, correlation was also calculated by mismatching which BOLD sliding window series went with which BLP sliding window series, destroying common temporal information.

The results are shown in Figure 3.2. After SGoF correction for multiple comparisons, theta, high beta and gamma sliding window series were significantly correlated with the BOLD time courses (p=1.35×10^{-3}, 8.40×10^{-6} and 5.18×10^{-5} respectively). The strongest correlations were observed in the high beta and gamma frequencies. As the use of global signal regression has been debated (Gavrilescu, Shaw et al. 2002; Fox, Zhang et al. 2009), the same calculation was also performed without the use of global signal regression as a preprocessing step, and the pattern of correlation between BOLD and BLP time courses was similar. Correlation in all frequency bands was lower when global regression was not used, however results were similar. The decrease was greater in the statistically significant frequency bands (mean $\Delta z = 1.67$ for statistically significant bands, mean $\Delta z = 0.872$ for non-statistically significant bands).

99

Theta, high beta and gamma again passed correction for multiple comparisons when no global signal regression was used (p $= 7.20 \times 10^{-3}$, 1.35×10^{-3} and 1.81×10^{-3} respectively).

3.3.3 Dependence on window length

Correlation was also calculated between interhemispheric SI signals to create sliding window series using a large range of window lengths for both BOLD and BLP. Positive correlation was observed in all frequency bands even for the shortest windows, and the correlation increased with window length for the entire filter pass-band from 10s to 100s (Figure 3.3). This monotonic increase may partially be a bias due to the normalization that was performed to convert *r* values to z values. As described in section 3.2.8, normalization is based on the number of samples correlated. Therefore, longer windows will correlate more samples and thus normalization increases correlation values. An example of how the multiplicand for normalization changes is shown in Figure 3.4a, and it can be seen that it monotonically increases as well. Naïve correlation values also showed an increase in correlation with window length, however a plateau was reached at approximately 50s (Figure 3.4b).

Numerical values at window lengths of 10s, 50s and 100s are shown in Table 3.3 for comparison for both normalized and naïve correlation values. For normalized correlation values, at 50s every BLP band had reached only approximately 40% of the maximum value reached over all window lengths (Delta, 38%, Theta, 35%, Alpha, 36%, Low beta, 38%, High beta, 39%, Gamma, 39%) and BOLD had reached 67% of the maximum value over all window lengths. For naïve correlation values, at 50s every BLP

band had reached approximately 90% of the maximum value reached over all window lengths (Delta, 87%, Theta, 87%, Alpha, 90%, Low beta, 94%, High beta, 92%, Gamma, 92%) and BOLD had reached 91% of the maximum value over all window lengths.

Correlation was also calculated, for every window length and BLP band, between BOLD sliding window series and all BLP sliding window series, with BLP time shifted four seconds prior to BOLD. Results are shown in Figure 3.5, mean Z values for all bands are plotted versus window length in (A), standard error of Z values are plotted versus window length in (B). From 10s to 18s window lengths all bands show increasing correlation with increasing window length, and all bands also show positive mean correlation with window lengths within the entire pass-band. Delta and low beta first peak (first switch from increasing to decreasing) at relatively low lengths (18.5s and 29.5s window lengths respectively), high beta, gamma, and alpha peak later, in that order (67.5s, 68s and 71.5s window lengths respectively). Naïve correlation values, shown in Figure 3.6B, show an almost identical trend.

Figure 3.5B illustrates the corresponding standard error values, also plotted in Figure 3.5A as error bars. Error increases rapidly for all bands for the entire pass-band. This is seen even though normalization biased error towards lower values for longer window lengths, as shown in Figure 3.6A.
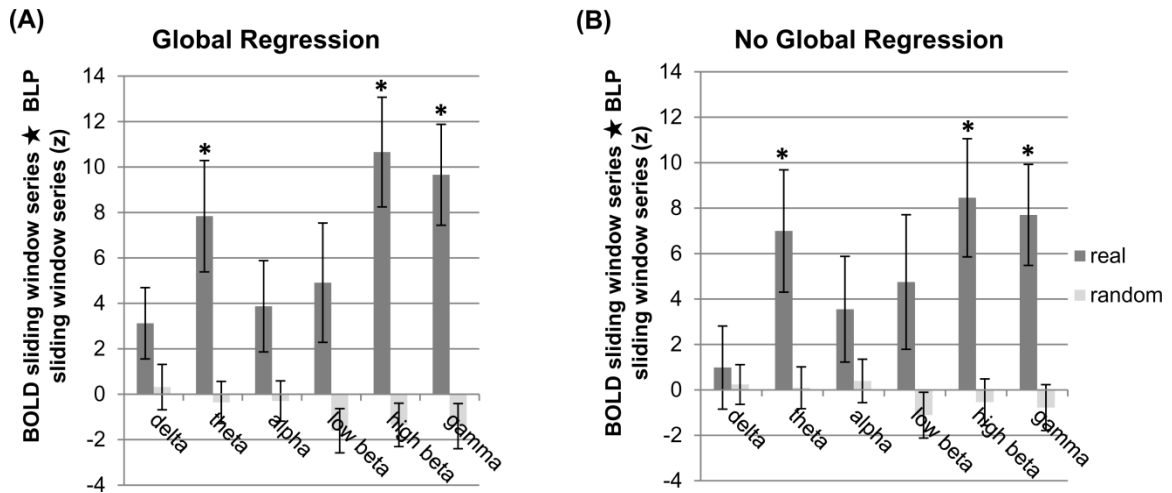
Figure 3.2: BOLD sliding window series versus LFP sliding window series. Sample time series are shown in Figure 3.1A with a detail in Figure 3.10. **(A)** Mean correlation (normalized z values) between BOLD sliding window series and BLP sliding window series for each frequency band, after global signal regression. Correlation between the BOLD sliding window series and the BLP time courses for signals from every incorrectly matched run are shown as a control. Error bars are one standard error. The highest correlation is observed in beta and gamma bands. Theta, high beta and gamma bands exhibited significant correlation to the BOLD sliding window series after correction for multiple comparisons, when compared to randomly matched BOLD and BLP pairs (t-test, p values: delta 0.272, theta 1.35×10^{-3}, alpha 7.65×10^{-2}, low beta 1.45×10^{-2}, high beta 8.40×10^{-6}, gamma 5.18×10^{-5}). **(B)** The same calculations were performed for data without global signal regression. All values are slightly lower, but the same three bands remain significance (t test, p values: delta 0.743, theta 7.20×10^{-3}, alpha 0.214, low beta 3.59×10^{-2}, high beta 1.35×10^{-3}, gamma 1.81×10^{-3}). Error bars are one standard error. This figure was calculated with a 50s long sliding window and with BLP lagged four seconds after BOLD.

* Statistically significant at 5% passing multiple comparisons correction (Carvajal-Rodriguez, de Una-Alvarez et al. 2009).

102
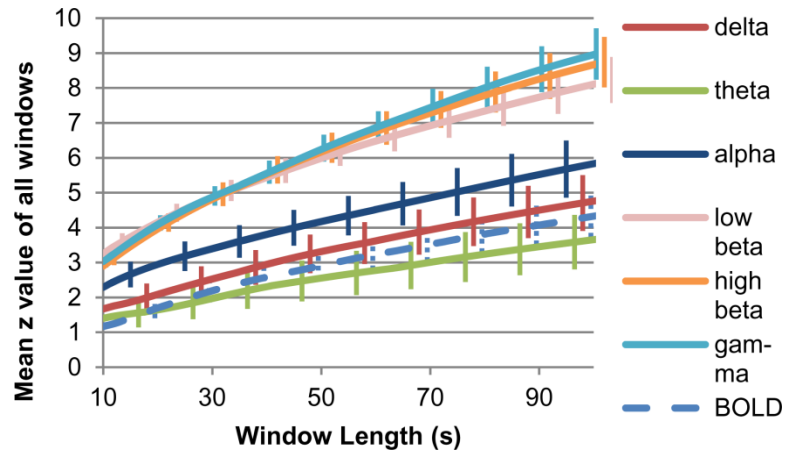
Figure 3.3: Window length dependence of interhemispheric correlation. Mean of normalized z values for interhemispheric SI correlation, over all windows and all runs, for BOLD and each BLP band, plotted versus window length. Error bars are one standard error in terms of inter-trial variance. For visibility purposes, only every 20th error bar is shown, and they are staggered between plots. As they were calculated from four second long segments, theta and delta include information from up to 1.5s longer than the window length used for correlation. Positive correlation is present for all bands even at the shortest windows, and increases steadily as window length increases. This plot uses normalized z scores, for naïve correlations see Figure 3.4.

_____
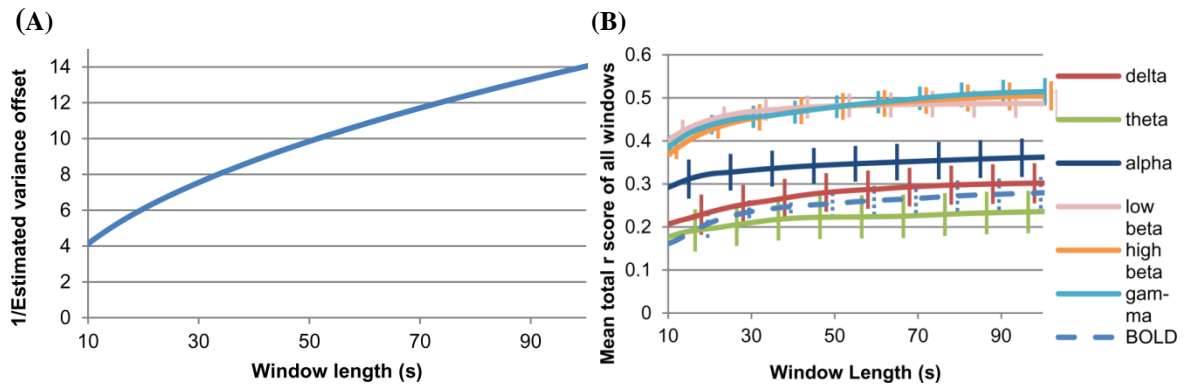
Figure 3.4: Interhemispheric SI correlation and normalization.
(A) The multiplicand (estimated variance offset) applied to z values to create a hypothetical N(0,1) distribution, versus window length. Used to normalize z values in Figure 3.3. As longer windows indicated more values to correlate together, the multiplicand tends to increase z values.
(B) Mean of naïve r values for interhemispheric SI correlation, over all windows and all runs, for BOLD and each BLP band, plotted versus window length. Error bars are one standard error. For visibility purposes only every 20th error bar is shown, and they are staggered between plots. As they were calculated from four second long segments, theta and delta include information from up to 1.5s longer than the window length used for correlation. Note that, unlike Figure 3.3, a plateau value appears to be reached by approximately 50s long windows.

103

Table 3.3: Mean correlations for interhemispheric SI sliding correlation for BOLD and every BLP frequency band. Results are shown for the shortest window length (10s), the window length used in most tests in this study (50 seconds), and the longest window length (100 seconds). Mean ± standard error is shown. The first three columns are normalized z values, the last three columns are naïve *r* values. As they were calculated from four second long segments, theta and delta may include information from up to 1.5s longer than the window length used for correlation. Note that normalized z values increase greatly with window length, but naïve *r* values plateau around the 50s window length. Also note that errors are comparatively small in most cases.

	10s	50s	100s	10s (naïve)	50s (naïve)	100s
BOLD	1.17 ± 0.06	2.91 ± 0.11	4.33 ± 0.17	0.16 ± 0.01	0.25 ± 0.01	0.28 ± 0.01
Delta	1.67 ± 0.10	3.31 ± 0.16	4.75 ± 0.22	0.21 ± 0.01	0.28 ± 0.01	0.30 ± 0.01
Theta	1.40 ± 0.10	2.55 ± 0.17	3.65 ± 0.22	0.18 ± 0.01	0.22 ± 0.01	0.24 ± 0.01
Alpha	2.29 ± 0.09	4.17 ± 0.15	5.83 ± 0.23	0.29 ± 0.01	0.34 ± 0.01	0.36 ± 0.01
Low beta	3.25 ± 0.07	5.98 ± 0.11	8.11 ± 0.18	0.40 ± 0.01	0.48 ± 0.01	0.49 ± 0.01
High beta	2.90 ± 0.06	6.16 ± 0.12	8.66 ± 0.20	0.37 ± 0.01	0.48 ± 0.01	0.50 ± 0.01
Gamma	3.03 ± 0.06	6.24 ± 0.11	8.95 ± 0.20	0.38 ± 0.01	0.48 ± 0.01	0.51 ± 0.01
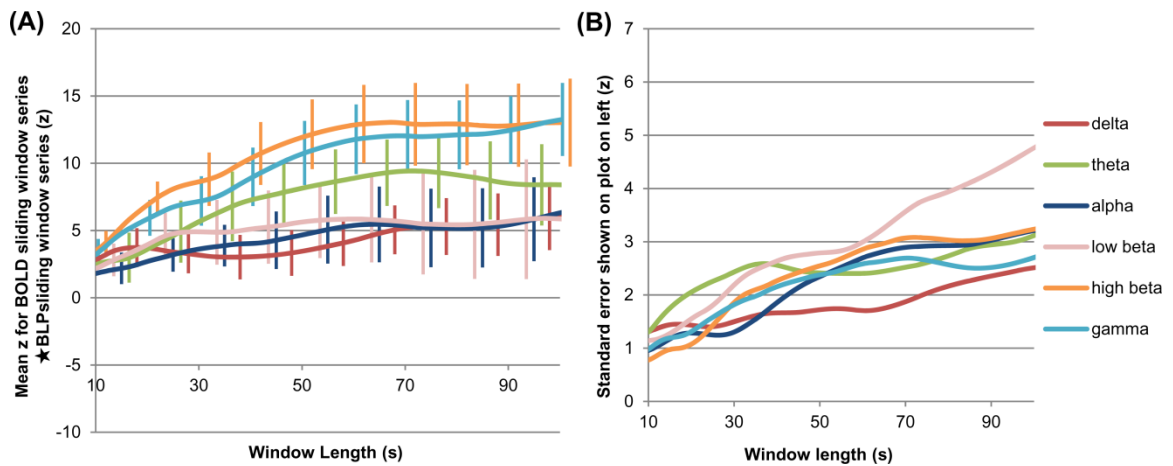
Figure 3.5: Window length dependence of BOLD vs. BLP. **(A)** Mean of normalized z values between BOLD sliding window series and each BLP sliding window series (shifted 4s prior), over all runs, plotted versus window length. Error bars are one standard error in terms of inter-trial variance. For visibility purposes, only every 20th error bar is shown, and they are staggered between plots. As they were calculated from four second long segments, theta and delta may include information from up to 1.5s longer than the window length used for correlation.
(B) Standard error of z values plotted in (A), these are the same values shown on the error bars. Note that correlation steadily increases until it reaches a plateau, but error steadily increases with window length. This plot uses normalized z scores, for naïve correlations, see Figure 3.6.

104
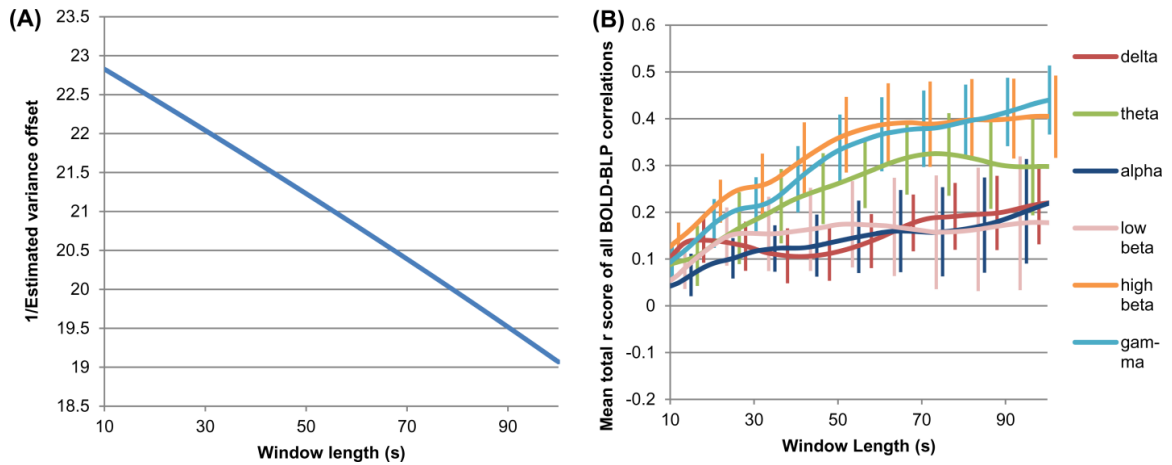
Figure 3.6: BOLD vs. BLP sliding window time course correlation and normalization.
(A) The multiplicand (estimated variance offset) applied to z values to create a hypothetical N(0,1) distribution, versus window length. Used to normalize z values in Figure 3.5. As window length increases, the maximum number of windows in the sample decreases. Therefore, the multiplicand for correlation between BOLD and BLP sliding window time courses will decrease normalized z values as window length increases, unlike the interhemispheric correlation values themselves, shown in Figure 3.4A.
(B) Mean of naïve *r* values for the BOLD sliding window time course correlated with each BLP sliding window time course, over all runs, plotted versus window length. Error bars are one standard error. For visibility purposes, only every 20th error bar is shown, and they are staggered between plots. As they were calculated from four second long segments, theta and delta include information from up to 1.5s longer than the window length used for correlation. Note that this figure closes matches normalized values in Figure 3.5A.

105

3.3.4 Correlation with global signal

Standard Pearson correlation was calculated between each SI BOLD and BLP signal (six frequency bands) and the corresponding global signal. Significance was tested by comparing versus data where the global signals had been mismatched (see section 3.2.14). These results are shown in Figure 3.7; strong significant correlation was shown between the SI BOLD signal (without the global signal regressed) and the global signal itself, weaker significant correlation was shown between theta and higher frequency BLP bands and the global signal. This result matched previous observations of correlations between electrophysiology and global BOLD (Scholvinck, Maier et al. 2010).

Standard Pearson correlation was also calculated between sliding window series calculated from 50s windows and the global signal. This was done for multiple alignments between the sliding window series and the global signal, ranging from each point in the sliding window series aligned to the equivalent of the start of its window in the global signal to the equivalent of the end of its window in the global signal. Significance was tested by comparing versus data where the global signals had been mismatched (see section 3.2.14). When BOLD with the global signal regressed or BLP signals were used to calculate the sliding window series, there was no statistically significant relationship between the sliding window series and the global signal (no p values less than 0.05 with or without correction for multiple comparisons, see Figure 3.8 for a histogram of p values).

106

(A)

(B)
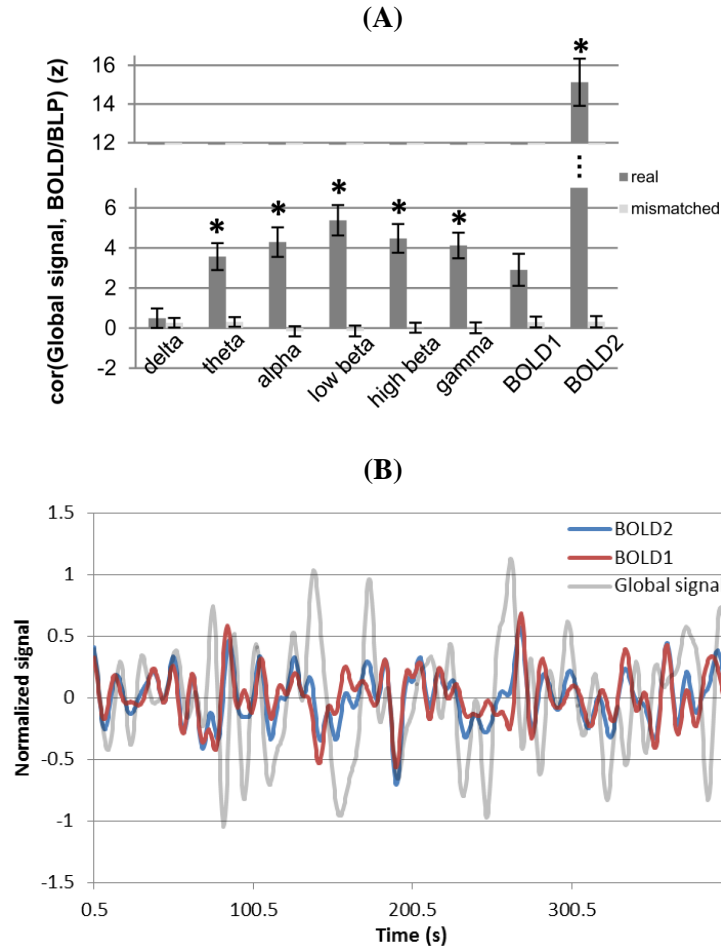
Figure 3.7: BLP and BOLD versus global signal. **(A)** Mean correlation (normalized z values) between BOLD from the SI regions of interest (BOLD1 has had the global signal regressed, BOLD2 has not) or BLP versus the filtered whole-brain (global) signal. Actual data are shown in dark gray bars, incorrectly matched data are shown in light gray bars. Error bars are one standard error. BOLD2 (no regression) and every BLP band except delta were significantly different than incorrectly matched BLP/BOLD and whole-brain signals (t test, p values: delta 7.17×10^{-1}, theta 1.31×10^{-6}, alpha 6.56×10^{-10}, low beta 2.14×10^{-12}, high beta 3.75×10^{-10}, gamma 2.52×10^{-8}, BOLD1 4.88×10^{-4}, BOLD2 2.71×10^{-40}, SGoF threshold $p \leq 1.31 \times 10^{-6}$).

* Statistically significant at 5% passing multiple comparisons correction (Carvajal-Rodriguez, de Una-Alvarez et al. 2009).

(B) Global signal over time, plotted against BOLD both with (BOLD1) and without (BOLD2) global signal regression, shown for rat 1, scan 1, left hemisphere. Note that both BOLD plots are similar to global signal, but BOLD2's values are generally closer. For plots of BOLD versus electrophysiology over time, see Pan et al. (Pan, Thompson et al. 2011), Figure 6.

107
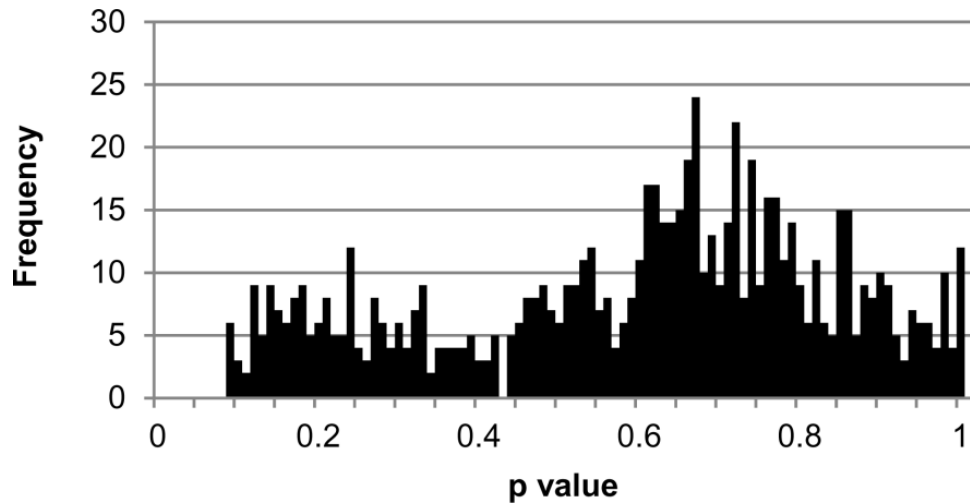
Figure 3.8: Sliding window series versus global signal. Sliding window time courses for all BLP bands and (global-signal regressed) SI BOLD were correlated with their respective whole-brain (global) signals. 50s windows were used, and BLP signals were lagged by 4s. This was done at all possible alignments between the whole-brain signals and the sliding window time courses, from the first sample in the window aligned to the corresponding sample in the whole-brain signal to the last sample in the window aligned to the corresponding sample in the whole-brain signal. This was repeated for each BLP band and BOLD, and each alignment using every possible incorrect pairing of whole-brain signals and sliding window time courses. Actual values were compared with incorrectly paired values using a two-sample, equal variance t-test to get p values.

P values are shown as a histogram of number of occurrences in the range [0,1]. Bins are 0.01 wide. No p values fall below the standard significance cutoff of 0.05. This result for sliding window time courses is in contrast to direct comparison of BLP and BOLD signals, shown in Figure 3.7, most of which showed a significant relationship with the whole-brain signal.

108

3.3.5 Sliding window correlation from infraslow LFP

To examine the relationship between variations in BOLD correlation and in infraslow LFP correlation, data from Chapter 4 were used. The sliding window series from infraslow (0.01-0.1Hz for isoflurane, 0.01-0.25Hz for dexmedetomidine) was correlated with the BOLD sliding window series from the same fMRI run with BOLD lagging BLP by four seconds, to match Pan et al. (Pan, Thompson et al. 2011). 50s windows were used for this analysis. As a control, correlation was also calculated by mismatching which BOLD sliding window series went with which BLP sliding window series, destroying common temporal information.

This result is shown in Figure 3.9. Out of four possible combinations (isoflurane and dexmedetomidine anesthetics, with and without global signal regression for BOLD data), only the combination of isoflurane and no global signal regression was marginally significant ($p=4.25 \times 10^{-2}$, all other results $p>0.05$). This was the only statistically significant result whether SGoF correction for multiple comparisons was performed or not.
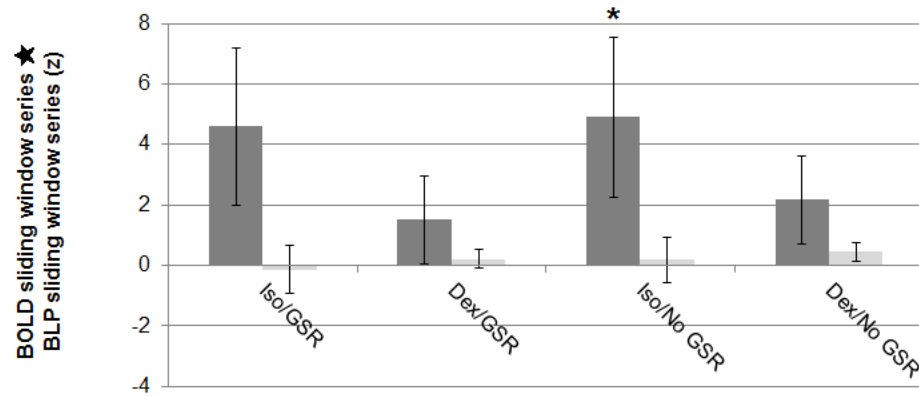
Figure 3.9: Infraslow signal sliding window correlation. The analysis from figure 3.2 was repeated, except that data from Chapter 4 were used. The LFP signals were preprocessed and filtered to 0.01 to 0.1Hz for isoflurane ("Iso") data and 0.01 to 0.25Hz for dexmedetomidine ("Dex") data. This was done both with ("GSR") and without ("No GSR") global signal regression. Compared to random pairings, only isoflurane with no global signal regression is statistically significant whether SGoF correction is used or not (Iso/GSR $p=5.67 \times 10^{-2}$, Dex/GSR $p=3.44 \times 10^{-1}$, Iso/No GSR $p=4.25 \times 10^{-2}$, Dex/No GSR $p=2.19 \times 10^{-1}$).

* Statistically significant at 5% passing multiple comparisons correction (Carvajal-Rodriguez, de Una-Alvarez et al. 2009).

_____

3.4 Discussion

This study provides the first evidence that the time-varying connectivity observed with resting state MRI (Chang and Glover 2010; Hutchison, Womelsdorf et al. 2012; Keilholz, Magnuson et al. 2012) reflects changes in correlation of electrical field potentials observed from an electrode implanted into the brain. The gamma, high beta and theta bands show a significant relationship between changes in LFP power correlation and changes in BOLD correlation (Figure 3.2). The finding of a neural basis for at least some of the variability in BOLD correlation is important, as previous studies demonstrated that similar variations could arise from randomly-matched or modeled time courses (Handwerker, Roopchansingh et al. 2012; Keilholz, Magnuson et al. 2012).

110

These findings also agree with data showing that variations in network connectivity on short time scales can predict task performance such as vigilance (Thompson, Magnuson et al. 2012) and diseases such as schizophrenia (Sakoglu, Pearlson et al. 2010).

3.4.1 Comparison to previous analysis

The analysis performed in this study utilized data acquired in order to compare steady-state functional connectivity to coherent neural activity as a function of anesthesia level (Pan, Thompson et al. 2011). Pan et al. observed high frequency BLP was most correlated across hemispheres and also contributed the most to the local BOLD signal, although all frequency bands were strongly correlated with BOLD at a lag time of 4s. However, only delta and theta correlation were predictive of BOLD correlation as the level of anesthesia varied, in agreement with the previous study by Liu et al. (Liu, Zhu et al. 2010). Anesthetic depth was not investigated in the present chapter, as data were pooled to provide greater statistical power. As the variation between frequency bands was clear regardless of variation in anesthetic levels (Figure 7 in Pan, et al. (Pan, Thompson et al. 2011)) the slight differences in anesthetic levels should not invalidate the present chapter.

The link between correlation in the delta and theta bands and BOLD, observed in the study by Pan et al., may have been caused by effects of anesthesia depth other than the overall reduction in neural correlation. The mechanism of neural suppression in isoflurane is likely inhibition of thalamocortical GABA and glutamate receptors (Alkire, Haier et al. 2000), while the mechanism of vascular dilation may be separate and due to

111

blockage of adenoside-triphosphate sensitive potassium channels (Cason, Shubayev et al. 1994). Both of these effects would increase with anesthetic depth. The present chapter showed a significant BOLD-BLP relationship for high beta and gamma bands, but not for delta, and theta remained significant (Figure 3.2). This may indicate that differing levels of neural suppression are behind the relationship between delta and BOLD seen in Pan, Thompson et al. 2011, Figure 9, rather than an implied delta-BOLD coordination.

3.4.2 Comparison to other animal and human studies

In the present chapter, the higher frequency BLPs were most closely related to BOLD changes. The comparatively high correlation values in these frequency bands are in close agreement with results linking BOLD fluctuations to LFPs recorded from a single site in nonhuman primates under different anesthetics (Shmuel and Leopold 2008; Magri, Schridde et al. 2012). This suggests the present chapter's results are not restricted to isoflurane and supports the idea that at least some of the BOLD fluctuations reflect variations in local activity linked to high frequency LFPs. The only other band that was statistically significant was theta (Figure 3.2). This is interesting as theta's phase may be coupled to amplitudes of higher frequency activity such as gamma (Canolty and Knight 2010; Tort, Komorowski et al. 2010) which also may be coupled to amplitudes of infraslow oscillations (0.01 to 1Hz) measured with EEG (Monto, Palva et al. 2008). The present chapter measured infraslow BOLD fluctuations, which are standard in functional connectivity, but did not use electrical amplifiers that could record LFP in this range. However, the infraslow LFP may also contain interesting dynamic correlations; Pan et al. recently showed that the BOLD signal is tightly coupled to very slow electrical

112

oscillations (<1 Hz) (Pan, Thompson et al. 2013). It is widely hypothesized in neuroscience that low frequency electrical activity organizes coordinates large areas of the brain, while high frequency activity coordinates local interactions. If this is true, the spontaneous BOLD fluctuations may reflect a combination of large scale patterns of quasi-periodic (displaying periodicity, but irregularly) modulation of excitability and localized fluctuations linked to local processing. It may then be possible to separate the large scale, quasi-periodic patterns from more variable changes in local activity (Majeed, Magnuson et al. 2009; Majeed, Magnuson et al. 2011), extracting new information about the neural organization of the brain. The sliding window approach used in this study may be weighted toward these local variations. Future work including the very low frequencies will help to elucidate the sources of the variation.

In humans, Chang et al. found a relationship between alpha power in the EEG and connectivity between two networks, the default mode and dorsal attention networks (Chang, Liu et al. 2013). Tagliazucchi et al. observed that increased power in the alpha and beta bands was associated with decreases in functional connectivity, while increased gamma power was linked to increased functional connectivity (Tagliazucchi, von Wegner et al. 2012). It should also be noted that while the studies by Chang et al. and Tagliazucchi et al. examined the relationship between connectivity and EEG power, this chapter focused on the correlation between BLP from areas in the left and right hemispheres as compared to the correlation between the BOLD signals from the same areas. (This focus was chosen as it allowed comparison to previous work which examined changes in BOLD versus BOLD correlation over time (Chang and Glover 2010; Hutchison, Womelsdorf et al. 2012; Keilholz, Magnuson et al. 2012), and also because

113

the hypothesis was that changes in the underlying electrophysiology drove changes in BOLD, rather than a dynamic BOLD-electrophysiology relationship. Nevertheless, future work could examine how BOLD versus BLP correlation may vary over time.) The frequency distribution of EEG power is related to the level of the subject's alertness, and therefore it is possible that the relationship between alpha power, for example, and BOLD is a result of fluctuations in the subject's drowsiness level. This is supported by the study by Tagliazucchi et al, which found that the relationship between EEG power and BOLD was altered in subjects with changing levels of alertness. Because the rats in this chapter were anesthetized and electrical signals were obtained using intracortical recordings that provide better spatial localization, these findings strengthen the evidence that the changes in correlation seen in human studies are linked to changes in neural coordination.

3.4.3 Window length dependence

BOLD and all BLP exhibited lower interhemispheric correlation when shorter windows were used. This may have been partially due to the normalization of z scores favoring longer window lengths which correlated more values (Figure 3.4A), because naïve correlation values also increased, but reached a plateau around 50s (Figure 3.4B). Based on Sakoğlu et al. (Sakoglu, Pearlson et al. 2010), a minimally sufficient window length can be selected as 0.5 divided by the minimum frequency in the signal. In the present chapter it was 0.5 / 0.01Hz = 50 seconds. In addition, a recent report by Allen et al., found that window lengths between 30 and 120 s had little impact on the resulting dynamics (Allen, Damaraju et al. 2012). In the present chapter, however, a 50s window

114

length was able to capture only 67% of maximum BOLD interhemispheric correlation when normalized to z values, but this increased to 91% when naïve r values were used. This suggests that longer window length provides greater confidence in results (represented by normalization increasing values more), even if raw r values do not increase greatly after the minimum suggested by Sakoğlu et al.

The results from correlating BOLD and BLP sliding window series (Figure 3.5) suggest that choice of window length may reflect a trade-off between shorter window lengths, which produce lower correlation but lower error, and longer window lengths, which increase correlation as they increase error. Note that this increase in error occurred in opposition to normalization which decreased z scores and thus was more likely to decrease error as window length increased (Figure 3.6). This result suggests that shorter windows may, in fact, reflect transient neural events which are synchronized between BOLD and electrophysiology. These result in inter-trial low error but, due to their transient nature, have low signal to noise ratio and thus low correlation. However longer windows may reflect a general BOLD-BLP relationship that can have very high correlation due to averaging over long periods, but may be occluded by transient events in some runs, leading to high inter-trial error. Figure 3.1B illustrates the difference in time courses for three different window lengths (10s, 50s, 100s), showing there are much larger changes in correlation in shorter windows if no normalization is performed. Figure 3.6B illustrates that the BOLD-electrophysiology relationship is weaker for the 10s windows, indicating that not all of these large fluctuations in BOLD reflect those in electrophysiology. Conversely, mean BOLD-electrophysiology correlation plateaus around 50s while error continues to increase. This can be seen in Figure 3.1B as well,

115

because the sliding window series from 100s windows looks similar to the series from 50s windows, but has fewer changes over time and thus is less responsive. The sliding window series from 100s windows is likely less responsive to both changes in the underlying neural physiology (that likely do correlate between BOLD and electrophysiology) and to changes that are due to noise (that likely do not). Thus, the individual sliding window series plotted in Figure 1B show why error increases in the longer window lengths as well.

Combining these factors, a smaller window length is advantageous due to its ability to more accurately represent transient events that may be merged over longer windows, and due to a lower inter-trial variability when BOLD is compared to electrophysiology. A longer window length increases the signal to noise ratio and provides more confidence in correlation results, and thus can be used in situations where differences between groups are more subtle. This confirms what has been seen in previous studies, as the shortest window length permitted by the filter's pass-band was effective in diagnosing network differences a few seconds before a task was performed (Thompson, Magnuson et al. 2012), while a window length slightly longer than the filter's pass-band was effective in diagnosing schizophrenia over entire resting-state scans (Sakoglu, Pearlson et al. 2010).

3.4.4 How rapid changes in correlation can occur

When a person is examining sliding window series, such as the one shown in Figure 3.1A, they might wonder how changes occur on a much more rapid time scale

116

than the length of the window. For example, Figure 3.1A shows a large downward spike at 233s in several frequency bands. However, all lines on this figure were calculated with 50s windows. This spike, which occurs on the order of 13s seems unusually fast as its values change rapidly during only 26% of one window's length. How then, can this occur?

Correlation values can be converted to percentage of shared variance by squaring. Therefore, as most of the changes in correlation in Figure 3.1A occur in the range from r = 0.0 to r = 0.6, this would indicate changes from 0% to 36%, 36% of the window (50s) being 18 seconds. And, indeed, in Figure 3.1A most changes do occur on a scale of approximately 18 seconds or greater. However there are some changes that occur more rapidly.

For the more rapid changes, we must consider how Pearson correlation is calculated. It is based on the dot product of both signals, and thus areas of the signal with greater (positive or negative) amplitude will have a greater effect on the resulting correlation value. However, it is also divided by the variance of both signals. This form of sliding window correlation is also insensitive to anything outside of the current window. Therefore, what is a tiny fluctuation in one window may become a gigantic spike in the next window if a large peak is present in the first window but absent in the second. Because of this, the percentage change for a 0.5s step of a 50s window may exceed 1% greatly, because the baseline to which the correlation values are normalized has been changed greatly.

117

Consider a 50.5s epoch of data with a spike at 0s and comparatively low baseline fluctuations at 0.5s to 50.5s. Consider two sliding window series time points on these data, one calculated from correlation from 0s to 50s, the other calculated from correlation from 0.5s to 50.5s. Let's first assume that the peak and the baseline are the same height. In the first point in the sliding window series, during the calculation of the Pearson correlation, the variance that each signal is divided by is 1% determined by the first peak and 99% determined by the baseline data. The second point is 0% determined by the first peak and 100% determined by the baseline data. Now let's assume that the peak is 10 times higher than the other data. Now, it now determines ~50% ($10^2 / [10^2 + 99*(1^2)]$) of the divisor for Pearson correlation in the first point, but still 0% in the second point, and thus can create a much greater than 1% change in correlation, even though only 1% of the window changes. In fact, as the peak's height approaches infinity relative to the baseline, the percentage change possible approaches 100% for an infinitesimally small step.

This can be seen in Figure 3.10, which provides a detail of Figure 3.1A from 183s to 283s. Examining Figure 3.1A, the most visually apparent change in a sliding window series appears to be from r ≈ 0.85 to r ≈ -0.18 in 13 seconds in low beta, pivoting around 233s. Correlation of 0.85 represents 73% shared variance and correlation of -0.18 represents -3% shared variance; this would seem an unusually large change as only 26% of the window changes over 13s. However the reason for can become clear if we compare it to the original signal. There is a large spike in both original signals, and this spike is correlated between hemispheres at 202s. However the spike is gone and loses its correlation at 206s. 206 + 25 = 231s, which is where correlation drops rapidly. However

at 259s, two large spikes begin to emerge again, and at $259 - 25 = 234$s the correlation increases rapidly again.

One possible solution to this problem would be to use a different shaped (e.g. Gaussian) window, rather than a square window. A square window was only used in this chapter as most previous work (Chang and Glover 2010; Hutchison, Womelsdorf et al. 2012; Keilholz, Magnuson et al. 2012) had used square windows. However, merely changing the window's shape may not be ideal. A differently shaped window could be sensitive to other unusual shapes in the data for the same reason; it would still re-calculate variance within the window if Pearson correlation is used. A better solution for future work could be to re-formulate the Pearson correlation equation to calculate the dot product within the window, but perform the variance-based normalization using the entirety of both signals. This modification may prevent sudden jumps in the sliding window series, and make them qualitatively easier to understand.

119
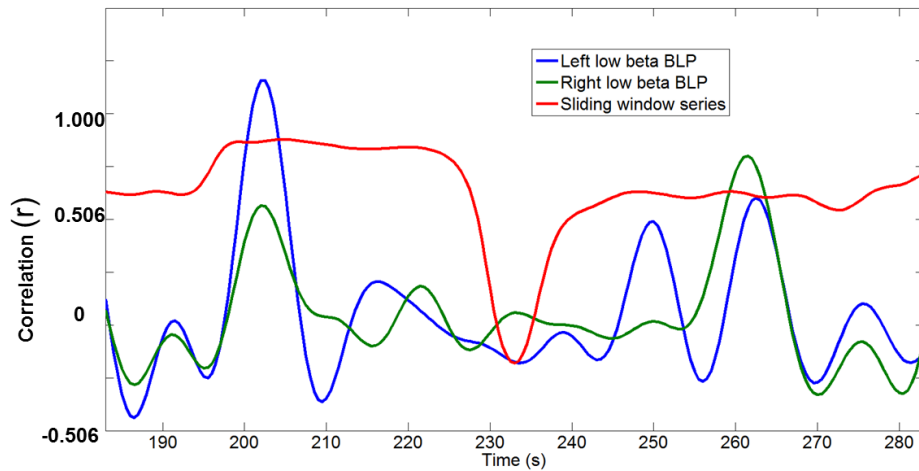
Figure 3.10: How comparatively rapid changes can occur in sliding window series. This figure illustrates a detail of Figure 3.1A, the sliding window series calculated with a 50s window length for BLP in the low beta band (red line), from 183s to 283s. Superimposed upon it are the interhemispheric original BLP signals (normalized to the same variance as the sliding window series, for visibility). The correlation values in the sliding window series are located in time to the center of their window; therefore each correlation point includes data from 25s prior and 25s succeeding its corresponding point on the x axis. A rapid change in correlation occurs both when a spike in the BLP falls outside the window (at 206s, thus affecting windows starting at 206 + 25 = 231s), but reverts when a new spike appears inside the window at 259s (259 – 25 = 234s).This is due to the normalization that Pearson correlation performs being sensitive to amplitude inside the window, but insensitive to amplitudes outside.

_____

3.4.5 Effects of global signal regression

Global signal regression increased the correlation between BOLD and BLP signals, but the overall pattern was preserved, including which bands showed statistical significance (Figure 3.2). The effect of global signal regression appeared to be primarily to increase correlation; this was probably because the global signal itself is slightly correlated with all signals (Figure 3.7) yet does not correlate with any sliding window series from BOLD or BLP (Figure 3.8), so its regression allows the parts of the signal that result in higher sliding window correlation to become more prominent. Scholvinck et al. reported that global signal was significantly correlated with gamma activity recorded

120

from a single electrode (Scholvinck, Maier et al. 2010). In the present chapter, gamma and beta BLP showed the greatest relationship with the global signal (Figure 3.7). The finding that the global BOLD signal is linked to BLP time courses but not to sliding window series (that were calculated by correlating the BLP) supports the hypothesis of both large-scale modulations and variable local contributions to the BOLD signal that may be separated with signal processing techniques to enhance the information obtained from brain imaging studies.

3.4.6 Limitations and future directions

Because anesthesia has a profound impact on both neural activity and the vasculature, it is important that these studies be extended to other anesthetic agents and, if possible, to awake rodents. However, it is likely that the findings will be similar, as in awake nonhuman primates the fMRI signal was also most strongly related to beta and gamma field potentials (Goense and Logothetis 2008) and exhibits correlation structures similar to BOLD in human pre-surgical patients (He, Snyder et al. 2008).

Large errors were measured when attempting to determine the time shift of maximum correlation between BOLD and BLP sliding window series. Therefore, this study simply used the four second shift that was observed in previous, steady-state results (Pan, Thompson et al. 2011, Figure 5). However, future work should investigate whether a "hemodynamic response function" truly exists when considering dynamic instead of steady state correlations.

121

Future studies should also examine other pairs of areas. Previous work has shown that the variability in BOLD correlation observed with sliding window techniques for left and right SI is quite different from the variability observed in randomly matched signals (Keilholz, Magnuson et al. 2012). However, other pairs of areas (SI and motor cortex) also exhibit some differences from the random distribution, and even areas where the distribution is statistically similar to randomly-matched data may actually contain information about neural activity. Simultaneous imaging and recording provides one way to link variability in the BOLD signal to an external measure of neural activity and verify that variability does not arise solely from inherent properties of the filtered, processed signal.

While this work has reduced the time scale of functional connectivity measurements, it is important to remember that the time scale of individual neurons firing is several orders of magnitude smaller, and what we measured with the LFP was the coordination of many neurons and potentially glial effects as well. In addition, we compared power in the LFP signal to amplitude in the fMRI signal, further reducing the time scale of the electrical activity we measured. Despite these limitations, there has been much work linking power changes in these frequency bands to the underlying neural and glial activity (see introduction of Magri, Schridde et al. 2012 for a brief review and application to fMRI), thus the present work is useful in establishing the neural and glial basis of dynamics in the resting state fMRI signal.

The finding that BLP exhibits variability in interhemispheric correlation that is closely linked to changes in BOLD correlation provides a firm basis for future explorations of network dynamics in the brain. For example, the prevalence and pattern

of brain states can be examined, as has been done in several fMRI studies (Allen, Damaraju et al. 2012; Keilholz, Magnuson et al. 2012; Liu and Duyn 2013). Utilizing simultaneously acquired BLPs as an independent measure of neural activity can help in identifying whether rare, transient states have a neural basis.

3.4.7 Conclusions

As interest in dynamic changes in the fMRI signal increases, it becomes important to understand the neural-electrical dynamics that underlie the fMRI dynamics. While studies differentiating based on behavior or disease can suggest that fMRI dynamics are important, and EEG studies can suggest a neural basis, studies such as the one presented in this chapter are required to better understand this basis. This study showed that interhemispheric BOLD sliding window correlation in the anesthetized rat was significantly related to sliding window correlation calculated for simultaneously-recorded BLP, particularly for the theta, beta and gamma frequencies. The strongest relationship between the BOLD signal and all BLP signals occurs when the sliding window series from BOLD was lagged after the sliding window series from the BLP by approximately 4 seconds; this closely matches what is seen for the signals themselves, without considering interhemispheric correlation (Pan, Thompson et al. 2011).

This chapter only examined a small part of one functional network: the interhemispheric primary somatosensory cortex, which is part of a larger somatomotor network (Majeed, Magnuson et al. 2009; Williams, Magnuson et al. 2010). However, this type of basic interhemispheric functional connectivity was the first type of functional

123

connectivity observed in fMRI (Biswal, Yetkin et al. 1995), and has been since observed as one of the strongest components of functional networks in humans (Cordes, Haughton et al. 2000; Calhoun, Adali et al. 2001). Therefore, the relationship between interhemispheric SI's dynamics and the underlying neural activity suggests that these results may translate to many other functional networks, including those observed in human subjects. Thus, for the sake of future researchers, it is heartening to know that data show that at least part of the variability in the BOLD sliding window series is related to changes in neural activity.

124

CHAPTER 4

NEURAL BASIS OF DYNAMIC RESTING STATE FMRI DEFINED BY QUASI-PERIODIC PATTERNS

4.1 Introduction

While much work has been done comparing resting state fMRI to neuropsychiatric diseases and behavioral variation in healthy individuals (as described in Chapter 1 and expanded to dynamic changes by the work in Chapter 2) most of the results are presented as specific to the disease or task, and few frameworks have emerged to help us understand the underlying physiological basis of these fluctuations (Sadaghiani, Hesselmann et al. 2010; Deco, Jirsa et al. 2011). An interesting possibility for such a framework was found by Majeed et al. (Majeed, Magnuson et al. 2009; Majeed, Magnuson et al. 2011) who observed highly reproducible spatiotemporal dynamic patterns in the resting state fMRI signal in rats and humans. These patterns are referred to as quasi-periodic, meaning periodic but not always present, and not necessarily having the same phase between two active epochs of periodicity. However, such patterns were not observed when fMRI was correlated with band-limited power (BLP) calculated from local field potentials (LFP) in a similar rat model (Pan, Thompson et al. 2011).

It has been postulated that the infraslow components of electrophysiological recordings (below 0.5 Hz) play an important role in the coordination of large-scale

125

networks (Birbaumer, Elbert et al. 1990; Drew, Duyn et al. 2008; He, Snyder et al. 2008; Khader, Schicke et al. 2008). These neural frequencies are directly comparable to the frequency range of the spontaneous BOLD fluctuations used to map functional networks; however these frequencies are rarely examined as most *in vivo* neural electrophysiology is limited by amplifier hardware or electrode materials (Agranovskii, Berg et al. 1998; Geddes 2001; Geddes 2003) to frequencies above 0.1Hz.

Despite these challenges, a recent study using simultaneous imaging and DC recording (direct current from an amplifier with no highpass filter) demonstrated high correlation between infraslow LFPs and BOLD at a time lag approximating the hemodynamic delay (Pan, Thompson et al. 2013). While the correlation was localized to the area surrounding the electrodes at the time of peak correlation, other areas of the brain were also highly correlated at different lag times. At sufficiently large lags many of the same areas alternated to high negative correlation. Neither of these phenomena had been observed when using BLP of higher frequencies (Pan, Thompson et al. 2011). A possible source of the spatiotemporal structure of the correlation observed between BOLD and infraslow LFP would be a repeating, propagating dynamic in the BOLD signal. Such "fMRI spatiotemporal dynamics" have already been observed using BOLD (Majeed, Magnuson et al. 2009; Grigg and Grady 2010; Majeed, Magnuson et al. 2011) and cerebral blood volume (CBV) contrast (Magnuson, Majeed et al. 2010) in rats and humans. In rats the fMRI spatiotemporal dynamics appeared to propagate from ventral-lateral to dorsal-medial cortex, a pattern similar in appearance to the time-lagged correlation present between BOLD and infraslow LFPs. In humans (Grigg and Grady 2010; Majeed, Magnuson et al. 2011), fMRI spatiotemporal dynamics alternated between

126

two well-known networks, the default mode and task positive networks (Raichle, MacLeod et al. 2001; Fox, Snyder et al. 2005), which have been implicated in performance on attentional tasks (Drummond, Bischoff-Grethe et al. 2005; Weissman, Roberts et al. 2006) and conditions including Alzheimer's disease (Greicius, Srivastava et al. 2004) and attention deficit disorder (Tian, Jiang et al. 2006). A similar link to attention has been found for infraslow activity measured with EEG (Trimmel, Mikowitsch et al. 1990; Trimmel, Strassler et al. 2001); this may be due to infraslow phase driving amplitude of all higher frequency activity (Monto, Palva et al. 2008). If infraslow LFPs underlie the fMRI spatiotemporal dynamics, it may prove possible to map the spatial and temporal patterns of infraslow activity with whole brain coverage and spatial resolution that is unobtainable from EEG but standard for fMRI. This would provide both a new avenue for the study of neuropsychiatric diseases (Helps, Broyd et al. 2010) and insight into the organization of cognitive function.

In the present chapter, previously published results (Pan, Thompson et al. 2013) are expanded upon by examining the relationship between the infraslow LFP and the fMRI spatiotemporal dynamics. Templates from fMRI spatiotemporal dynamics, generated using BOLD alone, are compared to the spatiotemporal pattern of BOLD-LFP correlation. Also, changes over time in strength of the fMRI spatiotemporal dynamics are compared to the infraslow LFP time course directly.

The results of this study suggest that very low frequency neural activity may play a role in coordinating the large scale networks observed with BOLD; these may be the same networks whose activity is involved in both attentional processes and impaired in

127

neuropsychiatric disorders. The correlation observed between dynamic BOLD and infraslow LFP provides validity to the use of fMRI for evaluating transient properties of large scale functional networks. It demonstrates that fMRI has the potential to study the infraslow electrical activity with unprecedented brain coverage and spatial resolution, providing new insight into normal function and cognitive disorders.

4.2 Materials and Methods

ParaVision 4.0 was used for BOLD data recording, LFP data recording and data processing were performed using custom software written in *MATLAB*.

4.2.1 Animal preparation and recording

All procedures were approved by the Emory University Institutional Animal Care and Use Committee. Ten rats were anesthetized with isoflurane anesthesia with glass microelectrodes implanted into left and right interhemispheric primary somatosensory cortex of the forelimb region (S1FL) for simultaneous LFP-fMRI recording (Pan, Thompson et al. 2010). Low-frequency recording was enabled by use of direct-current capable amplifiers and silver/silver chloride leads in glass electrodes (Agranovskii, Berg et al. 1998; Geddes 2001; Geddes 2003). The procedures used here are described in detail elsewhere (Pan, Thompson et al. 2013). For some rats, data were recorded under isoflurane anesthesia, some rats were transferred to dexmedetomidine anesthesia for further recording. Dexmedetomidine was administered as a subcutaneous bolus injection of 0.05 mg/kg followed by a continuous subcutaneous infusion of 0.1 mg/kg/hour

128

(Majeed, Magnuson et al. 2009; Pawela, Biswal et al. 2009). These anesthetics are widely used for functional connectivity studies in rats (Pawela, Biswal et al. 2009; Liu, Zhu et al. 2010; Williams, Magnuson et al. 2010) but have different mechanisms of action; using both acts as a control against anesthesia-specific effects (See Appendix).

fMRI BOLD data were acquired on a 9.4 T Bruker animal scanner with a volume transmit coil and an approximately 2 cm homemade surface receive coil using gradient-echo echo-planar imaging (EPI) with TR 500ms (2Hz); TE 15 ms; one 2 mm slice; FOV 1.92 x 1.92 cm; 64 x 64 matrix. LFP data were acquired at 12 kHz from left and right S1FL, beginning several seconds prior to MRI acquisition and ending several seconds after. Between two and fifteen combined fMRI/LFP scans were recorded from each rat.

4.2.2 Data pre-processing

Six rats had data recorded while under 1.3% to 2.0% isoflurane, of these four were transferred to dexmedetomidine anesthesia for recording. Four further rats were transferred to dexmedetomidine anesthesia immediately following surgery with no isoflurane recording, for a total of ten rats. 5-15 scans were recorded for each rat (2-11 isoflurane, 3-15 dexmedetomidine). The physiology was held at protocol required parameters under both anesthetics (Body temperature mean $37.0°C \pm 0.3°C$ under isoflurane, $37.1°C \pm 0.1°C$ under dexmedetomidine, breath rate 56.9 ± 6.99 breaths per minute under isoflurane, 84.3 ± 11.3 breaths per minute under dexmedetomidine, mean $\pm$ standard deviation).

Regions of interest (ROI) for left and right S1FL were manually drawn against a two dimensional BOLD image using a rat brain atlas for reference (Paxinos and Watson 2005) as well as an outline of the whole brain. The mean signal over time in the whole brain was calculated and regressed from each voxel (Fox, Zhang et al. 2009); following this, each voxel was linearly de-trended. For LFP data, artifacts due to scanning were removed by creating a noise template on a per-rat, per-scan basis by averaging the period between each TR together. The noise template was then subtracted from the period between each TR. If the signal was saturated by the gradient amplifiers, this section of the signal was replaced by a line connecting the two endpoints of the signal where it was saturated (Allen, Josephs et al. 2000; Pan, Thompson et al. 2010).

Only data recorded at isoflurane levels of 1.7% to 2.0% were used, and only data recorded under dexmedetomidine at least 2 hours after the switch from isoflurane were used. This range of isoflurane levels was chosen as a previous study had observed robust spontaneous fluctuations within a range of 1.8% to 2.0% (Liu, Zhu et al. 2010). The time change of the BOLD signal under dexmedetomidine is more complex (Majeed, Magnuson et al. 2009; Magnuson, Majeed et al. 2010; Williams, Magnuson et al. 2010). To summarize, high power at 0.2Hz is observed after two hours suggests a stable state with measurable spontaneous oscillations in BOLD. These exclusions resulted in 2-14 scans per rat (2-8 isoflurane, 3-14 dexmedetomidine) and four rats remaining under isoflurane, seven rats remaining under dexmedetomidine.

For calculation of coherence, BOLD and LFP data were quadratically de-trended (Majeed, Magnuson et al. 2011) and set to zero mean. Mean BOLD time courses were calculated for left and right S1FL by taking the mean BOLD signal over time within the

130

respective ROI for those areas. LFP data were resampled to 2Hz to match the BOLD using an anti-aliasing filter. S1FL BOLD and LFP data were then both normalized to unit variance, zero mean.

For calculation of correlation and fMRI spatiotemporal dynamics, BOLD and LFP data were each resampled to 4Hz using an anti-aliasing filter (to facilitate a greater range of phases in templates), quadratically de-trended (Majeed, Magnuson et al. 2011), filtered to either a standard (0.005 to 0.1Hz boxcar) (Liu, Zhu et al. 2010) or empirical (based on first peak of significant coherence, see section 4.2.4) filter and set to zero mean. The empirical filter was applied directly to the fast Fourier transform of the signal to avoid unknown effects on signal phase a convolution-based filter may have produced.

4.2.3 BOLD-LFP coherence

As the BOLD-LFP relationship can likely be modeled by a consistent time shift representing a hemodynamic response to neural activity, the most interest is placed in frequencies with consistent phase difference between infraslow LFP and BOLD. Therefore, magnitude-squared coherence was calculated using the mscohere function in MATLAB between each electrode's LFP and the BOLD signal at the corresponding S1FL region of interest (the cortex surrounding the electrode). The entire possible range of zero to one Hertz (as BOLD data were 2Hz) was calculated for each scan with 2,000 frequency steps to ensure an adequately smooth result. Mean coherence spectra were calculated for both anesthetic agents by averaging across all rats, all scans and both sides of the cortex.

131

Based on where significant coherence was observed (see section 4.3.2), the first large peak appeared to be a good choice for developing an empirical filter to use on infraslow LFP and BOLD. The "first large peak" of the significant (low-frequency, see results) mean coherence was selected as follows; the start point was defined as the lowest frequency local minimum in the mean coherence and the end point was defined as the lowest frequency local minimum in the mean coherence where the mean coherence value was 50% or less than the maximum peak reached in the coherence spectra at frequencies greater than the start point.

Power within the possibly coherent frequencies (zero to one Hertz) was also calculated using a Welch spectrum. All data were resampled to 200Hz prior to this calculation and normalized to zero mean, unit variance. The Welch spectrum used a window length of 200 seconds and 99.5% overlap. 1,000 frequency steps were calculated.

4.2.4 Filtering for time-lagged BOLD-LFP correlation

Both a standard and an empirical filter were calculated on a per-anesthesia basis. The first filter was a standard hard-edged Fourier filter with a pass band based on a standard used for isoflurane anesthetized rats (0.005Hz to 0.1Hz, based on Liu, Zhu et al., 2010, p375). The second filter was empirically derived by normalizing the "first large peak" (see section 4.2.3) of the mean coherence spectrum between zero and one, applied it as a multiplicand to the fast Fourier transform (FFT) of the signal, calculated the inverse FFT of the signal and set any residual imaginary part of the signal to zero. (Note that, while computationally inefficient, it was applied as a multiplicand to the complete

132

FFT directly, because a system such as a finite impulse response filter may have created unpredictable edge effects due to the unknown effect of the shape of the empirical filter on phase.) The second filter has the advantage of only assuming that amplitudes of infraslow LFP and BOLD will be similar during time periods where their frequency content is similar; it does not make as many assumptions about the frequency characteristics of spontaneous activity itself.

Use of magnitude-squared coherence as a filter is justified because of previous work (Pan, Thompson et al. 2013) and because the frequencies of interest in this study are those that have high power during epochs of the signal where actual signal-based (not correlated noise) correlation between infraslow LFP and BOLD signals is high. Magnitude squared coherence's equation is shown in Equation 1, D is the cross spectral density function. Pearson correlation is shown in Equation 2 reformulated to be comparable to Equation 1, V is the covariance function. Note that the coherence function is calculated identically, except its magnitude is taken and squared (and thus between zero and one instead of negative one and one) and based on the cross spectral density instead of covariance.

Equation 1.

$$\frac{\left|D_{BOLD,\,LFP}\right|^2}{D_{BOLD,\,BOLD}D_{LFP,\,LFP}}$$

Equation 2.

$$\frac{V_{BOLD,\,LFP}}{\sqrt{V_{BOLD,\,BOLD}}\sqrt{V_{LFP,\,LFP}}}$$

133

BOLD data were upsampled to 4Hz to facilitate a greater range of phases for pattern-matching (see section 4.2.6), and LFP data were downsampled to 4Hz (using a resampling filter, "resample" function in *MATLAB*). Both signals had quadratic de-trend performed (Majeed, Magnuson et al. 2011). Each filter was applied separately to all data (BOLD and infraslow LFP for every scan, every rat), then data were normalized to zero mean. As this study is concerned with infraslow LFP-BOLD correlates in matched frequencies, the same filter was applied to the data for infraslow LFP and BOLD in each case.

4.2.5 Calculation of time-lagged BOLD-LFP correlation: $r_{\text{lfp-bold}}$

Pearson correlation was calculated between each electrode's LFP and the BOLD signal at every voxel for time shifts from -10s to 10s with positive numbers indicating that the BOLD came after the LFP. Results of this calculation will be referred to as $r_{\text{lfp-bold}}$. The range of ±10s was selected to be more than sufficient to capture previously observed localized correlations in rats between the simultaneously recorded signals (Pan, Thompson et al. 2011; Pan, Thompson et al. 2013) but was set larger so that results would not be biased toward only the expected time shifts. Visual observation during electrode implantation under isoflurane anesthesia demonstrated that bursts in the LFP signals were in the downward direction. Therefore, to follow previous work that was done on downward bursting LFPs, correlation coefficients were inverted (Pan, Thompson et al. 2011; Pan, Thompson et al. 2013).

134

The empirically derived filter was used for all further analysis as it produced more consistent results (Table 4.1). No Fisher transformation or other normalization was used on $r_{\text{lfp-bold}}$, as some data were calculated with an empirical filter which may have had unpredictable effects on such a transform. To account for this lack of normalization, only p values from comparisons to randomized data were used to test for significance and some tests were replicated using median values instead of mean values (see section 4.2.10).

Movies were created using the "jet" color scale in *MATLAB* and a range of $r_{\text{lfp-bold}}$ between ±0.4 and examining only time shifts of -3s to 10s. A researcher (the author of this dissertation) visually inspected the movies for alternation between positive and negative correlation, as well as propagation from ventral to dorsal cortex, dorsal to ventral cortex, or neither. Example movies are included as multimedia files in section 4.4.

4.2.6 fMRI spatiotemporal dynamic template generation

For a statistical examination of dynamic correlation patterns, templates of inherent fMRI spatiotemporal dynamics in the BOLD signal were generated for each anesthesia, rat and scan. This also simultaneously generated a time course of sliding correlation with the template, which can be considered template strength over time. The algorithm used to generate these templates is described in Majeed et al. (Majeed, Magnuson et al. 2011), however the specific parameters were unique to this study and are as follows: The template length was set to the frequency location of the center of mass of the empirically derived filter; this was intended to force the template to be only one

135

period of the fMRI spatiotemporal dynamic. The start point of the template was held constant at 250 seconds, as, in rats, the start point is unlikely to affect the resulting fMRI spatiotemporal dynamic in any sense other than its phase (Majeed, Magnuson et al. 2009; Majeed, Magnuson et al. 2011). The region of interest was set to a combination of both the left and right S1FL ROIs. Thresholds were set arbitrary low to ensure convergence; the first threshold was 0.001 (1/100th of default) for 3 iterations (default) and the second threshold was 0.002 (1/100th of default) for a up to 10,000 (500 times default) iterations.

Previous work demonstrated that templates had a similar and highly reproducible spatiotemporal patterns across different scans and subjects, but the start point for each template (its phase) varied. (Majeed, Magnuson et al. 2009; Majeed, Magnuson et al. 2011). To correct for this, templates were set to the same start point (phase) on a per-anesthesia basis in the following manner: Templates were generated separately for each rat and each scan. Every individual template had normalized spatial correlation calculated ("normxcorr2" function in *MATLAB*) between it and the first rat, first scan's template. This was done at all possible circular time shifts between the template in question and the first rat, first scan's template (e.g. a circular time shift of 1 would remove one time point's frame from the end and place it at the beginning). At each time shift, spatial correlations were calculated at multiple spatial shifts: all spatial shifts from no shift up to 25% of the maximum shift were calculated. The spatial correlation values at all spatial shifts for a given time shift were then summed. The circular time shift that resulted in the largest sum of spatial correlation values was applied to the template and was used for all further analysis of the template itself. In addition, the amount of this shift, in seconds, was also applied as a non-circular, zero-replacing time shift (e.g. a time shift of 1 would

136

remove one point from the end and add a zero to the beginning) to the plots of template strength versus time.

4.2.7 LFP-BOLD correlation versus fMRI spatiotemporal dynamic templates: $r_{lfp\text{-}bold\text{-}template}$

To compare the spatiotemporal distribution of high signal within the frame shifted, fMRI spatiotemporal dynamic templates to the spatiotemporal distribution of correlation between infraslow LFP and BOLD, the following analysis was done: Normalized spatial correlation was calculated between aligned templates and $r_{lfp\text{-}bold}$ values to produce a result referred to as $r_{lfp\text{-}bold\text{-}template}$. This was done at all possible frame shifts given the lengths of $r_{lfp\text{-}bold}$ and the template. Maximum normalized spatial correlation between the template and $r_{lfp\text{-}bold}$ was calculated on a per-frame basis using the "normxcorr2" function in *MATLAB*, however only the central (zero shift) correlation was taken in each case as templates and $r_{lfp\text{-}bold}$ are co-registered as they came from the same scan. As bursting was in the negative direction correlation coefficients were inverted (Pan, Thompson et al. 2010; Pan, Thompson et al. 2011; Pan, Thompson et al. 2013). $r_{lfp\text{-}bold\text{-}template}$ values were re-centered in terms of frame shift to be relative to their maximum values. A brief summary of these methods is shown in Figure 4.1.

4.2.8 Correlation between template strength and LFPs: $r_{\text{lfp-template}}$

To compare the occurrences in time of fMRI spatiotemporal dynamics to the infraslow LFP signal directly, the following analysis was done: Pearson correlation was calculated between the aligned template strength time courses and the processed LFP signal in each electrode to produce values referred to as $r_{\text{lfp-template}}$. This was done at time shifts from -20s (LFP signal shifted forward relative to sliding correlation with template) to 20s (LFP signal shifted backward relative to sliding correlation with template). As bursting was in the negative direction correlation coefficients were inverted (Pan, Thompson et al. 2010; Pan, Thompson et al. 2011; Pan, Thompson et al. 2013). $r_{\text{lfp-template}}$ values were re-centered in terms of time shift to be relative to their maximum values. A brief summary of these methods is shown in Figure 4.1. To ensure that the lack of normalization for correlation values would not bias results, $r_{\text{lfp-bold}}$ was also calculated with median instead of mean values used (see section 4.2.10).
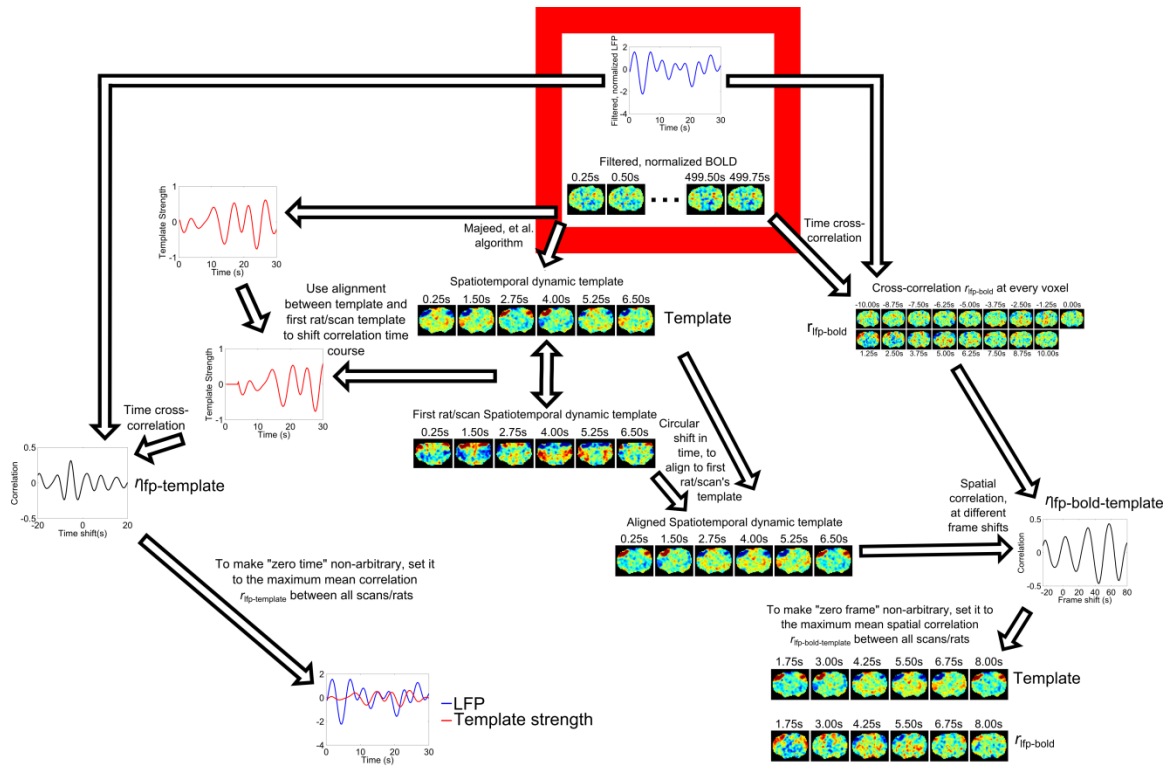
Figure 4.1: Summary of the methods used to produce and align $r_{\text{lfp-bold-template}}$ and $r_{\text{lfp-template}}$. The starting point is highlighted in the red box, with filtered and normalized LFP and BOLD signals. **Right side:** The filtered, normalized BOLD signal is cross-correlated at numerous time lags with the filtered, normalized infraslow LFP signal to produce $r_{\text{lfp-bold}}$. An fMRI spatiotemporal dynamic template is calculated from the filtered, normalized BOLD signal alone. As templates are produced with arbitrary phases, all templates are circularly shifted to align with the first rat, first scan's template for that electrode and anesthesia. Spatial correlation $r_{\text{lfp-bold-template}}$ is calculated between the aligned template and $r_{\text{lfp-bold}}$. To have a non-arbitrary "zero" frame shift, the zero frame shift is set to the maximum mean $r_{\text{lfp-bold-template}}$. **Left side:** An fMRI spatiotemporal dynamic template is generated from the filtered, normalized BOLD signal. The algorithm also produces a time course of correlation with the template, which is template strength versus time. As templates are produced with arbitrary phases, all templates are circularly shifted to align with the first rat, first scan's template for that electrode and anesthesia. This shift is used to non-circularly align the phase of the template strength time course. Time cross-correlation is done between the aligned template strength time course and the filtered, normalized infraslow LFP signal to produce $r_{\text{lfp-template}}$. To have a non-arbitrary "zero" time point, the zero time point is set to the maximum mean $r_{\text{lfp-template}}$.

139

4.2.9 Estimation of period of autocorrelation series

Results for $r_{\text{lfp-bold-template}}$ and $r_{\text{lfp-template}}$ that appeared similar to an autocorrelation series of a periodic process had the phase of the hypothetical periodic process estimated. The period of a periodic process can be calculated from the first several peaks of its autocorrelation series by averaging the expected period from each of those peaks. For example, with the time shifts of the positive peaks (PPL on the left and PPR on the right) and the time shifts of the negative peaks (NPL on the left and NPR on the right). These are shown in Figure 4.2. The period can be estimated, in seconds, by Equation 3. If the positive peak on the right is unavailable, the estimation can be done by Equation 4.

Equation 3.
$$\frac{[(PP_L + PP_R) - (NP_L + NP_R)]}{4}$$

Equation 4.
$$\frac{[(PP_L) - (NP_L + NP_R)]}{3}$$

_____
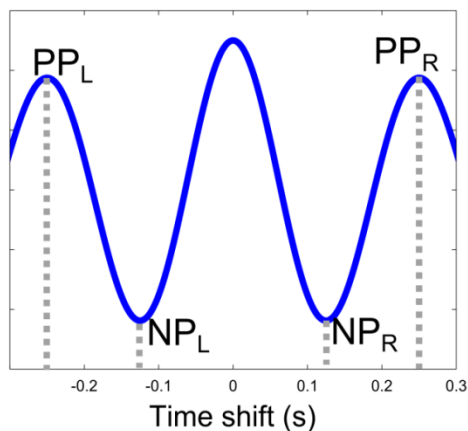
Figure 4.2: Estimation of autocorrelation period. The locations of positive peaks PP_L and PP_R and negative peaks NP_L and NP_R are shown around the central peak of a hypothetical autocorrelation spectrum of a sinusoidal process.

140

4.2.10 Use of median instead of mean

As normalization was not performed on correlation coefficients (see section 4.2.5), to validate the methods an additional test was done that did not use mean values but instead used median values (50th percentiles) which are independent of assumptions of the shape of the distribution of data. As the means of correlation values were only taken at the last step, the values calculated for $r_{\text{lfp-template}}$ were used for this test, taken as a median across all rats and scans for each anesthesia and electrode. Identical significance testing was done as was done when a mean was taken (see section 4.2.14).

4.2.11 Test of preliminary caudate-putamen electrical recording

As reported in Pan, et al. (Pan, Thompson et al. 2013), preliminary data had been recorded under the same protocol, with the exception of the electrode being implanted into the caudate-putamen instead of S1FL. The same data are used here as it would be informative to future work to know if the present chapter can be translated to non-cortical locations.

This datum was subjected to identical pre-processing as the interhemispheric S1FL data, using the empirical filter used in this study for S1FL and dexmedetomidine anesthesia, and had $r_{\text{lfp-bold}}$ and $r_{\text{lfp-bold-template}}$ calculated on the single scan. The only change made to processing was use of regions of interest drawn in the left and right caudate-putamen for calculation of the fMRI spatiotemporal dynamic template.

141

4.2.12 Power spectrum of template strength versus time

For each anesthesia, rat and scan, a power spectra was calculated on the template strength (time course of sliding correlation with the template). This was done using a Welch spectrum with 1,000 frequency steps, 200s window length and 99.5% overlap.

4.2.13 Incorrectly paired scans from the same rat

For a single rat, one BOLD scan was taken and combined with an LFP recording from a different BOLD scan. The values of $r_{\text{lfp-bold-template}}$ were calculated for it at time shifts from -60s to 60s and visually examined as a movie to determine if any dynamic correlations appeared that were similar to that of actual data.

4.2.14 Control data and multiple comparisons testing

In all cases, significance was tested using artificial null distributions to create probability values (p values), and control against multiple comparisons on these p values.

To generate p values for the coherence spectrum, the following process was used: An artificial null distribution was created by, prior to the quadratic de-trend, randomly circularly shifting each LFP data time course over time (uniformly distributed between one sample and the length of the signal minus one sample). This allowed inherent frequencies present in both signals to be kept, but shuffled where epochs of activity within a given frequency may have occurred in both signals. This was done 100 times

142

and mean coherence spectra between infraslow LFP and BOLD were calculated each time. At each of the 2,000 frequency steps the 100 randomization runs were taken as a null distribution; a one-tailed p value was then calculated for the actual value using the cumulative distribution function of the null distribution. This produced 4,000 p values (2 anesthesia, 2,000 frequency steps).

To test $r_{\text{lfp-bold-template}}$ and $r_{\text{lfp-template}}$ for significance, the following process was used: Analysis described in sections 4.2.5 through 4.2.8 were repeated, except that, within each rat and anesthesia combination, which LFP recordings corresponded to which BOLD scans was randomized. This was done 10 times without replacement (derangement), producing a range of mean $r_{\text{lfp-bold-template}}$ and mean $r_{\text{lfp-template}}$ values across all tested time/frame shifts. For each anesthesia, these values were combined across electrodes and time/frame shifts to form null distributions of $r_{\text{lfp-bold-template}}$ and $r_{\text{lfp-template}}$. Two-tailed p values were calculated for each actual $r_{\text{lfp-bold-template}}$ and $r_{\text{lfp-template}}$ value from the cumulative distribution function of their respective null distributions.

For control against multiple comparisons, each family of p values (here defined as each figure or table being its own family of hypotheses) was tested using Sequential Goodness of Fit (SGoF) (Carvajal-Rodriguez, de Una-Alvarez et al. 2009) to find a p value threshold that allowed only 5% family-wise error rate (FWER).

SGoF controls FWER in the weak sense (a large number of small p values is significant, rather than individual p values being sufficiently small) so it has the advantage that type II error rate (false negative) does not increase as the number of tests increase. In addition, it can reject p values of zero as non-significant. This is

143

advantageous as the data randomization used here can result in p values of zero if an actual value falls outside of the generated null distribution.

4.3 Results

Data were acquired from ten Sprague-Dawley rats, under either isoflurane anesthesia (four rats) or dexmedetomidine (seven rats, one of which also had data recorded under isoflurane) using simultaneous recording of broadband (0-100Hz) LFP and single-slice fMRI BOLD imaging (Pan, Thompson et al. 2010) (Figure 4.3). These anesthetics are widely used for functional connectivity studies in rats (Pawela, Biswal et al. 2009; Liu, Zhu et al. 2010; Williams, Magnuson et al. 2010) but have different mechanisms of action; using both acts as a control against anesthesia-specific effects (See Appendix). Two fine-tip (1 - 5 MΩ impedance) glass electrodes were used, implanted in left and right primary somatosensory cortex lower forelimb region (S1FL).

4.3.1 Data Quality

Simultaneous recording was successful, as the artifacts due to simultaneous fMRI recording could be removed from the LFP signal and the LFP electrodes caused minimal artifacts in the EPI images (Figure 4.3).

144
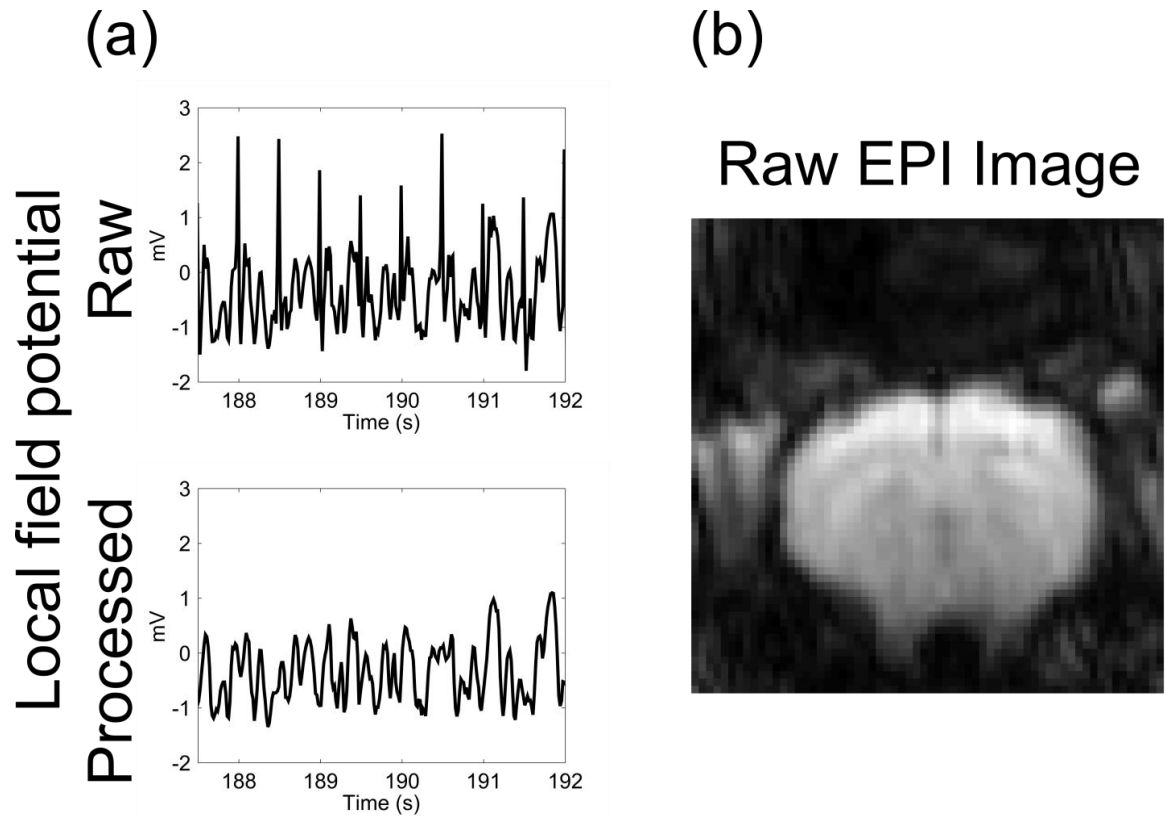
Figure 4.3: Signal quality. **(a)** Sample LFP signal before ("Raw") and after ("Processed") fMRI noise removal. Note that both the recovery artifact during the non-saturated epochs, and the saturated spikes are removed. **(b)** Sample BOLD fMRI image. Note that there is minimal distortion due to the glass electrodes and that cortical versus subcortical structures can be distinguished.

145

Temperature was held relatively constant across rats ($37.0°C \pm 0.3°C$ under isoflurane, $37.1°C \pm 0.1°C$ under dexmedetomidine, mean $\pm$ standard deviation, Figure 4.4 a) but breath rate varied by anesthesia as rats were allowed to breath freely (56.9 ± 6.99 breaths per minute under isoflurane, 84.3 ± 11.3 breaths per minute under dexmedetomidine, significant difference with $p = 2.25 \times 10^{-12}$, two sample T test, Figure 4.4 b).

Broadband LFP variance had a greater range of values under dexmedetomidine, but was not significantly different than under isoflurane (0.0390 ± 0.0236 mV under isoflurane, 0.122 ± 0.730 mV under dexmedetomidine, Figure 4.4 c).

4.3.2 BOLD-LFP coherence

Coherence between BOLD from S1FL and infraslow LFP from the same location is plotted in Figure 4.5. Significance testing using Sequential Goodness of fit (SGoF) (Carvajal-Rodriguez, de Una-Alvarez et al. 2009) produces a threshold of $p = 0.0100$. Isoflurane was potentially significant for frequencies from 0.037 to 0.159Hz. Dexmedetomidine was potentially significant for frequencies from 0.034 to 0.357Hz, from 0.358 to 0.359Hz, 0.367 to 0.368Hz and 0.369 to 0.377Hz.

The "first large peak" (see methods) of coherence was defined as from 0.038 to 0.184Hz under isoflurane and 0.045 to 0.304Hz under dexmedetomidine.

146
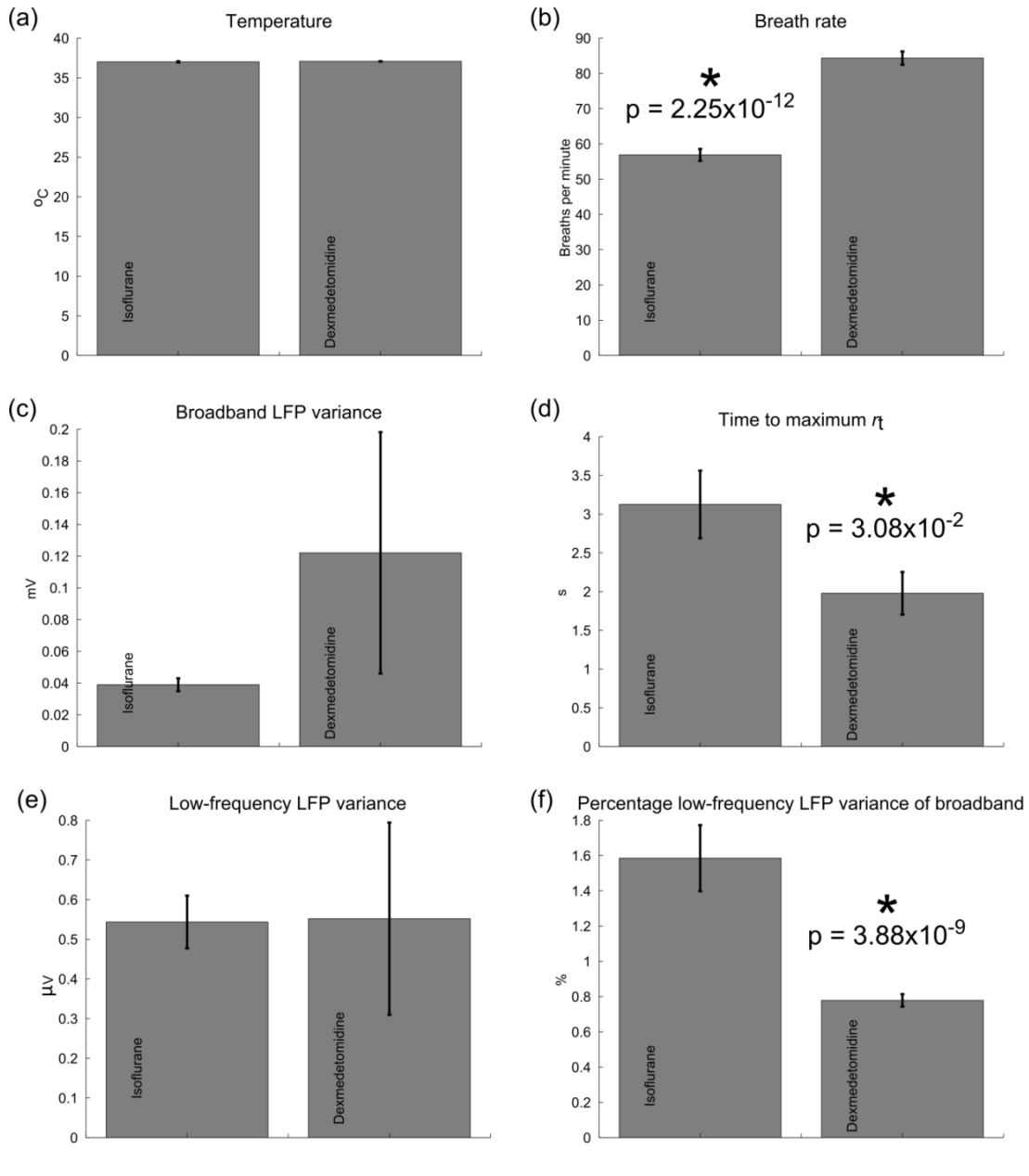
Figure 4.4: Bar graphs for various parameters as compared between isoflurane and dexmedetomidine anesthesias; error bars are one standard error. Asterisks indicate significant difference by two sample, two-tailed T test between the two anesthesia. **(a)** Temperature, degrees Celsius, **(b)** Breath rate, breaths per minute, **(c)** Variance in LFP signals at all recorded frequencies in millivolts, **(d)** Amount of time LFP signal had to be shifted backward in time relative to BOLD signal to find maximum correlation, **(e)** Variance in LFP signals after filtering using the anesthesia-specific, empirical filter, **(f)** Variance in the filtered LFP signal from (e) divided by variance in the non-filtered LFP signal from (c).

147
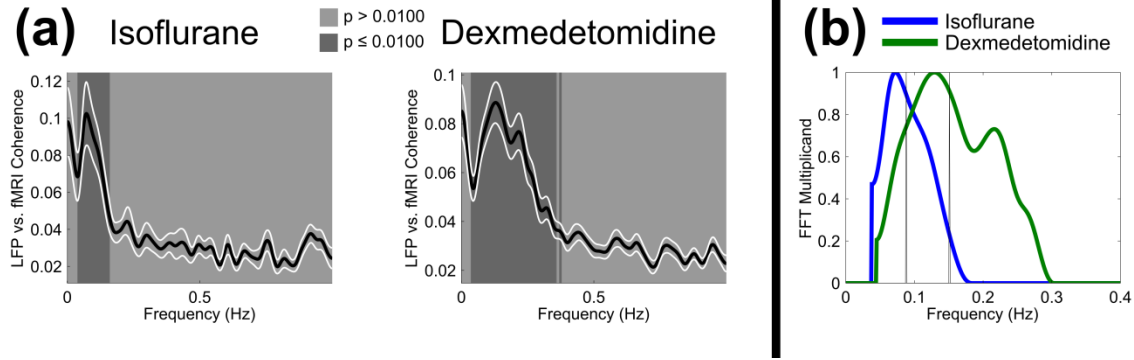
Figure 4.5: Significant coherence between infraslow LFP and BOLD produces an empirical filter. **(a)** Magnitude-squared coherence, combined across left and right hemispheres, between infraslow LFP signal recorded from S1FL and BOLD signal from that location. Isoflurane anesthesia is shown on the left, dexmedetomidine on the right. Areas significantly different from randomly shifted pairs are shown in dark gray (p ≤ 0.0100, SGoF at 5% FWER). **(b)** Empirical filter based on coherence, shown for both anesthesias. The filter is applied as a multiplicand to the fast Fourier transform (FFT) of the original signal. The vertical gray line represents the center of mass of each filter. N=92 for dexmedetomidine, 7 rats, 3-14 runs per rat, 2 electrodes. N=34 for isoflurane, 4 rats, 2-8 runs per rat, 2 electrodes.

_____

Table 4.1: Filter comparison. This table illustrates mean and one standard deviation (SD) for maximum $r_{\text{lfp-bold}}$, cross-correlation between infraslow LFP and BOLD signals in S1FL and the time shift to this maximum correlation value. Values for both a standard filter with a 0.005-0.1Hz boxcar frequency profile (Liu, Zhu et al. 2010) and an empirically generated filter (Figure 4.5b) are shown. In every case the standard deviation is higher for the standard filter, in particular the standard filter does not produce a reproducible time shift between infraslow LFP and BOLD. N=46 for dexmedetomidine, 7 rats, 3-14 runs per rat. N=17 for isoflurane, 4 rats, 2-8 runs per rat.

	Isoflurane				Dexmedetomidine			
	Time shift		Value		Time shift		Value	
	Mean	**SD**	**Mean**	**SD**	**Mean**	**SD**	**Mean**	**SD**
Standard Filter	1.5s	±4.5s	$r_t = 0.52$	±0.13	1.2s	±4.4s	$r_t = 0.47$	±0.10
Empirical Filter	3.1s	±2.5s	$r_t = 0.51$	±0.1	2.0s	±2.6s	$r_t = 0.40$	±0.08

148

Power spectra for LFP and BOLD under both anesthesia are illustrated in Figure 4.6, however, no obvious peaks are visible except in the case of dexmedetomidine BOLD signal. The approximately 0.2Hz peak seen in the dexmedetomidine BOLD signal is related to the time change of the BOLD signal under dexmedetomidine and cerebral blood volume (Majeed, Magnuson et al. 2009; Magnuson, Majeed et al. 2010; Williams, Magnuson et al. 2010).

4.3.3 Empirical vs. standard filters

Differences between the standard and empirical filter are shown in Table 4.1. Standard deviation in maximum correlation value for $r_{\text{lfp-bold}}$ and time shift to maximum $r_{\text{lfp-bold}}$ are lower using the empirical filter for both anesthetics, indicative of greater error when the standard filter is used. For both filters, a significant difference in anesthetics was seen in terms of maximum $r_{\text{lfp-bold}}$ value (p = 3.08×10^{-2} for standard filter, p = 7.69×10^{-9} for empirical filter, two sample T tests) and for the empirical filter a significant difference in anesthetics was seen in terms of the infraslow LFP-BOLD time shift that resulted in maximum $r_{\text{lfp-bold}}$ (p = 3.10×10^{-2}, two sample T test). The significant difference in time shifts between anesthetics replicates previous work (Pan, Thompson et al. 2013). For the empirical filter, the difference in time shifts between anesthesias is shown in Figure 4.4d.

While in some cases both filters produced similar results, an example of what is indicated by this greater error is shown in Figure 4.7. In the case shown, the standard filter produced maximum correlation at unlikely time shifts (BOLD events precede LFP

149

events) and, for the dexmedetomidine example, the highest correlation is not within the cortex. Conversely the lower-error empirical filter has produced high correlation in the cortex, and relatively close to the locations of electrode implantation.

Because it produced results with lower error but still produced high correlation values, the empirical filter was used for all further analysis. Within data that was filtered with the empirical filter, low-frequency LFP variance was similar (0.544 ± 0.387 µV under isoflurane, 0.552 ± 2.32 µV under dexmedetomidine, Figure 4.4 e). However the variance from the filtered data divided by the total variance was significantly higher under isoflurane ($1.59 \pm 1.09\%$ under isoflurane, $0.778 \pm 0.339\%$ under dexmedetomidine, $p = 3.88 \times 10^{-9}$, two sample T test, Figure 4.4 f). This suggests that, while there was more neural activity overall under dexmedetomidine (as would be expected, see Appendix), and despite using different filters for each anesthetic, the amount of infraslow electrical activity we were observing under the two anesthetic paradigms was not dissimilar.
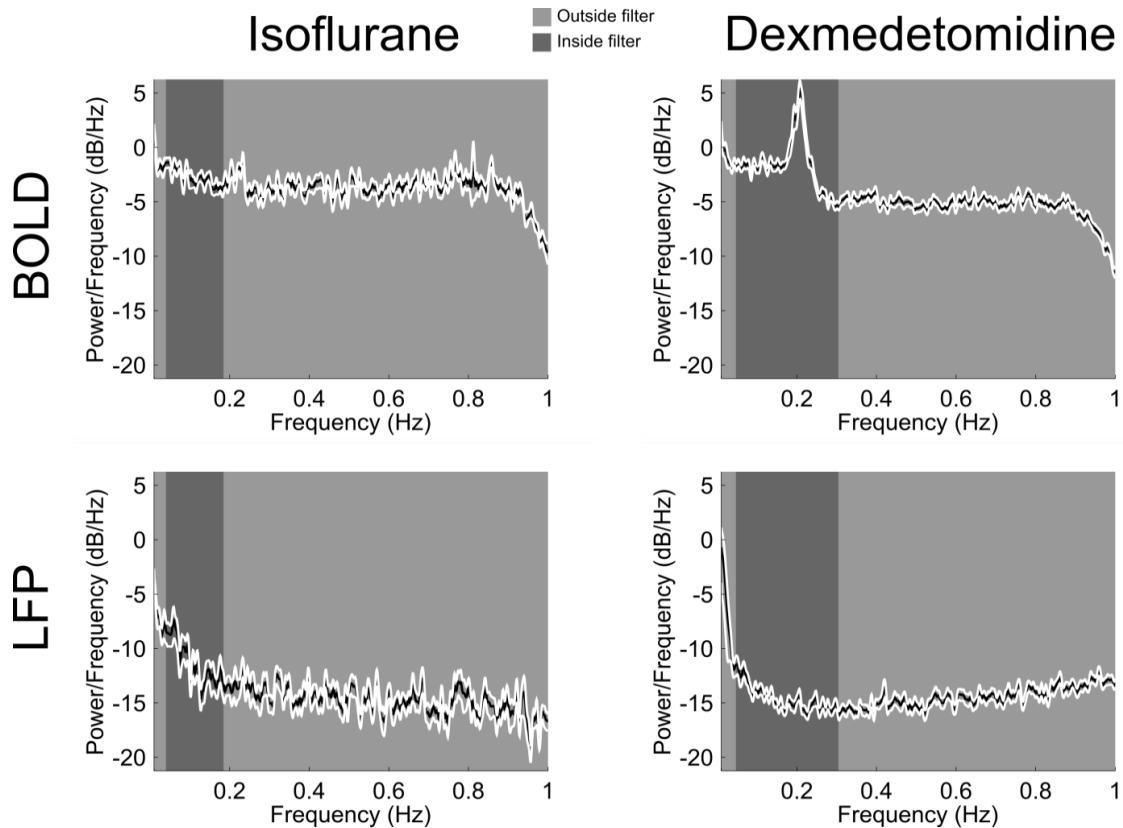
Figure 4.6: Plots of power spectra between zero and one Hertz under isoflurane (left column) and dexmedetomidine (right column) anesthesias and for the mean signal in S1FL in BOLD (top row) and for the signal recorded from implanted LFP electrodes (bottom row). The black line with the white edges is the mean across all rats, scans and both hemispheres. Light gray background is outside of the empirical filter for that anesthesia (see Figure 4.5b), dark gray is within the empirical filter.
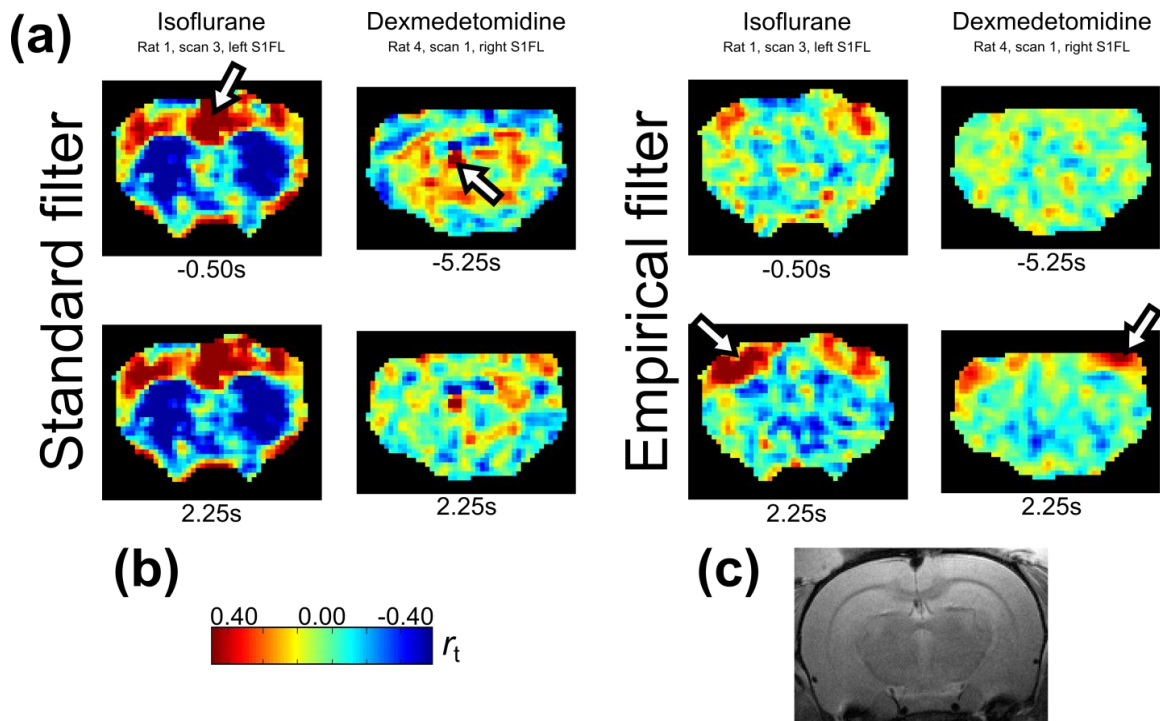
Figure 4.7: Filters comparison. Example correlation results using a standard filter (Liu, Zhu et al. 2010) (0.005-0.1Hz boxcar) versus the filter that was empirically determined from coherence (Figure 4.5). **(a)** The correlation coefficient $r_{\text{lfp-bold}}$ is shown across the rat cortex for both anesthesias and filters. In the example shown, the left electrode is used for isoflurane anesthesia and the right electrode is used for dexmedetomidine anesthesia. Images shown are standard (reversed from radiological) convention. The time shifts between the BOLD and LFP signals where correlation was maximum for both filters is shown for results from both filters (For the standard filter, -0.50s for isoflurane and -5.25s for dexmedetomidine, for the empirical filter, 2.25s for both anesthesia). Positive numbers indicate BOLD shifted later in time than LFP. Arrows point to the maximum correlation value for each filter and anesthesia. Under the empirical filter, maximum correlation is local to the electrode location, at a time shift consistent with a hemodynamic response (Pan, Thompson et al. 2013), and the correlation map is much less cluttered. **(b)** Scale bar for $r_{\text{lfp-bold}}$. **(c)** Anatomical fMRI image in the same plane as the functional fMRI images used to calculate correlation.

Table 4.2: Visual observation of dynamics in correlation between BOLD and LFP ($r_{\text{lfp-bold}}$). The number shown is total number of that dynamic observed, out of the total number of observations, including observation of both hemispheres, both electrodes, all rats and all scans.

	Positive/Negative Alternation	Cortical ventral-dorsal propagation	Cortical dorsal-ventral propagation
Isoflurane	66/68 (97.1%)	35/68 (51.5%)	6/68 (8.82%)
Dexmedetomidine	180/184 (97.8%)	127/184 (69.0%)	22/184 (12.0%)

_____

4.3.4 Time-lagged BOLD-LFP correlation

Movie files (examples included in section 4.4) were created for Pearson correlation between LFP and BOLD at different time shifts, referred to as $r_{\text{lfp-bold}}$. Each frame of the movie represented a time shift from BOLD 3s prior to LFP to BOLD 10s after LFP in 0.25s intervals. Table 4.2 shows the results from qualitative visual examination of these movies. Almost all (>97%) correlation time series showed alternation between positive and negative correlations, and over half (51.5% for isoflurane, 69.0% for dexmedetomidine) of all correlation time series showed cortical ventral-dorsal propagation. This matches the direction of propagation previously observed for fMRI spatiotemporal dynamics in the rat cortex (Majeed, Magnuson et al. 2009; Majeed, Magnuson et al. 2011). Approximately one in ten (8.82% isoflurane, 12.0% dexmedetomidine) $r_{\text{lfp-bold}}$ patterns showed cortical dorsal-ventral propagation. For the rest of correlation time series, if there was any direction to propagation it was not readily discernible. Figure 4.8 illustrates $r_{\text{lfp-bold}}$ at three spatial points along the cortex; more dorsal cortical locations have peak signal at longer lag times, suggesting

153

propagation, and the correlation alternates between high positive and high negative as the time shift increases. LFP-BOLD correlations across entire slices are shown in Figure 4.9 parts a and c, and are included as movie files in section 4.4.

4.3.5 LFP-BOLD correlation and fMRI spatiotemporal dynamic templates

fMRI spatiotemporal dynamic templates were generated for all rats and scans using the Majeed et al. algorithm (Majeed, Magnuson et al. 2011), a pattern-finding method that iteratively locates occurrences of a repeating fMRI spatiotemporal dynamic pattern and averages them together to create a template of the pattern. The resulting template describes a typical pattern of the spatial evolution of the spontaneous BOLD signal over time; these patterns tend not to be truly periodic, but repeat several times over isolated epochs of time, and thus are referred to as *quasi-periodic* (Majeed, Magnuson et al. 2011). The inverse of the frequency center of mass from the empirical filters was used as the template length (11.25s for isoflurane, 6.50s for dexmedetomidine, see Figure 4.5b) and templates were aligned in phase to the first template that was generated for that anesthetic. Examples of these templates are shown in Figure 4.9 parts b and d. The patterns of BOLD signal propagation are similar in appearance to the patterns of time-lagged BOLD-LFP correlation shown in Figure 4.9 parts a and c. Note that templates are generated using BOLD fMRI data alone, independent of electrophysiology.

(a)

(b)
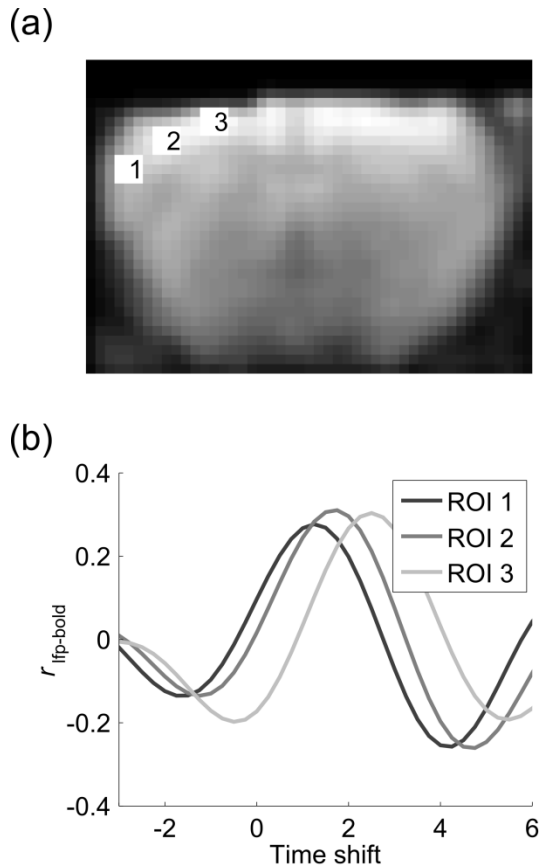
Figure 4.8: Dynamic correlation by location. **(a)** Mean BOLD image across an fMRI scan, three regions of interest (ROI) are shown numbered. An LFP electrode is implanted contralaterally to ROI 2. **(b)** Cross-correlation between the LFP signal at ROI 2 and the BOLD signal at every ROI. Note that the more ventral and lateral ROI 1 peaks at an earlier time shift while the more dorsal and medial ROI 3 peaks at a later time shift. Note also that ROI 2, closest to the contralateral homologue of the site of electrode implantation, has the greatest correlation value. N = 1; data are from rat 7, scan 5.
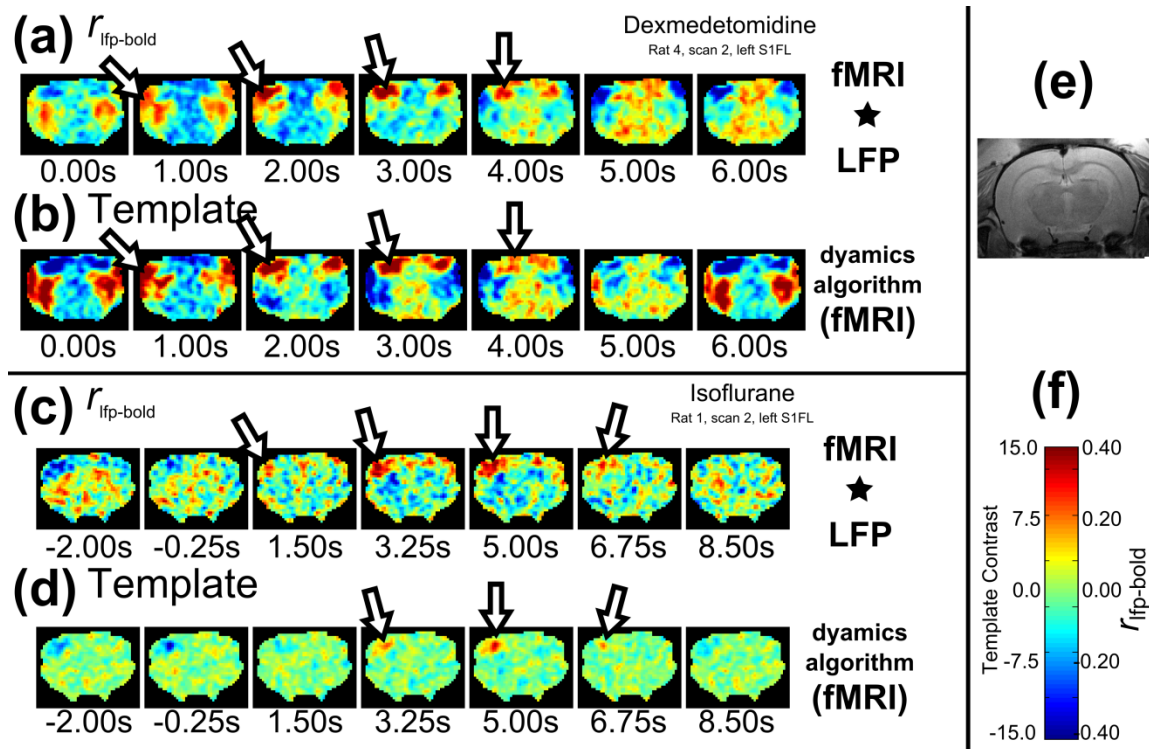
Figure 4.9: Examples of spatiotemporal dynamics from LFP-BOLD correlation and fMRI spatiotemporal dynamics from BOLD signal alone. **(a, c)** Pearson correlation between BOLD and LFP at shown time shifts, $r_{\text{lfp-bold}}$, under dexmedetomidine (a) and isoflurane (c) anesthesia **(b, d)** Template generated from the BOLD signal alone, using the Majeed, et al. algorithm (Majeed, Magnuson et al. 2011) aligned based on the maximum mean spatial correlation between the two patterns shown in Figure 4.10. Arrows in a, b, c, d show propagation of signal in typical ventral to dorsal direction along cortex. **(e)** Anatomical fMRI image of rat brain at slice approximately aligned to BOLD images. **(f)** Scale bar for a, b, c and d. **Note:** Parts a, b, c, and d are included as movie files in section 4.4. N = 1 for each plot, the specific rat/scan/electrode is indicated on the plot.

To quantify the similarity between the time-lagged infraslow LFP-BOLD correlation ($r_{lfp-bold}$) and the fMRI spatiotemporal dynamic template, spatial correlation of the two patterns was calculated and denoted $r_{lfp-bold-template}$. A maximum mean value of $r_{lfp-bold-template} = 0.233$ was observed for isoflurane and $r_{lfp-bold-template} = 0.275$ for dexmedetomidine (mean across electrodes, scans, rats). The similarity of the two patterns under both anesthetics suggests that they share a common origin and that the low frequency LFPs are likely to contribute to the patterns found in the BOLD–based templates.

The frame shift of maximum $r_{lfp-bold-template}$ was labeled as frame zero (as template phases are arbitrary). At positive and negative frame shifts, side-peaks were observed. The result appeared very similar to a plot of autocorrelation versus time lag of a signal containing a single periodic process (compare Figure 4.2 to Figure 4.10). Considering it to be such indicated a period of approximately 12.33s for isoflurane and 6.06s for dexmedetomidine (Equation 3, Equation 4). Figure 4.10 and Figure 4.11 illustrate $r_{lfp-bold-template}$ versus frame shift; exact values can be found in Table 4.3. Both the maximum mean value and its side-peaks were statistically significant when compared to a control by randomization (p ≤ 0.0160, significant at 5% family-wise error rate (FWER) by Sequential Goodness of Fit (SGoF) (Carvajal-Rodriguez, de Una-Alvarez et al. 2009)). The observed period from autocorrelation was consistent with the period of the templates themselves (see section 4.3.9). This result demonstrated that the spatiotemporal structure of LFP and BOLD correlation matches what has been seen previously in fMRI-only studies (Majeed, Magnuson et al. 2009) and suggests that the infraslow LFPs may contribute to a large-scale modulation of cortical excitability.

157
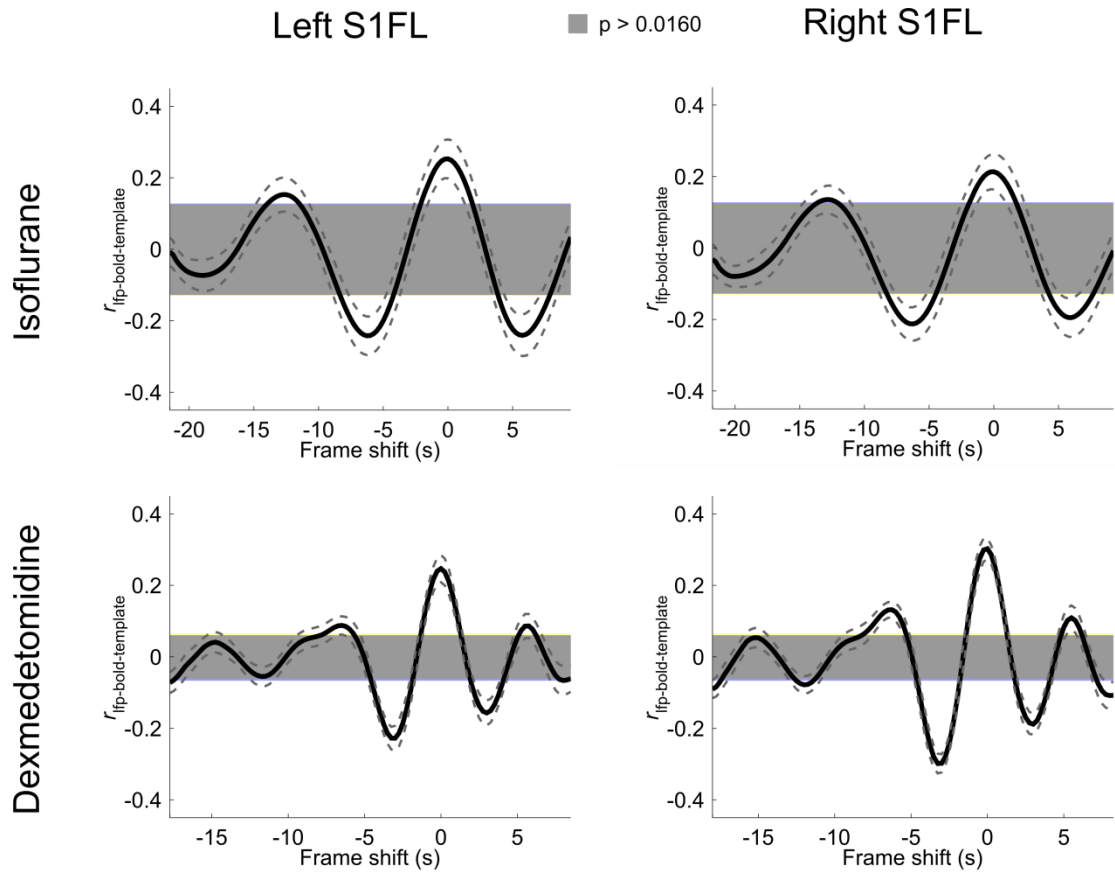
Figure 4.10: $r_{\text{lfp-bold-template}}$; normalized spatial correlation between $r_{\text{lfp-bold}}$ (generated from LFP-BOLD correlation, Figure 4.9 parts a and c) and fMRI spatiotemporal dynamic templates (generated from BOLD alone, Figure 4.9 parts b and d) plotted versus frame shift from maximum. Black solid line is mean of all rats and scans, dark gray dashed line is one standard error. Light gray areas are not significant ($p > 0.0160$), other areas are significant (SGoF, 5% FWER). Top row is isoflurane anesthesia, bottom row is dexmedetomidine anesthesia. Numerical results are shown in Table 4.3, individual rats are shown in Figure 4.11. In every case, $r_{\text{lfp-bold-template}}$ is significant for the largest peak and side peaks, and approximately resembles a down-scaled autocorrelation series. N=46 for dexmedetomidine, 7 rats, 3-14 runs per rat. N=17 for isoflurane, 4 rats, 2-8 runs per rat.
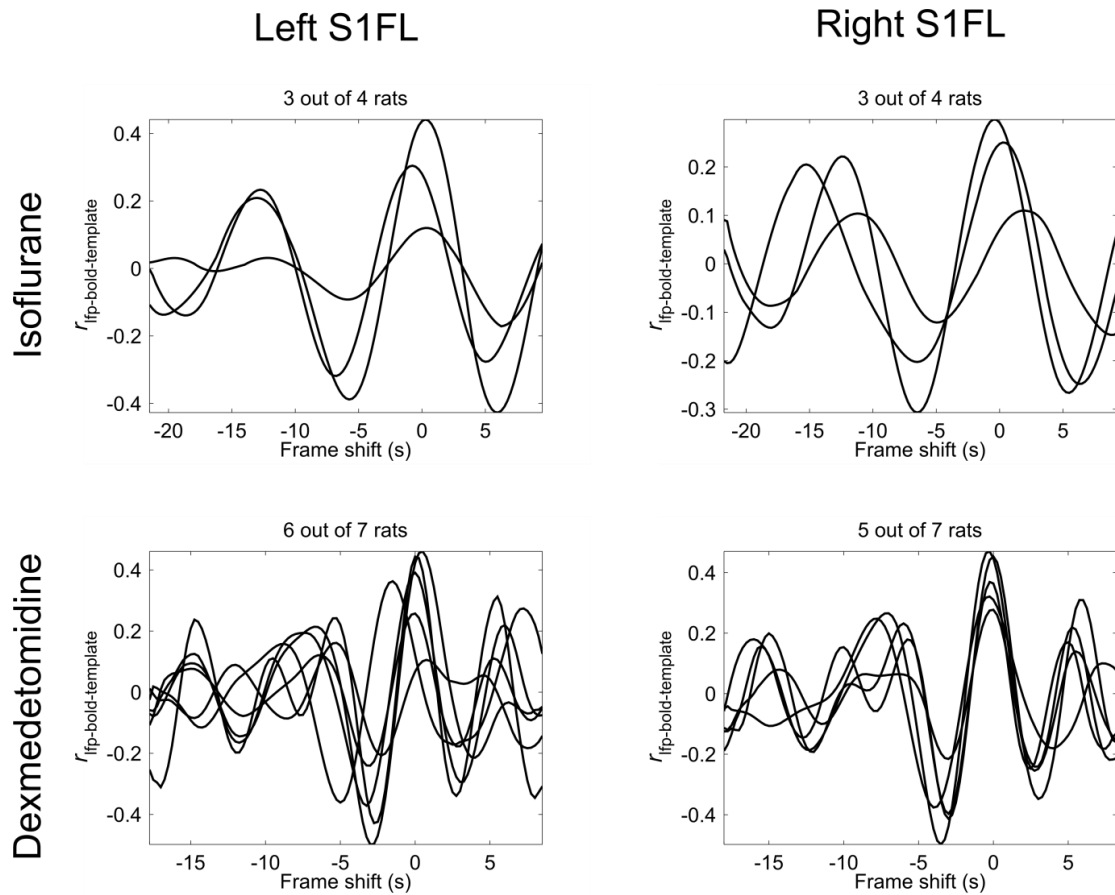
Figure 4.11: As Figure 4.10, except individual $r_{\text{lfp-bold-template}}$ values are plotted for each electrode and rat, for rats that fell within one standard deviation of the mean for frame shift location of maximum value. Note that, unlike Figure 4.14, results are consistent across different rats and overall results can be seen even in a single rat. Each rat represents the mean of 2-14 scans.

Table 4.3: Numerical results for calculation of $r_{\text{lfp-bold-template}}$, the spatial correlation between the infraslow LFP-BOLD correlation spatiotemporal dynamic, and the fMRI spatiotemporal dynamic template generated from BOLD alone. This is from values plotted in Figure 4.10. Each row represents a separate condition for site of electrode implantation (Left or Right) and anesthesia (Isoflurane or Dexmedetomidine. Columns are as follows. **Mean:** Maximum mean $r_{\text{lfp-bold-template}}$, considered to be a frame shift of zero. Mean ± one standard deviation. **Period estimate:** Estimated period if it is assumed to be an autocorrelation series. **Freq. estimate:** One divided by the period estimate. **Pos. corr. significance:** Frame shifts where data randomization and SGoF correction for multiple comparison indicate significance, and the correlation value is positive. **Neg. corr. significance:** As Pos. corr. significance, but where the correlation value is negative. **Individuals frame shifts:** Frame shifts of each individual rat's maximum mean $r_{\text{lfp-bold-template}}$, relative to the mean of all rats. N=46 for dexmedetomidine, 7 rats, 3-14 runs per rat. N=17 for isoflurane, 4 rats, 2-8 runs per rat.

Anesthesia	Side	Mean	Period estimate	Freq. estimate	Pos. corr. significance	Neg. corr. significance	Individuals' frame shifts
Isoflurane	Left	0.253 ± 0.224	12.25s	0.0816 Hz	-14s to -11.5s and from -2.25s to 1.75s	-8.5s to -4.25s and from 3.75s to 7.75s	0.25s, -0.75s, 0.25s and 2.75s
	Right	0.213 ± 0.206	12.4s	0.0805 Hz	-13.75s to -12.25s and from -2s to 1.5s	-8.25s to -4.5s and from 4.25s to 7.5s	0.25s, -0.5s, -17.5s and 2s
Dexmede-tomidine	Left	0.247 ± 0.257	6.06s	0.165 Hz	-7.75s to -6s, from -1.5s to 1.25s and from 5s to 6s	-4.75s to -17.5s, from 1.75s to -2s and from 7.5s to 4s	0.5s, -1.5s, -12s, 0s, -5.25s, 0s and 0s
	Right	0.302 ± 0.200	6.06s	0.165 Hz	-8.25s to -5.5s, from -1.5s to 1.25s and from 4.75s to 6s	-12.75s to -17.5s, from -4.75s to -11.5s, from 1.75s to -2s and from 7s to 4s	-0.25s, -0.25s, -5.5s, -0.25s, -5.75s, 0s and 0s

160

4.3.6 Correlation between template strength and LFPs

Changes over time in the strength of the fMRI spatiotemporal dynamic templates were also directly related to filtered LFP signals. Generation of an fMRI spatiotemporal dynamic template (from the BOLD signal alone) simultaneously produces a time course of the template's strength over time; an example is shown in Figure 4.12. Pearson correlation ($r_{lfp-template}$) was calculated between the pre-processed and filtered LFP time series and corresponding template strength time courses at time shifts up to 20s in each direction. Resulting correlation values were lower than spatial correlation values ($r_{lfp-template} = 0.150$ for isoflurane, $r_{lfp-template} = 0.0635$ for dexmedetomidine, mean across electrodes, scans, rats), but remained statistically significant ($p \leq 0.0161$, significant at 5% FWER by SGoF). These results are illustrated in Figure 4.13, Figure 4.14 and Table 4.4 for mean $r_{lfp-template}$. These results provide further support for a link between low frequency LFPs and the quasi-periodic BOLD patterns.

_____
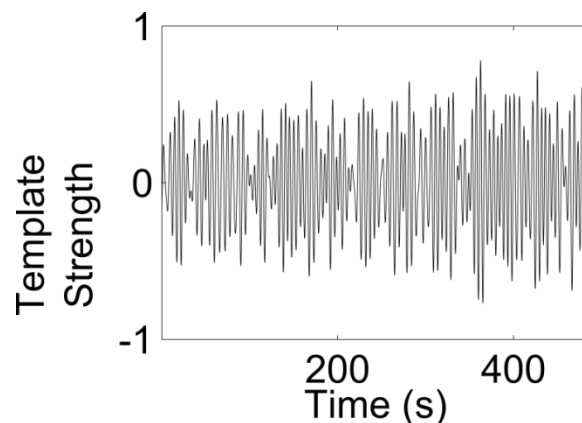
Figure 4.12: Template strength vs. time. In addition to producing a template, the algorithm provided in Majeed, et al. produces a signal versus time of the template's strength. An example of such a time course from one rat is shown in this figure. In the present chapter, this time course was correlated with the filtered infraslow LFP signal to produce $r_{lfp-template}$ (Figure 4.13).

161
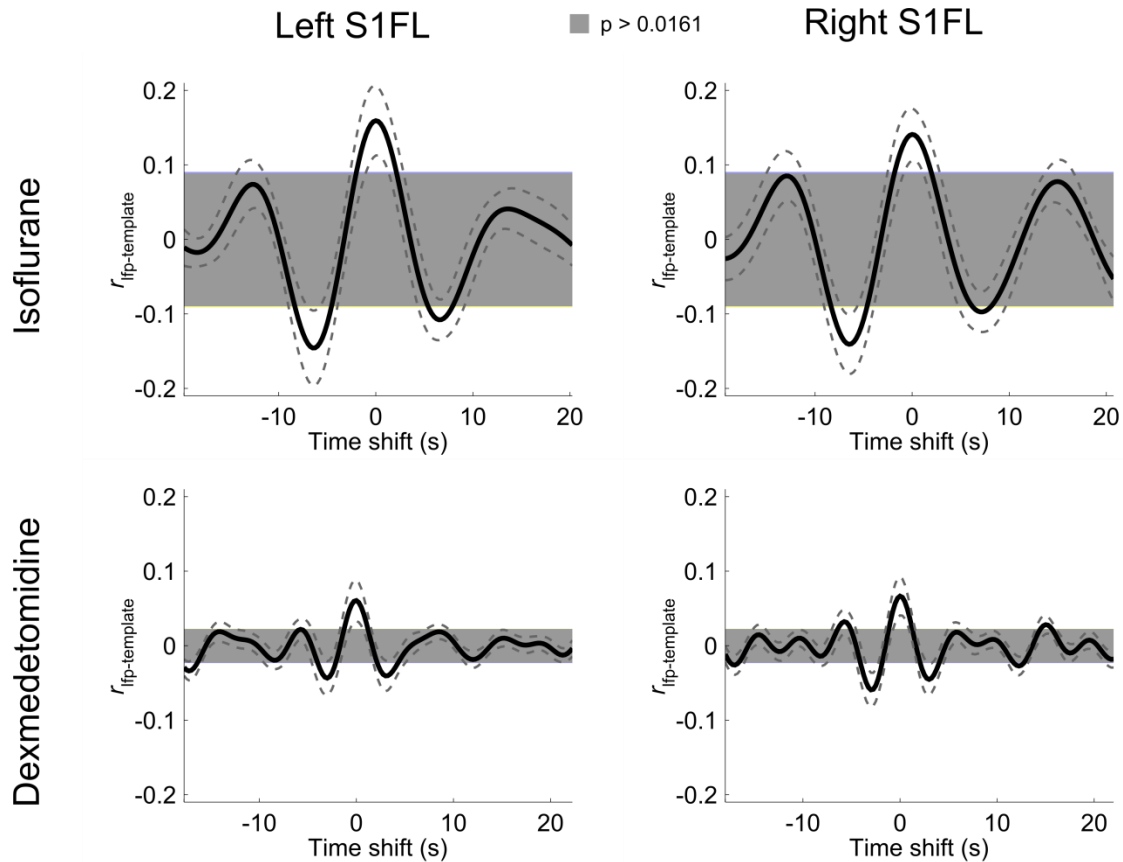
Figure 4.13: $r_{\text{lfp-template}}$. Pearson correlation between template strength and pre-processed infraslow LFP signal, $r_{\text{lfp-template}}$, plotted versus time shift from maximum. Black solid line is mean of all rats and scans, dark gray dashed line is one standard error. Light gray areas are not significant ($p > 0.0161$), other areas are significant (SGoF, 5% FWER). Left column is infraslow LFP from the electrode from left S1FL, right column is right S1FL. Top row is isoflurane anesthesia, bottom row is dexmedetomidine anesthesia. Numerical results are shown in Table 4.4, both electrodes and individual rats are shown in Figure 4.14. In every case, $r_{\text{lfp-template}}$ is significant for the largest peak and approximately resembles a down-scaled autocorrelation series. N=46 for dexmedetomidine, 7 rats, 3-14 runs per rat. N=17 for isoflurane, 4 rats, 2-8 runs per rat.
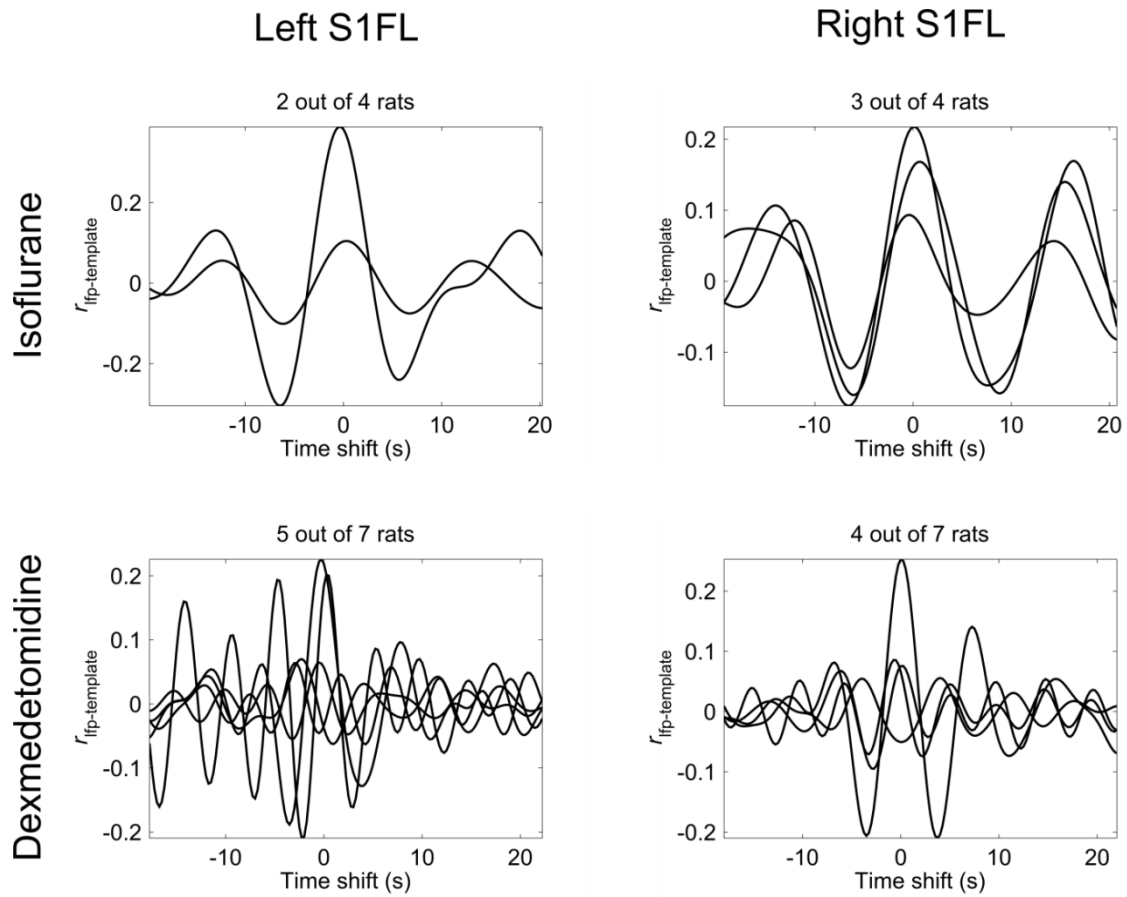
Figure 4.14: As Figure 4.13, except individual $r_{\text{lfp-template}}$ values are plotted for each electrode and rat, for rats that fell within one standard deviation of the mean for frame shift location of maximum value. Note that, unlike Figure 4.11, results are less consistent and cannot be clearly seen on all rats. Each rat represents the mean of 2-14 scans.

Table 4.4: Numerical results for calculation of $r_{\text{lfp-template}}$, the time correlation between the filtered and preprocessed infraslow LFP signal and the changes over time in strength of the fMRI spatiotemporal dynamic generated from BOLD alone. This is from values plotted in Figure 4.13. Each row represents a separate condition for site of electrode implantation (Left or Right) and anesthesia (Isoflurane or Dexmedetomidine. Columns are as follows. **Mean:** Maximum mean $r_{\text{lfp-template}}$, considered to be a time shift of zero. Mean ± one standard deviation. **Period estimate:** Estimated period if it is assumed to be an autocorrelation series. **Freq. estimate:** One divided by the period estimate. **Pos. corr. significance:** Time shifts where data randomization and SGoF correction for multiple comparison indicate significance, and the correlation value is positive. **Neg. corr. significance:** As Pos. corr. significance, but where the correlation value is negative. **Individuals time shifts:** Time shifts of each individual rat's maximum mean $r_{\text{lfp-bold-template}}$, relative to the mean of all rats. N=46 for dexmedetomidine, 7 rats, 3-14 runs per rat. N=17 for isoflurane, 4 rats, 2-8 runs per rat.

Anesthesia	Side	Mean	Period estimate	Freq. estimate	Pos. corr. significance	Neg. corr. significance	Individuals' time shifts
Isoflurane	Left	0.159 ± 0.193	13.1s	0.0766 Hz	-2.25s to 2s	-8.5s to -4.75s and from 5.25s to 7.75s	-0.25s, 0.25s, 12.25s and -13s
	Right	0.141 ± 0.144	13.9s	0.0721 Hz	-2s to 1.75s	-8.5s to -4.75s and from 6.25s to 7.75s	0s, -0.5s, 11.5s and 0.75s
Dexmede-tomidine	Left	0.0605 ± 0.1869	6.56s	0.152 Hz	-1.5s to 1s	-4s to -16.5s and from 2s to -2.25s	-0.25s, -2.25s, 1s, 0.25s, -3s, -0.5s and -6.5s
	Right	0.0665 ± 0.1754	5.88s	0.170 Hz	-6.5s to -5.25s, from -1.25s to 1s and from 14.25s to 15.5s	-17.75s to -16.75s, from -4.25s to -2s, from 2s to 4s and from 11.5s to 12.75s	0s, 4s, -5.75s, -4.75s, 6.5s, -0.75s and 0.25s

Numerical results are summarized in Table 4.4. Every result showed significance for a large central peak and two negative side peaks, and in some cases one or two positive side peaks. This result appeared similar to an autocorrelation series, and the results of estimating it as such are also shown in the table

4.3.7 Use of median instead of mean

The median $r_{\text{lfp--template}}$ was calculated in addition to the mean value. Results are shown in Figure 4.15 and Table 4.5. Every result showed significance for the largest central peak.

_____

Table 4.5: Numerical results for calculation of $r_{\text{lfp-template}}$ using median, but otherwise as in Table 4.4. This is from values plotted in Figure 4.15. Each row represents a separate condition for site of electrode implantation (Left or Right) and anesthesia (Isoflurane or Dexmedetomidine). Columns are as follows. **Median:** Maximum median $r_{\text{lfp-template}}$, considered to be a time shift of zero. **Pos. corr. significance:** Time shifts where SGoF correction for multiple comparison indicate significance, and the correlation value is positive. **Neg. corr. significance:** As pos corr. Significance, but where the correlation value is negative.

Anesthesia	Side	Median	Pos. corr. significance	Neg. corr. significance
Isoflurane	**Left**	0.177	-2s to 1s and from 2.5s to 2.75s	7.75s to -5.5s, from -5.25s to -4.5s, from -4s to -3.75s and from 5.5s to 6.75s
	Right	0.167	14.25s to -14s and from -1.75s to 2.5s	-8.5s to -4.5s and from 6s to 7.5s
Dexmede-tomidine	**Left**	0.0741	-0.75s to 1.75s	-7.5s to -15.5s, from -4s to -7.25s and from -2.75s to -3s
	Right	0.07693	-6.25s to -5.25s, from -1.5s to 1s and from 14.5s to 15.25s	-17.75s to -16.5s, from -8.5s to -8.25s, from -4s to -2s, from2.25s to 3s and from 11.75s to 12s
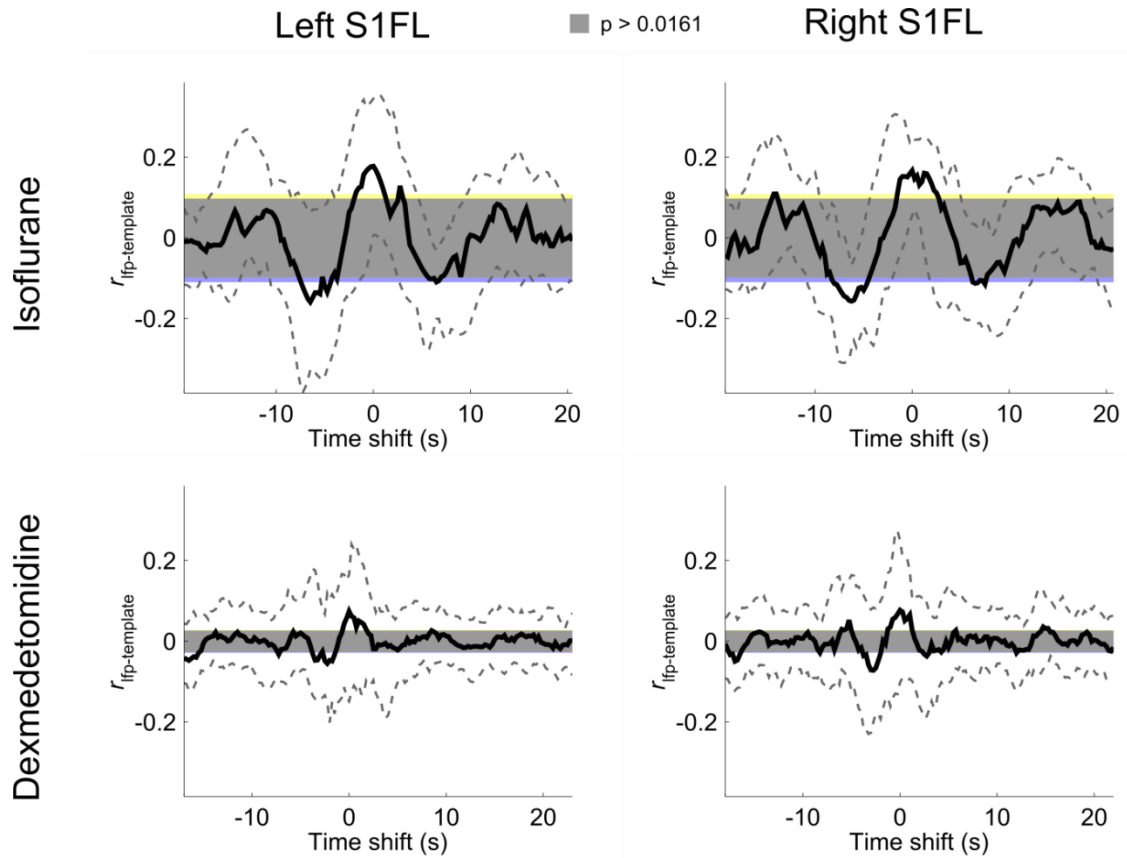
Figure 4.15: Median $r_{\text{lfp-template}}$. Pearson correlation between template strength and pre-processed infraslow LFP signal, $r_{\text{lfp-template}}$, plotted versus time shift from maximum. Black solid line is the median of all rats and scans, the upper dark gray dashed line represents the 84.1$^{\text{st}}$ percentile and the lower dark gray dashed line represents the 15.9$^{\text{th}}$ percentile (equivalent to one standard deviation from a normal distribution). Light gray areas are not significant ($p > 0.0161$), other areas are significant (SGoF, 5% FWER). Left column is infraslow LFP from the electrode from left S1FL, right column is right S1FL. Top row is isoflurane anesthesia, bottom row is dexmedetomidine anesthesia. Despite using the median instead of mean, significant results are similar to Figure 4.13. Numerical results are shown in Table 4.5. N=46 for dexmedetomidine, 7 rats, 3-14 runs per rat. N=17 for isoflurane, 4 rats, 2-8 runs per rat.

166

4.3.8 Test of preliminary caudate-putamen electrical recording

Calculating $r_{\text{lfp-bold}}$, using an electrode implanted in the caudate-putamen and BOLD regions of interest in the caudate-putamen, resulted in a dynamic propagating from ventral to dorsal caudate-putamen, most visible in the contralateral side (Figure 4.16b). Using regions of interest in interhemispheric caudate-putamen to calculate an fMRI spatiotemporal dynamic template also resulted in visible propagation of high signal from ventral to dorsal caudate-putamen (Figure 4.16a). Calculation of $r_{\text{lfp-bold-template}}$, spatial correlation between the two patterns at every frame shift, did not result in an autocorrelation-like series, though it did result in several peaks of comparatively high correlation, $r_{\text{lfp-bold-template}} > 0.3$ (Figure 4.16c). As some rats had $r_{\text{lfp-bold-template}}$ similar to this (Figure 4.11), it is possible that by using more scans and rats, that this would appear more like an autocorrelation series. It is also possible that an empirical filter generated from the caudate-putamen region instead of the S1FL region would make this result more consistent with what was observed in S1FL.

4.3.9 Power spectrum of template strength versus time

Power spectra were calculated for the template strength time courses (based on correlation with the template in a sliding window). Under isoflurane a single peak was observed at approximately 0.0713 Hz or 14.0 s and under dexmedetomidine two peaks were observed approximately 0.151 Hz or 6.62s s and 0.209 Hz or 4.78 s. These frequencies are consistent with the period of the fMRI spatiotemporal dynamics calculated from considering $r_{\text{lfp-bold-template}}$ and $r_{\text{lfp-template}}$ to be auto-correlation spectra

167

(shown on Table 4.3 and Table 4.4), further strengthening the link between infraslow LFP and these templates. The spectra are shown in Figure 4.17.

4.3.10 Incorrectly paired scans from the same rat

Observation of the correlation between incorrectly matched BOLD and LFP data from the same rat did show an artifactual dynamic at an arbitrary time shift, shown in Figure 4.18. The artifactual dynamic had lower correlation than other examples shown in this manuscript (Figures 4.8 and 4.9) but did follow a similar pattern. This likely occurred due to the fact that the spatiotemporal dynamics are quasi-periodic, so aligning an LFP trace where the dynamic is occurring coincidentally with a BOLD trace where the dynamic is occurring will result in a moderately correlated artifactual dynamic. This supports the quasi-periodic nature of the LFP and BOLD correlations.

168
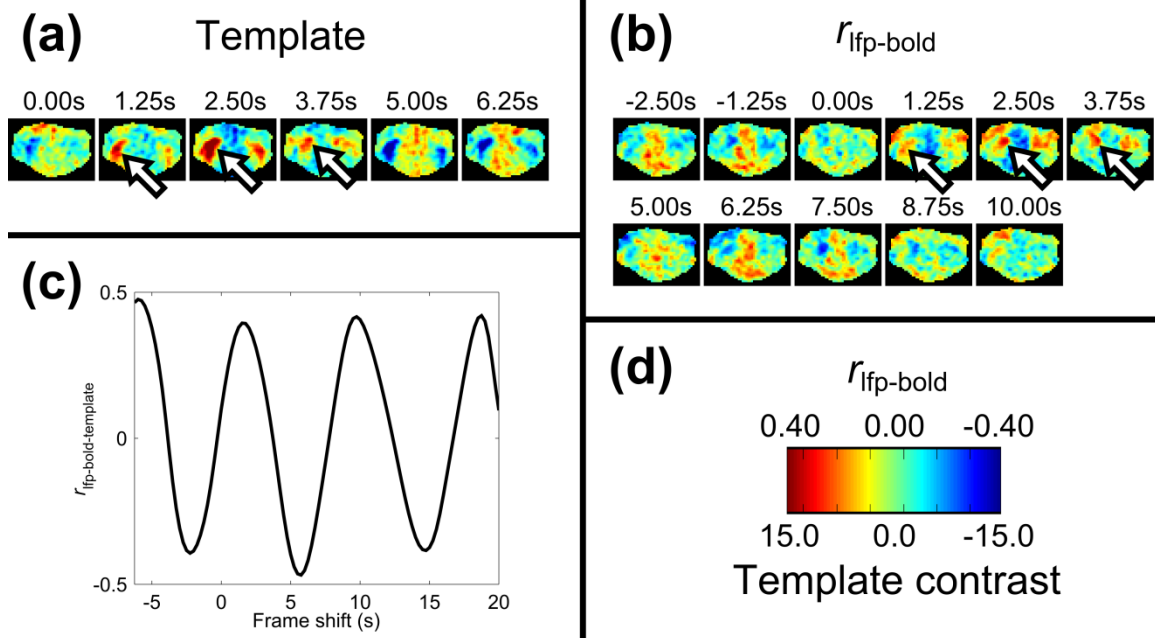
Figure 4.16: Caudate-putamen results. **(a)** fMRI spatiotemporal dynamic template generated from BOLD signal alone, using regions of interest in left and right caudate-putamen. Arrows indicate the ventral to dorsal propagation on the side contralateral to the electrode (note it is visible on the ipsilateral side as well). **(b)** Cross-correlation $r_{lfp\text{-}bold}$ between an infraslow LFP signal and the BOLD signal in the caudate-putamen. Arrows indicate the ventral to dorsal propagation on the side contralateral to the electrode (note it is visible on the ipsilateral side as well). **(c)** Spatial correlation $r_{lfp\text{-}bold\text{-}template}$ between $r_{lfp\text{-}bold}$ from (b) and the template from (a). **(d)** Scale bar for (a) and (b). Parts (a) and (b) are included as movie files in section 4.4. N=1.
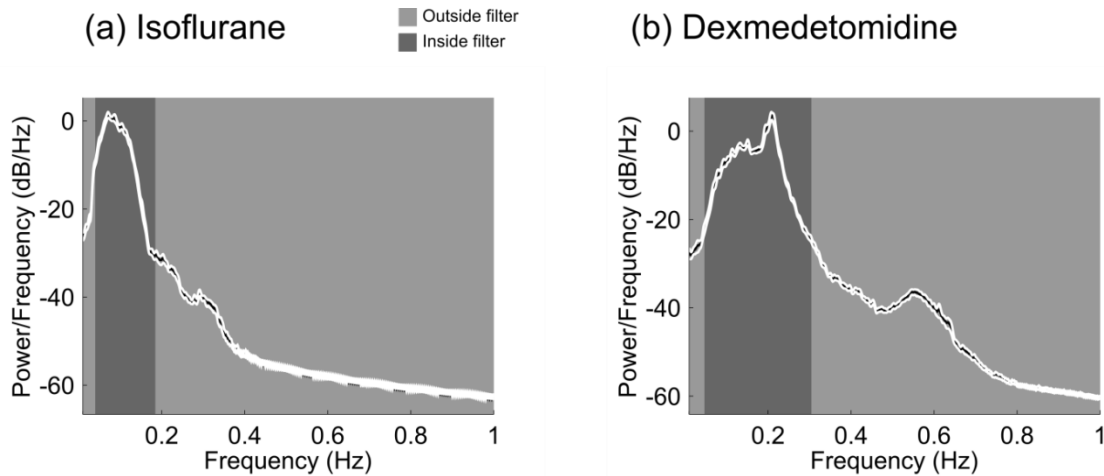
Figure 4.17: Template power spectra. Dark gray areas are areas inside the empirical filter for the respective anesthesias, light gray areas are areas outside the empirical filter. The black line with white edges is the mean. (a) Power spectra of the template strength versus time (based on correlation in a sliding window) under isoflurane anesthesia. The peak within the filter is located at approximately 0.0713 Hz or 14.0 s. (b) As (a), except dexmedetomidine anesthesia. The peaks within the filter are located at approximately 0.151 Hz or 6.62s s and 0.209 Hz or 4.78 s.

_____
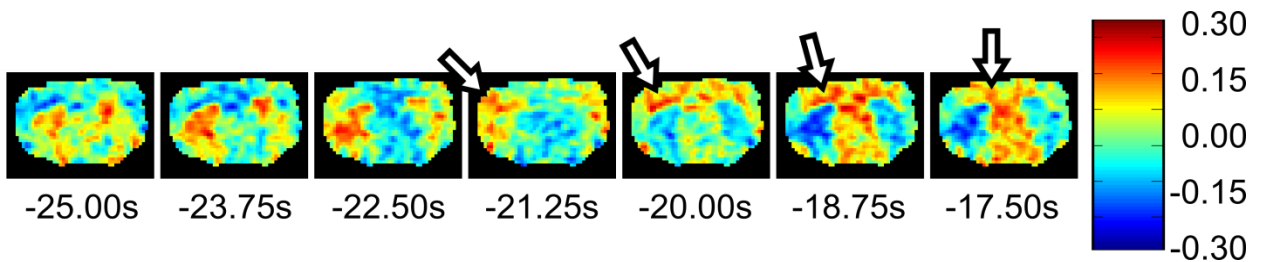
Figure 4.18: Incorrect matching. $r_{\text{lfp-bold}}$ calculated between incorrectly matched LFP and BOLD data from the same rat. Note that a lower-correlation spatiotemporal dynamic can still be observed at some arbitrary time shift between the two signals.

170

4.4 Movies of $r_{\text{lfp-bold}}$ and fMRI spatiotemporal dynamic templates

There are five movies linked here, each illustrating $r_{\text{lfp-bold}}$ generated from LFP-BOLD correlation, followed by the corresponding fMRI spatiotemporal dynamic template generated from BOLD alone. For the common direction of propagation (ventral-lateral to dorsal-medial along the cortex) two examples are shown per anesthesia, for the rare opposite direction, only one example is shown per anesthesia. All movies are in QuickTime (*.mov) format.

4.4.1 Ventral-lateral to dorsal-medial cortical propagation (>50% of all cases)

In more than half of all cases, propagation was observed from the ventral-lateral cortex to the dorsal-medial cortex (Table 4.2). This observation was seen in both $r_{\text{lfp-bold}}$ and the corresponding fMRI spatiotemporal dynamic templates.

Figure 4.19: Common direction cortical propagation under isoflurane (isoflurane_up_movie.mov, 1,327K). The first and third segments presented in this movie file are Pearson correlation, $r_{\text{lfp-bold}}$ between the LFP signal and BOLD, shown in every voxel of BOLD at time shifts from -3s to 10s. The second and fourth segments presented in this movie file are spatiotemporal dynamic templates, generated using the Majeed et al. algorithm from the BOLD signal alone, shown at every frame. The first and second segments presented in this movie file correspond to figure 4.9 in the manuscript. These data are recorded under isoflurane anesthesia from an electrode placed in the left (first segment) and right (third segment) S1FL and with the seeds for the Majeed, et al. algorithm placed in interhemispheric S1FL.

Figure 4.20: Common direction cortical propagation under dexmedetomidine (dexmedetomidine_up_movie.mov, 1,158K). The first and third segments presented in this movie file are Pearson correlation, $r_{\text{lfp-bold}}$ between the LFP signal and BOLD, shown in every voxel of BOLD at time shifts from -3s to 10s. The second and fourth segments presented in this movie file are spatiotemporal dynamic templates, generated using the Majeed et al. algorithm from the BOLD signal alone, shown at every frame. The first and second segments presented in this movie file correspond to figure 4.9 in the manuscript. These data are recorded under dexmedetomidine anesthesia from an electrode placed in the left S1FL and with the seeds for the Majeed, et al. algorithm placed in interhemispheric S1FL.

4.4.2 Dorsal-medial to ventral-lateral cortical propagation (~10% of all cases)

In less than 10% of all cases, propagation in the opposite direction (dorsal-medial to ventral-lateral cortex) was observed (Table 4.2). This was observed under $r_{\text{lfp-bold}}$ but, unlike the other direction, it was not usually observed in the corresponding fMRI spatiotemporal dynamic templates.

Figure 4.21: Rare direction cortical propagation under isoflurane (isoflurane_down_movie.mov, 669K). The first segment presented in this movie file is Pearson correlation, $r_{\text{lfp-bold}}$ between the LFP signal and BOLD, shown in every voxel of BOLD at time shifts from -3s to 10s. The second segment presented in this movie file is the spatiotemporal dynamic template, generated using the Majeed et al. algorithm from the BOLD signal alone, shown at every frame. These data are recorded under isoflurane

172

anesthesia from an electrode placed in the right S1FL and with the seeds for the Majeed, et al. algorithm placed in interhemispheric S1FL.

Figure 4.22: Rare direction cortical propagation under dexmedetomidine (dexmedetomidine_down_movie.mov, 570K). The first segment presented in this movie file is Pearson correlation, $r_{\text{lfp-bold}}$ between the LFP signal and BOLD, shown in every voxel of BOLD at time shifts from -3s to 10s. The second segment presented in this movie file is the spatiotemporal dynamic template, generated using the Majeed et al. algorithm from the BOLD signal alone, shown at every frame. These data are recorded under dexmedetomidine anesthesia from an electrode placed in the left S1FL and with the seeds for the Majeed, et al. algorithm placed in interhemispheric S1FL.

4.4.3 Caudate-putamen propagation

Using preliminary data from an electrode implanted in the caudate-putamen, data analysis was repeated and ventral to dorsal propagation was again observed under both $r_{\text{lfp-bold}}$ and the corresponding fMRI spatiotemporal dynamic template.

Figure 4.23: Caudate-putamen propagation under dexmedetomidine (caudate_putamen_movie.mov, 535K). The first segment presented in this movie file is Pearson correlation, $r_{\text{lfp-bold}}$ between the LFP signal and BOLD, shown in every voxel of BOLD at time shifts from -3s to 10s. The second segment presented in this movie file is the spatiotemporal dynamic template, generated using the Majeed et al. algorithm from the BOLD signal alone, shown at every frame. These data are recorded under dexmedetomidine anesthesia from an electrode placed in the right caudate-putamen and

173

with the seeds for the Majeed, et al. algorithm placed in interhemispheric caudate-putamen. This movie corresponds to Figure 4.16.

4.5 Discussion

The present chapter suggests that the previously observed fMRI spatiotemporal dynamics (Majeed, Magnuson et al. 2009; Majeed, Magnuson et al. 2011) and the low-frequency local field potentials that correlate with fMRI (Pan, Thompson et al. 2013) share a common mechanism. Significant correlation has been demonstrated between the spatial extent and timing of fMRI spatiotemporal dynamic templates generated from the BOLD alone and the spatial extent and timing of infraslow LFP-BOLD correlation (Figure 4.10). Both the BOLD-based templates and infraslow LFP-BOLD correlation patterns are different in spatial extent and timing under the two anesthetics, but the correlation between them remains strong. Furthermore, the changes over time in the strength of the fMRI spatiotemporal dynamics (generated from BOLD alone) and the changes over time of the infraslow LFP signal (Figure 4.13) show a significant relationship. This study focuses on the S1FL region; preliminary data is also shown that suggests that these results will translate to another brain region (the caudate-putamen, Figure 4.16).

The implication is that the fMRI spatiotemporal dynamics observed in the spontaneous BOLD signal (Majeed, Magnuson et al. 2009; Majeed, Magnuson et al. 2011) reflect a quasi-periodic, slow wave of electrical potential changes that make up a significant portion of the infraslow LFP. The observed significant correlation resembles

174

autocorrelation of a signal containing a single periodic process (Figure 4.10). When considered to be such, the observed period of this autocorrelation matches the period of the fMRI spatiotemporal dynamics themselves (see section 4.3.9).

4.5.1 Possible common mechanisms for fMRI spatiotemporal dynamics and LFP-BOLD correlations

As LFP were recorded only from a single point in each hemisphere, it is possible that the appearance of propagation in both the BOLD-based fMRI spatiotemporal dynamic templates and the infraslow LFP-BOLD correlation maps is vascular in origin. Large veins point downward into the rat cortex (Lin, Lin et al. 2009), and arteries point upward, dorsal-medially. A change in blood flow can create a change in arterial diameter; the time scale of this change is on the order of seconds for distances on the order of millimeters (Porret, Stergiopulos et al. 1998). The correlation with field potentials could be synchrony between this highly coordinated vasomotion and large scale slow fluctuations in the brain, such as occasional global sleep waves (Steriade, Contreras et al. 1993; Steriade, Nunez et al. 1993; Steriade, Nunez et al. 1993) or a hypothetical global neural electrical signal (Scholvinck, Maier et al. 2010).

Neural and glial mechanisms could also allow for slow, propagating changes in the electrical field. Thalamocortical neurons may initiate slow wave activity through calcium ions (Hughes, Cope et al. 2002) and this neural activation may increase astrocytic calcium concentrations, inducing a wave that can propagate to other astrocytes on a scale of tens of seconds (Kuga, Sasaki et al. 2011). The interplay between the blood

175

vessel directionality described above and changing intracellular calcium concentrations that cause local vessel dilation (Iadecola and Nedergaard 2007; Girouard, Bonev et al. 2010), or astrocytic dynamics (Kuga, Sasaki et al. 2011) may tentatively explain the direction of the dynamics observed here.

To test which of these hypotheses is more likely, the infraslow LFP at multiple sites along the pattern of propagation would need to be recorded. However in either case, the dynamics are likely linked to information processing as they would be relating to either a global signal with an electrical basis (Scholvinck, Maier et al. 2010) or localized dynamics such as those previously linked to behavior in fMRI (Eichele, Debener et al. 2008; Thompson, Magnuson et al. 2012). Single unit recording may help confirm if the electrical basis is actually neural (as would be initially suspected) or has a more complex source, such as astrocytes or other glia.

4.5.2 Implications for dynamic analysis of functional connectivity.

While fMRI-based functional connectivity is typically calculated for an entire resting state scan (5-10 minutes), interest is growing in identifying changes that occur on much shorter time scales (12-100 seconds) (Chang and Glover 2010; Hutchison, Womelsdorf et al. 2012; Thompson, Magnuson et al. 2012). However, preliminary attempts using correlation calculated in sliding time windows have had mixed results as the signal dynamics in some cases appear indistinguishable from randomly-matched or artificial data (Handwerker, Roopchansingh et al. 2012; Keilholz, Magnuson et al. 2012). Chapter 2 demonstrated a consistent link between correlation in sliding windows and

176

behavior by focusing on the networks where fMRI spatiotemporal dynamics have been observed in humans (Thompson, Magnuson et al. 2012). This suggests that infraslow activity could be used to identify meaningful changes in sliding window correlation.

The results of this study also highlight some of the pitfalls involved in standard functional connectivity analysis techniques. No correlation is typically observed between lateral and medial cortical areas in the rat (Zhao, Zhao et al. 2008; Pawela, Biswal et al. 2009; Williams, Magnuson et al. 2010), but the present chapter suggests this may be due to a time lag resulting from a propagating dynamic. Perhaps the entire somatomotor cortex could be considered a network, with sub-networks connecting interhemispherically homologous areas. It is interesting to speculate, based on the pattern of fMRI spatiotemporal dynamics in humans, that the default and attention networks are also part of a larger organization.

4.5.3 Limitations of the study

The fMRI spatiotemporal dynamics that were observed in this chapter are unlikely to be artifactual in origin. Previous work using fast imaging (10Hz) has shown that these dynamics are not related to aliasing of cardiac or respiratory frequency components, nor are they related to scanner noise as they do not occur in euthanatized rats under the same setup (Majeed, Magnuson et al. 2009) and occur in both humans and rats, under different scan parameters for both species (Majeed, Magnuson et al. 2011). It is unlikely that they are due to local differences in signal to noise ratio because they propagate in both directions, primarily in the direction towards the electrode, the opposite

177

of the direction proposed for this artifact by Logothetis et al. (Logothetis, Murayama et al. 2009). Animals were imaged in the dark, under anesthesia, and typical forepaw stimulation equipment was not attached, so stimulus artifacts can be excluded.

The results presented in this chapter are consistent between the two anesthetics except for the time scales; this may be because the filters are based on the different infraslow LFP-BOLD coherence between anesthesia. Previously published work indicated that use of the coherent frequencies produced the best results, with outside frequencies (such as those for another anesthetic) were unlikely to influence results except to increase noise (Pan, Thompson et al. 2013). However, as vascular properties themselves may limit which frequencies in the infraslow LFP can be represented by BOLD, the empirical filters may be representing the differing vascular effects of the two anesthetics (Iida, Ohata et al. 1998; Ohata, Iida et al. 1999). Nevertheless, the use of two anesthetics with different mechanisms (see Appendix) and different effects on the vasculature demonstrates these results are not an artifact of any single anesthesia.

It also must be considered that the present chapter used regression of the mean signal from all brain voxels to reduce the noise due to non-localized scanner artifacts (Fox, Snyder et al. 2005). This was required to complete the goal of this study as previous work both with infraslow potentials (Pan, Thompson et al. 2013) and with fMRI spatiotemporal dynamics (Majeed, Magnuson et al. 2009; Majeed, Magnuson et al. 2011) performed this regression, and this study combined those studies. In addition, in the anesthetized rat model, failure to regress this "global signal" can complicate comparison between different anesthesia levels (Liu, Zhu et al. 2012). However, global signal

www.manaraa.com

regression has the potential to introduce artifactual anti-correlation (Gavrilescu, Shaw et al. 2002) even if it may not do so in practice (Fox, Zhang et al. 2009). Further work is needed to determine if the negative correlations observed here are actually physiologically "negative", or merely low relative to some form of global electrical signal (Scholvinck, Maier et al. 2010).

4.5.4 Conclusion

As fMRI spatiotemporal dynamics have also been demonstrated during the resting state in human subjects (Majeed, Magnuson et al. 2011), the results of this study have many implications for human resting state studies. Local field potentials are an aggregate, extracellular measure like EEG (Buzsaki, Anastassiou et al. 2012), which has also been studied at frequencies under 1Hz (Khader, Schicke et al. 2008). Therefore potential applications could include use of infraslow EEG to map functional networks or, conversely, use of fMRI spatiotemporal dynamics to better understand slow EEG potentials. As the fMRI spatiotemporal dynamics are linked to neural electrical oscillations, it is possible that they are related to problems in network modulation for diseases linked to functional connectivity. Analysis that includes fMRI spatiotemporal dynamics may help in understanding why some diseases, such as Schizophrenia, show both increases and decreases in functional connectivity (Garrity, Pearlson et al. 2007).

However, it is hoped that the existence of an infraslow, electrically-correlated, fMRI-observable and easily replicable dynamic within the resting state BOLD signal will provide researchers with a solid target for investigating the ultimate origin of both

179

healthy and disrupted resting state functional networks in the brain. Such a target may one day allow both the neuronal and non-neuronal basis of resting state functional networks to finally be understood.

CHAPTER 5

CONCLUSION

As described in Chapter 1, functional connectivity and resting state methods for fMRI data analysis have proven effective in diagnosing neuropsychiatric diseases and predicting behavioral differences between groups of healthy individuals. However the long time scales used in analysis (6-8 minutes) made it difficult to get a better understanding of how the correlated fluctuations are emerging, and complicated efforts to understand the neural or glial activity and physiology behind them. Therefore, while interesting, functional connectivity methods were poorly understood (Raichle 2006) and sometimes argued to be artifacts of pre-processing methods (Gavrilescu, Shaw et al. 2002).

Dynamic analysis of the resting state signal, done in its earliest forms with quasi-periodic pattern detection by Majeed et al., 2009 (Majeed, Magnuson et al. 2009) and sliding-window correlation by Chang and Glover, 2010 (Chang and Glover 2010) shows promise as a method of understanding the correlations in functional networks by understanding the fluctuations underlying them.

Chapter 2 provides evidence linking dynamically measured functional connectivity to a behavioral result that directly matches what was observed when using static functional connectivity. Both entire resting state scans and 12.3 second windows at various peristimulus times around a task show a relationship between anti-correlation between two networks and better (faster) performance on a vigilance task. This result also

181

replicates entire-scan results seen for similar tasks in the past (Kelly, Uddin et al. 2008). Chapter 2 also shows, by examining intra-individual variation (Figure 2.6), a time dependence of the effect on behavior. This provides solid evidence that the dynamics within resting state fMRI are likely to be linked to the overall results seen when comparing resting state fMRI to behavior. This suggests that functional networks, calculated over entire scans, may represent an average of dynamic spontaneous activity, and can be understood by understanding these dynamics.

As the dynamics are linked to behavior, they likely have a neural basis, so the next step taken was towards understanding this basis. Chapter 3 showed that higher frequency (in particular beta and gamma band) electrical activity in the brain is linked to changes in interhemispheric correlation over time at a specific location versus its contralateral homologue. Chapter 4 showed that low-frequency electrical activity in the brain was linked to a quasi-periodic pattern in fMRI that appeared as a propagating wave, as has been observed previously in fMRI-only studies (Majeed, Magnuson et al. 2009; Magnuson, Majeed et al. 2010; Majeed, Magnuson et al. 2011). The relationship between the quasi-periodic patterns and localized interhemispheric correlation thus becomes an interesting topic worthy of future investigation. At least part of interhemispheric correlation must make up the quasi-periodic patterns, as they typically show bilateral symmetry. However, as the two different ways of measuring dynamics correlate with different LFP components, they may be representing different underlying processes in the brain. Future work can try to separate these different sources' effects on functional connectivity, as well as differentiate how each method of measuring dynamics is affected wholly or in part by the different components of the LFP.

182

What about the other permutations, sliding window correlation versus infraslow activity, and quasi-periodic patterns versus high frequency BLP? BOLD changes in interhemispheric correlation in 50s windows were not strongly linked to low-frequency electrical activity changes in interhemispheric correlation (Figure 3.9), showing only marginally significant correlation under one of four cases. Quasi-periodic patterns versus high-frequency BLP was not investigated herein due to two factors that made the comparison difficult. First, unlike the infraslow LFP (Figure 4.9), BLP does not exhibit an obvious dynamic pattern when correlated with the fMRI signal at multiple time shifts. See Figure 6 of Pan et al. for an example (Pan, Thompson et al. 2011); a similar result was also observed across every rat examined (personal communication with Wen-Ju Pan, 2011). Second, again unlike the infraslow LFP (Figure 4.5), the coherence measured between BLP and fMRI was much lower, and under dexmedetomidine lacked obvious peaks. This is illustrated in Pan et al., 2013, Figure 4 (Pan, Thompson et al. 2013). While these results do not preclude measuring quasi-periodic patterns in some manner in fMRI and comparing them to BLP, it does make replicating the steps in Chapter 4 with BLP troublesome, and makes it appear unlikely to produce positive results. Therefore this was not examined for this dissertation. However, the above mentioned data limitations do suggest that we should hypothesize either that no relationship, or a much weaker relationship than with the infraslow LFP, exists.

It has long been hypothesized in neuroscience that high frequencies coordinate localized (or contralateral homologous through the corpus callosum) regions of the brain, while low frequencies coordinate larger scale activity. The results presented in Chapter 3 and Chapter 4 support this view in linking the spontaneous activity observed in fMRI to

the LFP recorded directly from the brain. The high frequencies of gamma and beta, as well as the gamma-linked theta band (Tort, Komorowski et al. 2010), show changes in correlation that match those in the fMRI signal local to the electrode. The infraslow electrical signal, conversely, correlates with a broad, quasi-periodic pattern across the entire brain.

Future work with new techniques may be able to examine even shorter time scales of neural activity as compared to fMRI. While this work has compared power changes in LFP to the BOLD signal, limitations of the fMRI scanner prevented direct comparison to amplitudes of the LFP signal above 1Hz. However, new fMRI technologies, such as stronger magnets (Yacoub, Shmuel et al. 2001), and new pulse sequences, such as ultra-fast fMRI (Feinberg and Setsompop 2013), may allow direct comparison of BOLD amplitude changes to the slower LFP bands such as delta and alpha. It is also theoretically possible to use the same setup done for simultaneous LFP/fMRI to perform simultaneous patch-clamp/fMRI. This would be difficult due to the comparatively short time from which it is possible to record from a single neuron (<1 hour) versus an LFP electrodes in extracellular fluid (>4 hours). One possible solution would be to build a system for automatically patching onto cells entirely out of MRI-safe materials and perform the patching inside the scanner itself.

Another possible future study would be to look at direct correlation between LFP or BLP versus BOLD in short, sliding windows, rather than correlating within each modality prior to correlating across modalities (as was done in Chapter 3). Positive results of such a study would be difficult to interpret; Chapter 3 can be interpreted as

184

networks in the LFP being represented in the BOLD, whereas positive results for the other kind of study would have to represent some kind of dynamic change in the hemodynamic response to electrical activity. Nevertheless, since we already have usable data from Chapter 3, this would be a comparatively easy and interesting study for someone to complete in the future.

The interplay between large scale and local disruptions in functional connectivity are not well understood, particularly in how this interplay relates to the behavioral differences and disease states described in Chapter 1. Majeed, et al.'s quasi-periodic patterns (Majeed, Magnuson et al. 2009) and Chang and Glover's sliding window correlation (Chang and Glover 2010) provide two dynamic analysis methods that can be used in this investigation. The work presented in this dissertation first shows that such methods are useful in Chapter 2, and then provides insight into what neural electrical activity underlies these techniques in Chapter 3 and Chapter 4.

Continuation of this work is necessary to answer many questions; Does the propagating wave seen in Chapter 4 exist as a propagating electrical potential or is it hemodynamic and merely coordinated by a global electrical signal? What are the cortical or subcortical drivers behind functional connectivity? What are the neural, astrocytic or venous mechanisms for propagation of functional connectivity across the brain? It also remains an open question how the two types of dynamics interact. While quasi-periodic patterns appear more linked to infraslow neural or glial activity than sliding window correlation, the dynamics are often interhemispheric and thus would be expected to induce some correlation on short time scales. Possibly, this induced effect could be

185

removed from the BOLD signal to get local dynamic correlation alone which may produce a better fMRI biomarker for higher frequency neural electrical activity. Despite these questions, this work provides solid evidence of an electrophysiological (that is hypothetically neural, but possibly glial as well) origin for the dynamics seen in resting state fMRI, and initial insight into the source of these dynamics. Researchers who use the tools of sliding-window correlation and quasi-periodic pattern analysis can use this work to gain an insight into the neural basis of the changes in functional connectivity that they are observing.

By understanding how functional connectivity measured with fMRI originates, we can better understand the diseases in which it is disrupted. As most neuropsychiatric diseases that are poorly understood involve problems in many brain areas, it is not unreasonable to suspect that they may be diseases of coordination or connectivity. Understanding the dynamics that underlie functional connectivity may help scientists understand why diseases such as Schizophrenia show both increased and decreased correlation in functional networks (Garrity, Pearlson et al. 2007). As attention deficit disorders show disruptions in infraslow EEG (Helps, Broyd et al. 2010), linking fMRI dynamics to infraslow potentials may help scientists better spatially localize these disruptions. Therefore, to better treat or even potentially cure diseases such as schizophrenia and attention deficit disorder, it is likely necessary to understand functional connectivity on a much deeper level. This dissertation has taken the first steps in that direction.

APPENDIX

Anesthesia mechanisms and physiological effects

Isoflurane is a gaseous anesthesia with a long history of use in both human patients and nonhuman animal research. Its primary mechanism of anesthesia is not fully understood, but is thought to be suppression of neural activity through inhibition of GABA and glutamate receptors at thalamocortical connections (Alkire, Haier et al. 2000), resulting in a burst pattern in cortical LFP where greater anesthetic dose results in greater burst suppression (Vincent, Patel et al. 2007; Pan, Thompson et al. 2011). Large-scale vascular dilation has been long observed under isoflurane (Reiz, Balfors et al. 1983) which has been suggested to be due to blockage of adenosine triphosphate sensitive potassium (KATP) channels in smooth muscle (Cason, Shubayev et al. 1994). This vascular dilation likely influences the hemodynamic response seen in fMRI (Liu, Zhu et al. 2010; Pan, Thompson et al. 2011). The vasodilation (Schwinn, McIntyre et al. 1990; Lennon and Murray 1995) mechanisms of isoflurane are believed to be independent of alpha adrenergic systems, and the author was unable to find discussion of adrenergic systems in work describing isoflurane's mechanisms of cortical suppression (Ries and Puil 1999; Alkire, Haier et al. 2000). While adrenergic systems may play a role in analgesic properties of isoflurane (Kingery, Agashe et al. 2002), to the best of the author's knowledge these have only been implicated outside the brain.

Medetomidine and its enantiomer dexmedetomidine is an anesthesia that has recently been gaining popularity for small animal fMRI studies as it can be administered

187

subcutaneously to freely breathing animals (Pawela, Biswal et al. 2009). Medetomidine binds in a highly specific fashion to alpha-2 adrenoreceptors. Blockage of these receptors in the central nervous system prevents release of norepinephrine, and as norepinephrine is required for awake behaviors, sedation occurs (Sinclair 2003). As medetomidine requires a sedative effect to maintain anesthesia, its effect is not as strong as isoflurane; stress may prevent sedation, and sedated animals may awaken if disturbed by a loud noise, pain or physical movement (Sinclair 2003). Opposite to isoflurane, medetomidine has been shown to induce vasoconstriction in the cerebral vasculature, which is likely due to the direct effect of alpha-2 receptors within cerebral vasculature (Ganjoo, Farber et al. 1998).

As the two anesthetic agents, first, have hypothetically non-overlapping mechanisms for both their anesthetic and vascular active properties, second, have different effects on vasculature, and third, have vastly different strength, it is suggested in Chapter 4 that each one acts as a control for many possible anesthetic effects against the other. In fact, it has been suggested to use dexmedetomidine to reverse the vascular effects of isoflurane (Zornow, Fleischer et al. 1990) and isoflurane to reverse epileptiform effects of dexmedetomidine overdose (Fukuda, Vazquez et al. 2012). While comparing results under both anesthesias cannot control against the anesthetic state in general, commonalities observed between them are unlikely to be due to the peculiarities of any one anesthesia.

188

REFERENCES

Agranovskii, A. V., O. Berg, et al. (1998). "[Experimental evaluation of materials for electrodes in transcutaneous recording of bioelectric signals]." Med Tekh(1): 23-27.

Albert, N. B., E. M. Robertson, et al. (2009). "The resting human brain and motor learning." Curr Biol 19(12): 1023-1027.

Alkire, M. T., R. J. Haier, et al. (2000). "Toward a unified theory of narcosis: brain imaging evidence for a thalamocortical switch as the neurophysiologic basis of anesthetic-induced unconsciousness." Conscious Cogn 9(3): 370-386.

Allen, E. A., E. Damaraju, et al. (2012). "Tracking Whole-Brain Connectivity Dynamics in the Resting State." Cereb Cortex.

Allen, P. J., O. Josephs, et al. (2000). "A method for removing imaging artifact from continuous EEG recorded during functional MRI." Neuroimage 12(2): 230-239.

Birbaumer, N., T. Elbert, et al. (1990). "Slow potentials of the cerebral cortex and behavior." Physiol Rev 70(1): 1-41.

Biswal, B., F. Z. Yetkin, et al. (1995). "Functional connectivity in the motor cortex of resting human brain using echo-planar MRI." Magn Reson Med 34(4): 537-541.

Boly, M., C. Phillips, et al. (2008). "Consciousness and cerebral baseline activity fluctuations." Hum Brain Mapp 29(7): 868-874.

Brett, M., Anton, J, Valabregue, R, Poline, J (2002). <u>Region of interest analysis using an SPM toolbox</u>. 8th International Conference on Functional Mapping of the Human Brain, Sendai, Japan, NeuroImage.

Buzsaki, G., C. A. Anastassiou, et al. (2012). "The origin of extracellular fields and currents--EEG, ECoG, LFP and spikes." <u>Nat Rev Neurosci</u> 13(6): 407-420.

Calhoun, V. D., T. Adali, et al. (2001). "Spatial and temporal independent component analysis of functional MRI data containing a pair of task-related waveforms." <u>Hum Brain Mapp</u> 13(1): 43-53.

Canolty, R. T. and R. T. Knight (2010). "The functional role of cross-frequency coupling." <u>Trends Cogn Sci</u> 14(11): 506-515.

Carter, A. R., S. V. Astafiev, et al. (2010). "Resting interhemispheric functional magnetic resonance imaging connectivity predicts performance after stroke." <u>Ann Neurol</u> 67(3): 365-375.

Carvajal-Rodriguez, A., J. de Una-Alvarez, et al. (2009). "A new multitest correction (SGoF) that increases its statistical power when increasing the number of tests." <u>BMC Bioinformatics</u> 10: 209.

Cason, B. A., I. Shubayev, et al. (1994). "Blockade of adenosine triphosphate-sensitive potassium channels eliminates isoflurane-induced coronary artery vasodilation." <u>Anesthesiology</u> 81(5): 1245-1255; discussion 1227A-1228A.

Chang, C. and G. H. Glover (2010). "Time-frequency dynamics of resting-state brain connectivity measured with fMRI." <u>Neuroimage</u> 50(1): 81-98.

190

Chang, C., Z. Liu, et al. (2013). "EEG correlates of time-varying BOLD functional connectivity." Neuroimage 72: 227-236.

Chee, M. W., J. C. Tan, et al. (2008). "Lapsing during sleep deprivation is associated with distributed changes in brain activation." J Neurosci 28(21): 5519-5528.

Cordes, D., V. Haughton, et al. (2002). "Hierarchical clustering to measure connectivity in fMRI resting-state data." Magn Reson Imaging 20(4): 305-317.

Cordes, D., V. M. Haughton, et al. (2000). "Mapping functionally related regions of brain with functional connectivity MR imaging." AJNR Am J Neuroradiol 21(9): 1636-1644.

Deco, G., V. K. Jirsa, et al. (2011). "Emerging concepts for the dynamical organization of resting-state activity in the brain." Nat Rev Neurosci 12(1): 43-56.

Dinges, D. F. and J. W. Powell (1985). "Microcomputer Analyses of Performance on a Portable, Simple Visual Rt Task During Sustained Operations." Behavior Research Methods Instruments & Computers 17(6): 652-655.

Drew, P. J., J. H. Duyn, et al. (2008). "Finding coherence in spontaneous oscillations." Nat Neurosci 11(9): 991-993.

Drummond, S. P., A. Bischoff-Grethe, et al. (2005). "The neural basis of the psychomotor vigilance task." Sleep 28(9): 1059-1068.

Eichele, T., S. Debener, et al. (2008). "Prediction of human errors by maladaptive changes in event-related brain networks." Proc Natl Acad Sci U S A 105(16): 6173-6178.

191

Eriksen, B. A. and C. W. Eriksen (1974). "Effects of Noise Letters Upon Identification of a Target Letter in a Nonsearch Task." Perception & Psychophysics 16(1): 143-149.

Feinberg, D. A. and K. Setsompop (2013). "Ultra-fast MRI of the human brain with simultaneous multi-slice imaging." Journal of Magnetic Resonance 229: 90-100.

Fox, M. D., M. Corbetta, et al. (2006). "Spontaneous neuronal activity distinguishes human dorsal and ventral attention systems." Proc Natl Acad Sci U S A 103(26): 10046-10051.

Fox, M. D., A. Z. Snyder, et al. (2005). "The human brain is intrinsically organized into dynamic, anticorrelated functional networks." Proc Natl Acad Sci U S A 102(27): 9673-9678.

Fox, M. D., D. Y. Zhang, et al. (2009). "The Global Signal and Observed Anticorrelated Resting State Brain Networks." Journal of Neurophysiology 101(6): 3270-3283.

Fransson, P. (2005). "Spontaneous low-frequency BOLD signal fluctuations: an fMRI investigation of the resting-state default mode of brain function hypothesis." Hum Brain Mapp 26(1): 15-29.

Friston, K. J., C. Buechel, et al. (1997). "Psychophysiological and modulatory interactions in neuroimaging." Neuroimage 6(3): 218-229.

Friston, K. J., L. Harrison, et al. (2003). "Dynamic causal modelling." Neuroimage 19(4): 1273-1302.

Fukuda, M., A. L. Vazquez, et al. (2012). "Effects of the alpha(2) -adrenergic receptor agonist dexmedetomidine on neural, vascular and BOLD fMRI responses in the somatosensory cortex." European Journal of Neuroscience.

Ganjoo, P., N. E. Farber, et al. (1998). "In vivo effects of dexmedetomidine on laser-Doppler flow and pial arteriolar diameter." Anesthesiology 88(2): 429-439.

Garrity, A. G., G. D. Pearlson, et al. (2007). "Aberrant "default mode" functional connectivity in schizophrenia." Am J Psychiatry 164(3): 450-457.

Gavrilescu, M., M. E. Shaw, et al. (2002). "Simulation of the effects of global normalization procedures in functional MRI." Neuroimage 17(2): 532-542.

Geddes, L. A., Roeder, R. (2001). "Measurement of the Direct-Current .Faradic. Resistance of the Electrode-Electrolyte Interface for Commonly Used Electrode Materials." Annals of Biomedical Engineering 29(2): 181-186.

Geddes, L. A., Roeder, R. (2003). "Criteria for the Selection of Materials for Implanted Electrodes." Annals of Biomedical Engineering 31(7): 879-890.

Girouard, H., A. D. Bonev, et al. (2010). "Astrocytic endfoot Ca2+ and BK channels determine both arteriolar dilation and constriction." Proc Natl Acad Sci U S A 107(8): 3811-3816.

Goense, J. B. and N. K. Logothetis (2008). "Neurophysiology of the BOLD fMRI signal in awake monkeys." Curr Biol 18(9): 631-640.

193

Graw, P., K. Krauchi, et al. (2004). "Circadian and wake-dependent modulation of fastest and slowest reaction times during the psychomotor vigilance task." Physiol Behav 80(5): 695-701.

Greicius, M. D., B. H. Flores, et al. (2007). "Resting-state functional connectivity in major depression: abnormally increased contributions from subgenual cingulate cortex and thalamus." Biol Psychiatry 62(5): 429-437.

Greicius, M. D., G. Srivastava, et al. (2004). "Default-mode network activity distinguishes Alzheimer's disease from healthy aging: evidence from functional MRI." Proc Natl Acad Sci U S A 101(13): 4637-4642.

Grigg, O. and C. L. Grady (2010). "Task-related effects on the temporal and spatial dynamics of resting-state functional connectivity in the default network." PLoS One 5(10): e13311.

Gruetter, R. (1993). "Automatic, localized in vivo adjustment of all first- and second-order shim coils." Magn Reson Med 29(6): 804-811.

Gujar, N., S. S. Yoo, et al. (2009). "The unrested resting brain: sleep deprivation alters activity within the default-mode network." J Cogn Neurosci 22(8): 1637-1648.

Gusnard, D. A. and M. E. Raichle (2001). "Searching for a baseline: functional imaging and the resting human brain." Nat Rev Neurosci 2(10): 685-694.

Hampson, M., N. R. Driesen, et al. (2006). "Brain connectivity related to working memory performance." J Neurosci 26(51): 13338-13343.

Hampson, M., B. S. Peterson, et al. (2002). "Detection of functional connectivity using temporal correlations in MR images." Hum Brain Mapp 15(4): 247-262.

Handwerker, D. A., V. Roopchansingh, et al. (2012). "Periodic changes in fMRI connectivity." Neuroimage 63(3): 1712-1719.

Harrell, F. E., Jr., R. M. Califf, et al. (1982). "Evaluating the yield of medical tests." Jama 247(18): 2543-2546.

Hasson, U., H. C. Nusbaum, et al. (2009). "Task-dependent organization of brain regions active during rest." Proc Natl Acad Sci U S A 106(26): 10841-10846.

He, B. J., A. Z. Snyder, et al. (2008). "Electrophysiological correlates of the brain's intrinsic large-scale functional architecture." Proc Natl Acad Sci U S A 105(41): 16039-16044.

Helps, S. K., S. J. Broyd, et al. (2010). "Altered spontaneous low frequency brain activity in attention deficit/hyperactivity disorder." Brain Res 1322: 134-143.

Honey, C. J., R. Kotter, et al. (2007). "Network structure of cerebral cortex shapes functional connectivity on multiple time scales." Proc Natl Acad Sci U S A 104(24): 10240-10245.

Hughes, S. W., D. W. Cope, et al. (2002). "Cellular mechanisms of the slow (<1 Hz) oscillation in thalamocortical neurons in vitro." Neuron 33(6): 947-958.

Hutchison, R. M., T. Womelsdorf, et al. (2012). "Resting-state networks show dynamic functional connectivity in awake humans and anesthetized macaques." Hum Brain Mapp.

195

Iadecola, C. and M. Nedergaard (2007). "Glial regulation of the cerebral microvasculature." <u>Nat Neurosci</u> 10(11): 1369-1376.

Iida, H., H. Ohata, et al. (1998). "Isoflurane and sevoflurane induce vasodilation of cerebral vessels via ATP-sensitive K+ channel activation." <u>Anesthesiology</u> 89(4): 954-960.

Jewett, M. E., D. J. Dijk, et al. (1999). "Dose-response relationship between sleep duration and human psychomotor vigilance and subjective alertness." <u>Sleep</u> 22(2): 171-179.

Josephs, O., R. Turner, et al. (1997). "Event-related f MRI." <u>Hum Brain Mapp</u> 5(4): 243-248.

Kay, K. N., S. V. David, et al. (2008). "Modeling low-frequency fluctuation and hemodynamic response timecourse in event-related fMRI." <u>Hum Brain Mapp</u> 29(2): 142-156.

Keilholz, S., M. E. Magnuson, et al. (2012). "Dynamic Properties of Functional Connectivity in the Rodent." <u>Brain Connect</u>.

Kelly, A. M., L. Q. Uddin, et al. (2008). "Competition between functional brain networks mediates behavioral variability." <u>Neuroimage</u> 39(1): 527-537.

Khader, P., T. Schicke, et al. (2008). "On the relationship between slow cortical potentials and BOLD signal changes in humans." <u>Int J Psychophysiol</u> 67(3): 252-261.

Kingery, W. S., G. S. Agashe, et al. (2002). "Isoflurane and nociception: spinal alpha2A adrenoceptors mediate antinociception while supraspinal alpha1 adrenoceptors mediate pronociception." <u>Anesthesiology</u> 96(2): 367-374.

Kiviniemi, V., T. Vire, et al. (2011). "A sliding time-window ICA reveals spatial variability of the default mode network in time." <u>Brain Connect</u> 1(4): 339-347.

Kuga, N., T. Sasaki, et al. (2011). "Large-scale calcium waves traveling through astrocytic networks in vivo." <u>J Neurosci</u> 31(7): 2607-2614.

Lennon, P. F. and P. A. Murray (1995). "Isoflurane and the pulmonary vascular pressure-flow relation at baseline and during sympathetic alpha- and beta-adrenoreceptor activation in chronically instrumented dogs." <u>Anesthesiology</u> 82(3): 723-733.

Leopold, D. A., Y. Murayama, et al. (2003). "Very slow activity fluctuations in monkey visual cortex: implications for functional brain imaging." <u>Cereb Cortex</u> 13(4): 422-433.

Lim, J. and D. F. Dinges (2008). "Sleep deprivation and vigilant attention." <u>Ann N Y Acad Sci</u> 1129: 305-322.

Lin, C. Y., M. H. Lin, et al. (2009). "In vivo cerebromicrovasculatural visualization using 3D DeltaR2-based microscopy of magnetic resonance angiography (3DDeltaR2-mMRA)." <u>Neuroimage</u> 45(3): 824-831.

Liu, X. and J. H. Duyn (2013). "Time-varying functional network information extracted from brief instances of spontaneous brain activity." <u>Proc Natl Acad Sci U S A</u> 110(11): 4392-4397.

Liu, X., X. H. Zhu, et al. (2010). "Neural Origin of Spontaneous Hemodynamic Fluctuations in Rats under Burst-Suppression Anesthesia Condition." <u>Cereb Cortex</u> 21(2): 374-384.

Liu, X., X. H. Zhu, et al. (2012). "The Change of Functional Connectivity Specificity in Rats Under Various Anesthesia Levels and its Neural Origin." <u>Brain Topogr</u>.

Logothetis, N. K. (2008). "What we can do and what we cannot do with fMRI." <u>Nature</u> 453(7197): 869-878.

Logothetis, N. K., Y. Murayama, et al. (2009). "How not to study spontaneous activity." <u>Neuroimage</u> 45(4): 1080-1089.

Logothetis, N. K., J. Pauls, et al. (2001). "Neurophysiological investigation of the basis of the fMRI signal." <u>Nature</u> 412(6843): 150-157.

Lu, H., Y. Zuo, et al. (2007). "Synchronized delta oscillations correlate with the resting-state functional MRI signal." <u>Proc Natl Acad Sci U S A</u> 104(46): 18265-18269.

Magnuson, M., W. Majeed, et al. (2010). "Functional connectivity in blood oxygenation level-dependent and cerebral blood volume-weighted resting state functional magnetic resonance imaging in the rat brain." <u>J Magn Reson Imaging</u> 32(3): 584-592.

Magri, C., U. Schridde, et al. (2012). "The amplitude and timing of the BOLD signal reflects the relationship between local field potential power at different frequencies." <u>J Neurosci</u> 32(4): 1395-1407.

198

Majeed, W., M. Magnuson, et al. (2011). "Spatiotemporal dynamics of low frequency BOLD fluctuations in rats and humans." Neuroimage 54(2): 1140-1150.

Majeed, W., M. Magnuson, et al. (2009). "Spatiotemporal dynamics of low frequency fluctuations in BOLD fMRI of the rat." J Magn Reson Imaging 30(2): 384-393.

Mayhew, J. E., S. Askew, et al. (1996). "Cerebral vasomotion: a 0.1-Hz oscillation in reflected light imaging of neural activity." Neuroimage 4(3 Pt 1): 183-193.

Miezin, F. M., L. Maccotta, et al. (2000). "Characterizing the hemodynamic response: effects of presentation rate, sampling procedure, and the possibility of ordering brain activity based on relative timing." Neuroimage 11(6 Pt 1): 735-759.

Monto, S., S. Palva, et al. (2008). "Very slow EEG fluctuations predict the dynamics of stimulus detection and oscillation amplitudes in humans." J Neurosci 28(33): 8268-8272.

Murphy, K., R. M. Birn, et al. (2009). "The impact of global signal regression on resting state correlations: are anti-correlated networks introduced?" Neuroimage 44(3): 893-905.

Nielsen, T., J. Montplaisir, et al. (1993). "Decreased interhemispheric EEG coherence during sleep in agenesis of the corpus callosum." Eur Neurol 33(2): 173-176.

Ogawa, S., R. S. Menon, et al. (1993). "Functional brain mapping by blood oxygenation level-dependent contrast magnetic resonance imaging. A comparison of signal characteristics with a biophysical model." Biophys J 64(3): 803-812.

Ohata, H., H. Iida, et al. (1999). "Intravenous dexmedetomidine inhibits cerebrovascular dilation induced by isoflurane and sevoflurane in dogs." <u>Anesth Analg</u> 89(2): 370-377.

Pan, W. J., G. Thompson, et al. (2010). "Simultaneous FMRI and electrophysiology in the rodent brain." <u>J Vis Exp</u>(42).

Pan, W. J., G. Thompson, et al. (2011). "Broadband local field potentials correlate with spontaneous fluctuations in functional magnetic resonance imaging signals in the rat somatosensory cortex under isoflurane anesthesia." <u>Brain Connect</u> 1(2): 119-131.

Pan, W. J., G. J. Thompson, et al. (2013). "Infraslow LFP correlates to resting-state fMRI BOLD signals." <u>Neuroimage</u> 74C: 288-297.

Pawela, C. P., B. B. Biswal, et al. (2009). "A protocol for use of medetomidine anesthesia in rats for extended studies using task-induced BOLD contrast and resting-state functional connectivity." <u>Neuroimage</u> 46(4): 1137-1147.

Paxinos, G. and C. Watson (2005). <u>The rat brain in stereotaxic coordinates</u>. Amsterdam ; Boston, Elsevier Academic Press.

Porret, C. A., N. Stergiopulos, et al. (1998). "Flow-driven diameter response in rat femoral arteries perfused in vitro." <u>Ann Biomed Eng</u> 26(4): 526-533.

Prado, J., J. Carp, et al. (2011). "Variations of response time in a selective attention task are linked to variations of functional connectivity in the attentional network." <u>Neuroimage</u> 54(1): 541-549.

200

Prado, J. and D. H. Weissman (2011). "Heightened interactions between a key default-mode region and a key task-positive region are linked to suboptimal current performance but to enhanced future performance." <u>Neuroimage</u> 56(4): 2276-2282.

Prado, J. and D. H. Weissman (2011). "Spatial attention influences trial-by-trial relationships between response time and functional connectivity in the visual cortex." <u>Neuroimage</u> 54(1): 465-473.

Raichle, M. E. (2006). "The brain's dark energy." <u>Science</u> 314(5803): 1249-1250.

Raichle, M. E., A. M. MacLeod, et al. (2001). "A default mode of brain function." <u>Proc Natl Acad Sci U S A</u> 98(2): 676-682.

Reiz, S., E. Balfors, et al. (1983). "Isoflurane--a powerful coronary vasodilator in patients with coronary artery disease." <u>Anesthesiology</u> 59(2): 91-97.

Ries, C. R. and E. Puil (1999). "Mechanism of anesthesia revealed by shunting actions of isoflurane on thalamocortical neurons." <u>J Neurophysiol</u> 81(4): 1795-1801.

Rombouts, S. A., F. Barkhof, et al. (2005). "Altered resting state networks in mild cognitive impairment and mild Alzheimer's disease: an fMRI study." <u>Hum Brain Mapp</u> 26(4): 231-239.

Sadaghiani, S., G. Hesselmann, et al. (2010). "The relation of ongoing brain activity, evoked neural responses, and cognition." <u>Front Syst Neurosci</u> 4: 20.

Sadaghiani, S., G. Hesselmann, et al. (2009). "Distributed and antagonistic contributions of ongoing activity fluctuations to auditory stimulus detection." <u>J Neurosci</u> 29(42): 13410-13417.

Sakoglu, U., G. D. Pearlson, et al. (2010). "A method for evaluating dynamic functional network connectivity and task-modulation: application to schizophrenia." Magma 23(5-6): 351-366.

Scholvinck, M. L., A. Maier, et al. (2010). "Neural basis of global resting-state fMRI activity." Proc Natl Acad Sci U S A 107(22): 10238-10243.

Schwinn, D. A., R. W. McIntyre, et al. (1990). "Isoflurane-induced vasodilation: role of the alpha-adrenergic nervous system." Anesth Analg 71(5): 451-459.

Seeley, W. W., V. Menon, et al. (2007). "Dissociable intrinsic connectivity networks for salience processing and executive control." J Neurosci 27(9): 2349-2356.

Shmuel, A. and D. A. Leopold (2008). "Neuronal correlates of spontaneous fluctuations in fMRI signals in monkey visual cortex: Implications for functional connectivity at rest." Hum Brain Mapp 29(7): 751-761.

Sinclair, M. D. (2003). "A review of the physiological effects of alpha(2)-agonists related to the clinical use of medetomidine in small animal practice." Canadian Veterinary Journal-Revue Veterinaire Canadienne 44(11): 885-897.

Singh, K. D. and I. P. Fawcett (2008). "Transient and linearly graded deactivation of the human default-mode network by a visual detection task." Neuroimage 41(1): 100-112.

Sirotin, Y. B. and A. Das (2009). "Anticipatory haemodynamic signals in sensory cortex not predicted by local neuronal activity." Nature 457(7228): 475-479.

Steriade, M., D. Contreras, et al. (1993). "The slow (< 1 Hz) oscillation in reticular thalamic and thalamocortical neurons: scenario of sleep rhythm generation in interacting thalamic and neocortical networks." J Neurosci 13(8): 3284-3299.

Steriade, M., A. Nunez, et al. (1993). "Intracellular analysis of relations between the slow (< 1 Hz) neocortical oscillation and other sleep rhythms of the electroencephalogram." J Neurosci 13(8): 3266-3283.

Steriade, M., A. Nunez, et al. (1993). "A novel slow (< 1 Hz) oscillation of neocortical neurons in vivo: depolarizing and hyperpolarizing components." J Neurosci 13(8): 3252-3265.

Tagliazucchi, E., F. von Wegner, et al. (2012). "Dynamic BOLD functional connectivity in humans and its electrophysiological correlates." Front Hum Neurosci 6: 339.

Tallgren, P. (2006). DC-EEG For Routine Clinical Use: Methods And Clinical Impact Doctor of Science in Technology, Helsinki University of Technology.

Tambini, A., N. Ketz, et al. (2010). "Enhanced brain correlations during rest are related to memory for recent experiences." Neuron 65(2): 280-290.

Thompson, G. J., M. E. Magnuson, et al. (2012). "Short-time windows of correlation between large-scale functional brain networks predict vigilance intraindividually and interindividually." Hum Brain Mapp.

Tian, L., T. Jiang, et al. (2006). "Altered resting-state functional connectivity patterns of anterior cingulate cortex in adolescents with attention deficit hyperactivity disorder." Neurosci Lett 400(1-2): 39-43.

203

Tort, A. B., R. Komorowski, et al. (2010). "Measuring phase-amplitude coupling between neuronal oscillations of different frequencies." J Neurophysiol 104(2): 1195-1210.

Trimmel, M., A. Mikowitsch, et al. (1990). "Occurrence of infraslow potential oscillations in relation to task, ability to concentrate and intelligence." Int J Psychophysiol 9(2): 167-170.

Trimmel, M., F. Strassler, et al. (2001). "Brain DC potential changes of computerized tasks and paper/pencil tasks." Int J Psychophysiol 40(3): 187-194.

van de Ven, V. G., E. Formisano, et al. (2004). "Functional connectivity as revealed by spatial independent component analysis of fMRI measurements during rest." Hum Brain Mapp 22(3): 165-178.

Villalobos, M. E., A. Mizuno, et al. (2005). "Reduced functional connectivity between V1 and inferior frontal cortex associated with visuomotor performance in autism." Neuroimage 25(3): 916-925.

Vincent, J. L., G. H. Patel, et al. (2007). "Intrinsic functional architecture in the anaesthetized monkey brain." Nature 447(7140): 83-86.

Waites, A. B., A. Stanislavsky, et al. (2005). "Effect of prior cognitive state on resting state networks measured with functional connectivity." Hum Brain Mapp 24(1): 59-68.

Wang, L., P. Laviolette, et al. (2010). "Intrinsic connectivity between the hippocampus and posteromedial cortex predicts memory performance in cognitively intact older individuals." Neuroimage 51(2): 910-917.

Weissman, D. H., K. C. Roberts, et al. (2006). "The neural bases of momentary lapses in attention." <u>Nat Neurosci</u> 9(7): 971-978.

Williams, K. A., M. Magnuson, et al. (2010). "Comparison of alpha-chloralose, medetomidine and isoflurane anesthesia for functional connectivity mapping in the rat." <u>Magn Reson Imaging</u> 28(7): 995-1003.

Yacoub, E., A. Shmuel, et al. (2001). "Imaging brain function in humans at 7 Tesla." <u>Magn Reson Med</u> 45(4): 588-594.

Zang, Y. F., Y. He, et al. (2007). "Altered baseline brain activity in children with ADHD revealed by resting-state functional MRI." <u>Brain Dev</u> 29(2): 83-91.

Zhao, F., T. Zhao, et al. (2008). "BOLD study of stimulation-induced neural activity and resting-state connectivity in medetomidine-sedated rat." <u>Neuroimage</u> 39(1): 248-260.

Zornow, M. H., J. E. Fleischer, et al. (1990). "Dexmedetomidine, an alpha 2-adrenergic agonist, decreases cerebral blood flow in the isoflurane-anesthetized dog." <u>Anesth Analg</u> 70(6): 624-630.